University of New Mexico
UNM Digital Repository

Chemical and Biological Engineering ETDs | Engineering ETDs

2-8-2011

Printable lithium batteries

Kyle Fenton

Follow this and additional works at: https://digitalrepository.unm.edu/cbe_etds

Recommended Citation
Fenton, Kyle. "Printable lithium batteries." (2011). https://digitalrepository.unm.edu/cbe_etds/6

This Dissertation is brought to you for free and open access by the Engineering ETDs at UNM Digital Repository. It has been accepted for inclusion in Chemical and Biological Engineering ETDs by an authorized administrator of UNM Digital Repository. For more information, please contact disc@unm.edu.

Kyle Fenton
Candidate

Chemical Engineering
Department

This dissertation is approved, and it is acceptable in quality and form for publication:

Approved by the Dissertation Committee:

, Chairperson

PRINTABLE LITHIUM BATTERIES

BY

KYLE FENTON

B.S. Chemical Engineering
University of New Mexico
Albuquerque, NM, 2003.

M.S. Chemical Engineering
University of New Mexico
Albuquerque, NM, 2007.

DISSERTATION

Submitted in Partial Fulfillment of the
Requirements for the Degree of

Doctor of Philosophy
Engineering

The University of New Mexico
Albuquerque, New Mexico

December, 2010

DEDICATION

To my friends and family.

ACKNOWLEDGEMENTS

I heartily acknowledge Dr. Chris Apblett and Dr. Plamen Atanassov, my advisors during this work for their continual support and patience during the entirety of this dissertation. I gratefully acknowledge Dr. Apblett for his time and discussions while learning this material. Without his leadership and direction, I would be in quite a different situation than I am today. I am forever grateful and cannot express the gratitude I have for his efforts. They are nothing short of heroic.

I would like to thank my committee members for their recommendations and their contributions to the development of this work.

I would like to thank my friends at Sandia National Laboratories who became my colleagues, my entertainment, and my friends during this work. Eric, Adam, Paul, Connie, and Chris will, I hope, become a mainstay in my future endeavors and I am honored that they were able to share this one. I was definitely “enriched” by them.

I would like to thank the NSF IGERT program, through the NSMS program at UNM, for the funding that I received during this work.

Finally, I would like to thank my close friends and family. Their contributions have been monumental.

PRINTABLE LITHIUM BATTERIES

BY

KYLE FENTON

ABSTRACT OF DISSERTATION

Submitted in Partial Fulfillment of the
Requirements for the Degree of

Doctor of Philosophy
Engineering

The University of New Mexico
Albuquerque, New Mexico

December, 2010

PRINTABLE LITHIUM BATTERIES

by

Kyle Fenton

B.S., Chemical Engineering, University of New Mexico, 2003

M.S., Chemical Engineering, University of New Mexico, 2007

Ph.D., Chemical Engineering, University of New Mexico, 2010

ABSTRACT

Printable lithium iron phosphate ($LiFePO_4$) cathodes and porous aerogel / polymer separators have been designed, constructed, and tested. The cathodes consist of LiFePO4, PVDF binder, and conductive carbon which was developed for robocast deposition (printing) onto carbon coated aluminum substrates to form 60 μm thick cathodes. Electrochemical and physical evaluation of these printed cathodes was performed to determine capacity, rate capability, and lifetime performance of the printed cathodes. Cells were constructed using a standard 2032 coin cell to ensure uniform electrode size and pressure on the layers of the battery. Cathodes printed exhibited up to 115 mAh/g capacity with a commercial separator and have 89% retention of capacity after 60 continuous charge / discharge cycles. The physical characteristics for the printed cathodes were evaluated using SEM and EDS techniques to determine the morphology of the cathodes as printed.

Several polymers were evaluated to identify applicability for a printed separator. In order to allow for the resulting printed separator to remain porous, an aerogel material

was added to the printing slurry before deposition. The materials were evaluated for rheological properties and printing results to identify an optimal material for a printable separator. The polypropylene/polyethylene material identified as a suitable printed separator was printed directly onto printed cathodes and electrochemical and physical evaluations were conducted on the resulting battery material to determine ability to cycle and rate capability. The printed cathode and separator exhibited up to 60 mAh/g capacity. An optimal ratio between the polymer binder and the aerogel porous component was established based upon testing in a 2032 coin cell using liquid electrolytes. The ratio of binder to aerogel which exhibited the highest electrochemical performance in a full cell was predicted to have the lowest performance. This unexpected relationship was explored based upon impedance measurements of the cells. The performance of these battery components printed using the robocasting technique was compared to current alternative technologies. The resulting comparison indicates that printed battery constituents using the robocasting technique is a viable method for developing printed lithium battery systems which exhibit similar performance to alternative techniques. Additionally, the robocasting technique for battery development allows for printing of battery materials in nearly any geometry in both planar and three dimensional systems depending on the application needs.

TABLE OF CONTENTS

LIST OF FIGURES

LIST OF TABLES

CHAPTER 1: INTRODUCTION

Interest in battery technology has recently become significant due to the fact that many devices rely on batteries for their operation. This demand seems to be increasing at a very rapid rate due to the exponential growth of the number and complexity of devices made. New battery technologies not only needs to be able to meet the power and longevity demands for new devices, but much also be adapted towards smaller footprints and more environmentally friendly chemical constituents. Increasing demands on battery technology will push research towards new and innovative directions and promises to be a very interesting and fruitful field in the coming years. Lithium batteries are one of the technologies which may be able to answer to this increasing demand due to their high specific energy density, their high operation voltage, and their ability to be configured as rechargeable (1). Furthermore, lithium batteries have been made in a variety of shapes and sizes with including thin film batteries which are very small (~ 100 μm thick) but are still able to yield usable amounts of power such as commercial cells such as those from Frontedge Technologies, Inc. (2). The ability to make thin batteries with novel properties such as footprints or shapes that can be specified for any application or batteries which can operate while being completely flexible will be an enabling technology for future devices.

Batteries, in their simplest form, are devices which convert chemical energy stored in the active materials within the battery into usable energy. This conversion happens through a series of reactions called electrochemical oxidation/reduction (redox) reactions. In a battery, the electrochemical reactions transfer electrons between the

chemicals in the battery through an external circuit, which produces usable electricity. There are many chemical oxidation reactions, such as rusting or burning, which involve direct transfer of electrons between the chemical constituents (as opposed to through an external circuit) and often produce heat. Unlike these reactions, the electrochemical redox reactions within a secondary battery are reversible and generate an ion to counter the electron which will travel through the external circuit. The big gain in the electrochemical reactions within a battery are that unlike combustion, electrochemical reactions are not subject to the limitations of the Carnot cycle and therefore are capable of higher energy conversion efficiencies (3).

Batteries are comprised of many different layers, each with unique material chemistries and material properties. Each of these layers is engineered to suit a specific demand for the specific function in the battery. There are five major parts to a battery. The anode or negative electrode is the electrode which gives up electrons to the external circuit and ions to the electrolyte: it is oxidized during the electrochemical reaction. The cathode or positive electrode is the electrode that accepts electrons from the external circuit and ions from the electrolyte: it is reduced during the electrochemical reaction. The separator is a layer which separates the anode and cathode and allows for ionic conductivity but keeps the anode and cathode physically separated to prevent an internal short of the battery. The electrolyte is the medium that facilitates the transfer of charge or ions between the anode and cathode. The electrolyte is typically a liquid but many solid electrolytes have been developed. The package of the battery is the final component which encapsulates the chemistry from the environment and allows for the connection with the external circuit. The design of the package or encapsulant is critical

for the isolation of the electrochemical reactions within the battery from parasitic side reactions caused by unwanted chemicals in contact with the active battery materials. Any unwanted chemical reactions due to improperly designed packaging can result in loss of battery performance, inability for the battery to be charged / discharged, complete shorting of the battery anode and cathode and even safety concerns such as ignition or detonation.

Battery operation for a rechargeable battery occurs in two different modes, charge and discharge. A diagram for how charge and discharge modes work within a cell can be seen in Figure 1, as seen in ref (4). During cell discharge electrons flow from the anode which is oxidized, through the external circuit to the cathode which is reduced. While this happens, the circuit is completed by the flow of ions within the battery electrolyte between the anode and cathode. During cell charge (which only occurs on rechargeable, or secondary, batteries) the current flow is reversed and the redox reactions at each electrode reverses. The anode becomes the positive electrode and the cathode becomes the negative electrode. Typically, one refers to the electrodes based on the redox reaction occurring at them instead of the polarity of

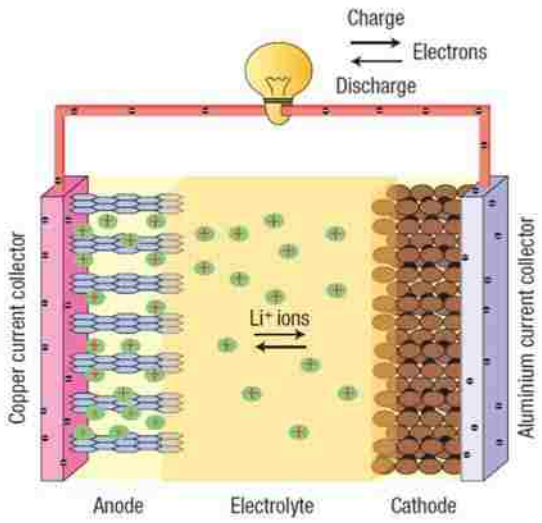

Figure 1 – Operational modes of a battery. The flow of electrons through the external cell occur from left to right during charge and right to left during discharge. Shown is a generic scheme for lithium batteries, the concept is the same for any chemistry. From ref (4).

the electrode itself. For example, during charge, the convention for the anode to be negative does not apply.

Battery Classifications

Batteries are classified in several different ways. The classifications are primarily on how the battery is used.

Primary batteries are batteries which are created in the charged state and once they are fully discharged they are not capable of being recharged. This is because the redox reaction involved in the cell is not reversible. Many of these batteries contain an absorbent separator and are therefore known as dry batteries. The primary advantages of primary batteries are their cost and weight. They tend to be a lightweight and inexpensive source of power commonly used in portable electronics, lighting, photography, and in common household devices.

Secondary batteries are able to be recharged electrically. This is done by passing current in the opposite direction from their discharge mode of operation. This charging mode is possible due to the chemical reversibility of the redox pair used for the anode and cathode. Every chemical formulation for the redox pair will differ in their extent of reversibility, which is one of the effects which give batteries different characteristics for the lifetime or number of charge / discharge cycles possible. There are numerous other factors that influence this lifetime capability which will be discussed in more detail later in this manuscript such as dendrite growth, parasitic reactions, and solid electrolyte interface (SEI) formation. These batteries are typically used as either as an energy

storage media or as if they were a primary battery but then are recharged instead of discarded. Secondary batteries typically have lower energy density than primary batteries but that is made up by the fact that they can be cycled many times.

Reserve batteries are a special type of battery in which one part of the battery is physically separated from the rest of the battery components until the battery is needed for use. During activation, the separated component is introduced into the battery and the battery goes live for use. Separating one of the components almost eliminates chemical deterioration or self-discharge of the battery; this makes the shelf-life of the reserve battery much longer than primary or secondary batteries. A good example of these types of batteries would be car batteries, a Pb/PbO_2 chemistry that can be stored in air for a long time. When an acid electrolyte is introduced, the battery becomes live, and can be cycled.

The design of batteries is almost always application specific. There are many factors that affect battery performance. Everything from the chemical makeup of the battery to the package size and shape can affect whether or not a specific battery will work for a given application. Without a specific application in mind, a battery may be of little use.

Battery Performance and Capacity

Batteries can be rated by their theoretical performance. The chemical compounds in the battery limit the possible power output of the oxidation-reduction (redox) reaction. The chemistry used in a cell also serves to set the voltage that a given cell will produce.

Since the maximum power a cell can produce, based on the chemistry used serves as the upper bound for the amount of usable energy within a given cell, much of the engineering and science behind batteries revolves around learning how to extract the maximum amount of energy from the material. This involves optimizing many properties within the cell such as transport kinetics, reaction kinetics, electrode materials and properties, electrolyte composition and properties, packaging, and minimization of activation and transport losses within the cell in order to achieve a maximum capacity for the battery.

Theoretical performance of a battery can be calculated through free energy. The release of free energy during an electrochemical reaction can be expressed thermodynamically by:

$$\Delta G = -nFE^o \tag{1}$$

where F is Faradays constant (96,480.3 C or 26.8 Ah), n is the valency change or number of electrons transferred in the reaction, and E^o is the standard potential of the reaction in volts. This can be used to evaluate the free energy change of an electrochemical reaction.

When examining the theoretical energy for an entire cell, many values for the standard potential of a redox reaction have been published, see Figure 2. These published values are either determined experimentally or calculated from the free energy of the reaction. To calculate a standard potential for the battery, one must calculate the difference between the anodic or oxidation potential and the cathodic or reduction potential. This will give the theoretical voltage at which the battery should operate. This shows an important point in battery design. The operational voltage of the cell is set by material choice. The operational plateau which a cell will cycle at is determined solely by the difference between the redox potential of the anodic and cathodic processes during discharge. The theoretical voltage of the cell can be mildly affected by many things having to do with the design, fabrication, and operation of the battery but will always be very near the standard potential difference between the anode and cathode.

Electrode reaction	E°, V	Electrode reaction	E°, V
$Li^+ + e \rightleftharpoons Li$	−3.01	$Tl^+ + e \rightleftharpoons Tl$	−0.34
$Rb^+ + e \rightleftharpoons Rb$	−2.98	$Co^{2+} + 2e \rightleftharpoons Co$	−0.27
$Cs^+ + e \rightleftharpoons Cs$	−2.92	$Ni^{2+} + 2e \rightleftharpoons Ni$	−0.23
$K^+ + e \rightleftharpoons K$	−2.92	$Sn^{2+} + 2e \rightleftharpoons Sn$	−0.14
$Ba^{2+} + 2e \rightleftharpoons Ba$	−2.92	$Pb^{2+} + 2e \rightleftharpoons Pb$	−0.13
$Sr^{2+} + 2e \rightleftharpoons Sr$	−2.89	$D^+ + e \rightleftharpoons \frac{1}{2}D_2$	−0.003
$Ca^{2+} + 2e \rightleftharpoons Ca$	−2.84	$H^+ + e \rightleftharpoons \frac{1}{2}H_2$	0.000
$Na^+ + e \rightleftharpoons Na$	−2.71	$Cu^{2+} + 2e \rightleftharpoons Cu$	0.34
$Mg^{2+} + 2e \rightleftharpoons Mg$	−2.38	$\frac{1}{2}O_2 + H_2O + 2e \rightleftharpoons 2OH^-$	0.40
$Ti^+ + 2e \rightleftharpoons Ti$	−1.75	$Cu^+ + e \rightleftharpoons Cu$	0.52
$Be^{2+} + 2e \rightleftharpoons Be$	−1.70	$Hg^{2+} + 2e \rightleftharpoons 2Hg$	0.80
$Al^{3+} + 3e \rightleftharpoons Al$	−1.66	$Ag^+ + e \rightleftharpoons Ag$	0.80
$Mn^{2+} + 2e \rightleftharpoons Mn$	−1.05	$Pd^{2+} + 2e \rightleftharpoons Pd$	0.83
$Zn^{2+} + 2e \rightleftharpoons Zn$	−0.76	$Ir^{3+} + 3e \rightleftharpoons Ir$	1.00
$Ga^{3+} + 3e \rightleftharpoons Ga$	−0.52	$Br_2 + 2e \rightleftharpoons 2Br^-$	1.07
$Fe^{2+} + 2e \rightleftharpoons Fe$	−0.44	$O_2 + 4H^+ + 4e \rightleftharpoons 2H_2O$	1.23
$Cd^{2+} + 2e \rightleftharpoons Cd$	−0.40	$Cl_2 + 2e \rightleftharpoons 2Cl^-$	1.36
$In^{3+} + 3e \rightleftharpoons In$	−0.34	$F_2 + 2e \rightleftharpoons 2F^-$	2.87

Figure 2 – Standard redox potentials for common battery reactions. The difference between the anodic and cathodic reactions determines the overall redox potential for the full cell. From ref (3).

The primary factors that can affect the operational voltage of a cell are temperature and concentration as described by the Nernst equation:

$$E = E^o - \frac{RT}{nF} ln\left(\frac{{a_p}^c {a_p}^d}{{a_r}^a {a_r}^b}\right) \quad (2)$$

where $a_r \; and \; a_p$ is the activity of the reactants and products raised to their respective stoichometric coefficient, R is the gas constant, T is absolute temperature, n, F, and E^o are as defined previously. This equation shows the effect of the temperature and the ratio of the electrochemical species and their activity. It is uncommon to have a battery which operates exactly at the theoretical potential, for reasons that will be discussed below.

The theoretical capacity is also considered when designing and optimizing batteries. This is done similarly to theoretical voltages and can be calculated using the density of the electrochemical species:

$$Capacity = \frac{nF}{3600 * \rho} \quad (3)$$

Where F is Faraday's constant in units of C/mol, ρ is the density of the species in g/mol and n is the valence change for the electrochemical reaction. To determine the overall theoretical capacity of the entire battery is calculated based on the equivalent weights of both the anodic and cathodic reactions. The calculation must be done in equivalent weights per amp-hour or the calculation will be incorrect.

The theoretical capacity for a battery is very rarely attained due to the fact that there are always non reactive components of the battery (electrolytes and separator) as well as packaging. This reduces the capacity of the battery even if the engineering design were able to use all of the energy liberated by the electrochemical reactions. The loss in

battery capacity based solely on battery non-reactive species and package can be as great as 65-75% of the theoretical capacity. Figure 3 shows typical losses for battery performance based on non reactive materials (3).

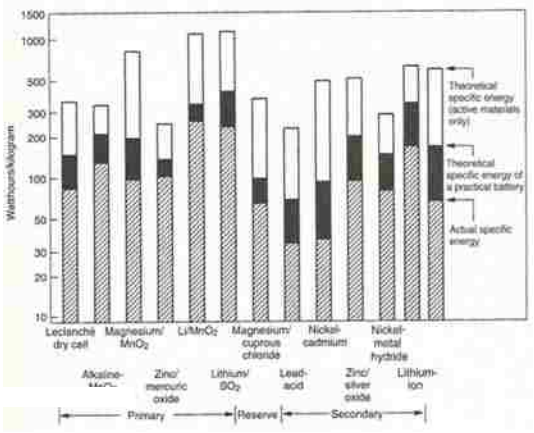

Figure 3 – Typical loss within a cell. Loss of capacity is based on many factors such as materials, manufacturing, and inert components. From ref (3).

This loss in capacity is compounded by the fact that not every battery is made identically. The differences in chemical composition, different manufacturing protocols, different cell shapes and sizes can all have an effect on the deviation of an actual battery from its theoretical performance. This can be seen in plots similar to Figure 4 which depict typical energy outputs for different types of batteries (5). If plots like this were based solely on the chemical components, then there would be a dot for each type of battery. Instead, there is a design window for each type of battery. The engineer must work within that design window to build a suitable power source for the specific application.

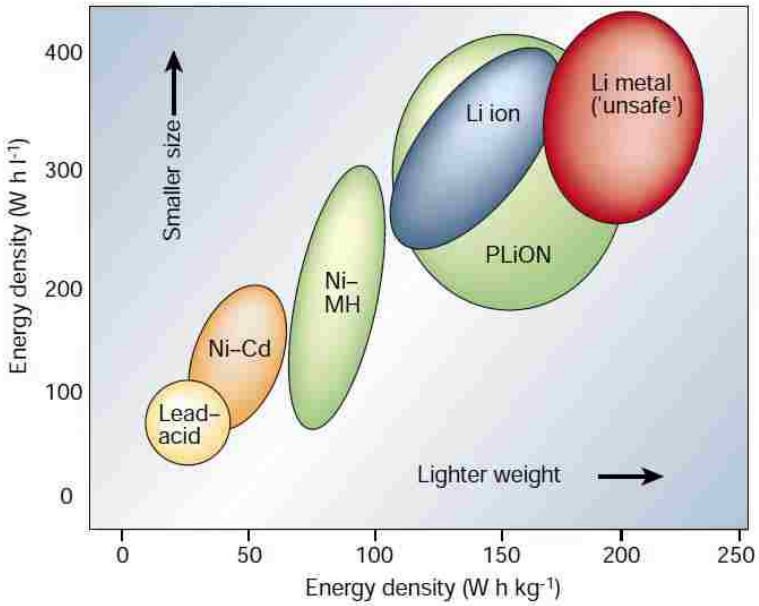

Figure 4 – Specific energy comparison for various battery chemistries. From ref (5).

Lithium Battery Development

Unlike electronics and current semiconductor research which has been doubling in performance every 18 months, according to Moore's law, batteries have not been able to keep up the pace in advances (3). During the cycling of a battery, the chemicals are either completely used up in the electrochemical reaction (primary) or reacted on one electrode then the other repeatedly (secondary) and are therefore limited by the materials that can be used and not the process. Most of the latest advances have been with lithium batteries. These batteries are able to deliver over 200 Wh/kg of power which is well above the specific energy density of previous generations of batteries. This figure of merit is often used to indicate the performance of a battery. The specific energy density

in Wh/kg is the current a battery can produce multiplied by the voltage at which it produces that power divided by the weight of the cell. Most of the higher energy density discoveries have used lithium or lithium ion technology and it appears that the research is still heavily invested in furthering lithium technology.

Lithium is the lightest of all metallic elements and is very electronegative (-3.04V vs. the standard hydrogen electrode (SHE)) (7). The color quickly fades into a grey dull color in the presence of air. The density of lithium is about half that of water, making lithium a very light but very powerful chemical. Lithium generates 3.86 Ah/g, which is the highest electrochemical equivalence and it also has the highest generated voltage of any of the metals.

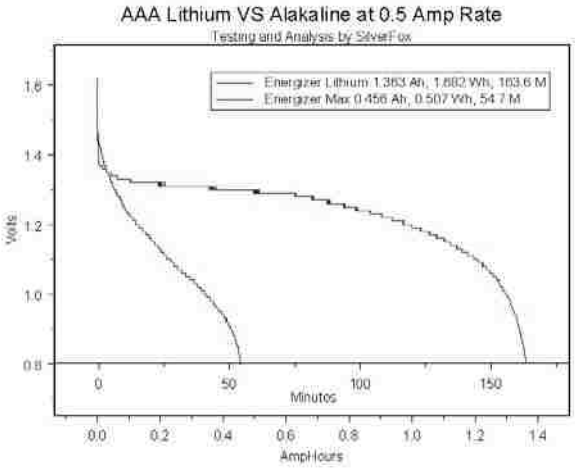

Figure 5 – Comparison of Energizer lithium and alkaline AAA form factor batteries. From ref (6).

As seen in Figure 2, the redox potential for lithium half cell reaction is the lowest of all the metals. This means that full cells using lithium as the anode create the highest operating voltage. Cells with lithium anodes can operate up to over 4 volts depending on the cathode chemistry. This allows for use of fewer batteries in series in order to achieve high voltage. Lithium has a high specific energy so lithium batteries also have several times more energy than a traditional alkaline zinc battery (with a MnO_2 cathode). Lithium can operate in a fairly wide temperature range. The discharge voltage for many

lithium batteries can remain relatively constant due to the crystalline structure allowing the lithium to transport into the unit cell of the cathodic crystal lattice without causing an appreciable amount of swelling or stress (8, 9). This allows for the continual transport and reaction of the lithium redox reaction within the crystal lattice at a constant voltage. The output fluctuations of lithium batteries can be very small compare to more traditional chemistries such as alkaline cells and the capacity of lithium cells is much larger than alkaline cells, as seen in Figure 5 (6). Another benefit to using lithium cells is that the shelf life can be up to 20 years (3, 10).

Despite being more energetic and having a large capacity, there are several major drawbacks to lithium batteries. Lithium is extremely reactive and can be extremely dangerous. The major reaction that occurs is between lithium and water:

$$2Li(s) + 2H_2O \rightarrow 2LiOH\ (aq) + H_2(g) \quad (4)$$

which is a highly exothermic reaction. When this occurs, the heat released during the reaction can cause the hydrogen gas to ignite. Many of the chemicals traditionally used for cathode can be environmentally unfriendly, such as cobalt or manganese based cathodes (11). This makes wide production of those types of batteries undesirable.

Lithium batteries can be made into three main types of batteries depending on composition: primary lithium batteries, secondary lithium batteries, and lithium ion batteries.

Primarily lithium batteries all used metallic lithium as their anode material. They vary in the cathode composition. Just by varying the cathode composition they have

theoretical voltages anywhere between 1.75 and 3.9 volts and will theoretically produce over 2000 Wh/kg for carbon monofluoride (CF) cathodes (12, 13). These values are rarely obtained, as discussed previously, and will typically produce somewhere between 215 Wh/kg for CF cathodes and 590 Wh/kg for thionyl chloride ($SOCl_2$) cathodes. There are 3 styles of primary lithium batteries, depending on the phase of the battery layers: soluble cathode cells, solid cathode cells, and solid electrolyte cells. Soluble cathode cells have a cathode that is liquid or gas and dissolves in the solvent. A solid-electrolyte interface (SEI) type layer forms on the lithium anode to allow for operation of the cell. Solid cathode cells are the more typical style of cells which consist of lithium metal anode and a solid cathode. Solid electrolyte cells use a solid electrolyte and are incredibly stable but have lower discharge rates than gel or liquid electrolyte cells (14).

The SEI layer in a lithium battery forms during the first cycle of the cell and occurs within solid electrode cells with liquid electrolytes. The exact composition of this layer varies, but is usually due to a breakdown of the electrolyte or impurities within the electrolyte reacting with the electrode to form a passivation layer on the surface of the electrode (15-17). This SEI layer adds to the overall impedance of the cell and restricts transport to the electrodes or aids in preventing the intercalation of the lithium out of the electrode (18).

Secondary lithium batteries are very similar to primary lithium batteries in that they use lithium metal as an anode and vary the cathode. There are a variety of different cathode compositions used for specific applications. This type of battery uses aprotic solvents to ensure no cross reaction with lithium, which limits their conductivity and therefore limits their performance. The secondary lithium battery is the primarily

researched lithium cell, as it can produce the highest specific capacity for a rechargeable cell and typically has very good lifetime performance. There are, however, several drawbacks to these batteries.

The first is the problem of dendrite formation (7, 19). During repetitive charge and discharge cycles of a lithium battery, the plating of the lithium ion onto the metallic anode occurs differently each time. As the number of cycles increases, there can be preferential plating at certain locations on the metal electrode. The continual plating at this preferential location will result in the formation of a large dendrite, which is a safety concern as these dendrites may grow through the separator material causing a short in the cell and possibly a runaway reaction between the anode and cathode (20). The second concern of the secondary lithium ion battery is the safety concern for the lithium reaction with water as seen in equation 4. There have been many approaches used to reduce this concern, namely engineering of better seals for battery packaging, use of additives in the cell electrolytes to suppress this reaction, and engineered separators to prevent thermal runaway (11, 21-26). The concern for safety that this poses is one of the driving forces behind the development of the lithium-ion battery.

Lithium-ion batteries do not use metallic lithium as the anode material. They instead use a lithium intercalation compound as the anode material (3). Intercalation compounds allow for the introduction of lithium ions into the lattice structure for both anode and cathode. This type of cell does not contain lithium in any metallic form, only ionic or as a compound intercalated into an electrode. The intercalation of the lithium ion into the electrode at a given lattice point results in a swelling of the electrode. This phenomenon can even be seen in graphitic anode electrodes. Since both electrodes in

lithium-ion batteries are made of intercalation compounds, the lithium ions shuttle back and forth between the anode and cathode. This gives rise to the term “rocking chair” or “flip flop” batteries which are commonly used for lithium ion batteries. The potential generated in these batteries is based solely on the difference in free energy of the electrodes when lithium is intercalated into one electrode or the other. The use of these types of batteries has advantages over using lithium metal as an anode material due to the safety concerns of having metallic lithium within the cell. The downside to using two intercalation materials is that they do not produce as much energy as a cell which uses metallic lithium, see Figure 6. From this plot it can be seen that there is a fourfold increase in capacity when using metallic lithium rather than the highest performing intercalation compounds for the negative electrode (5). This has dramatic implication on the use of intercalation compounds for the negative electrode in applications which require a high amount of energy such as most portable electronic applications.

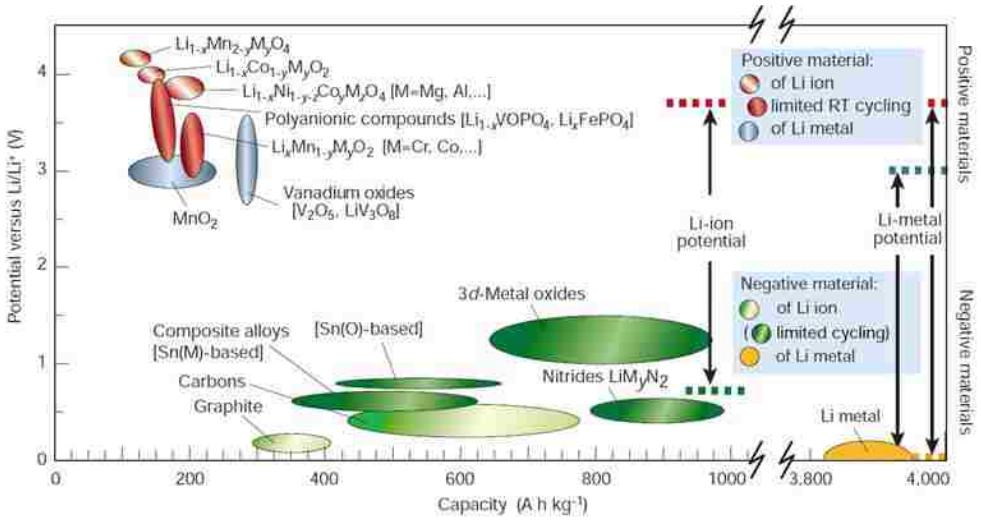

Figure 6 – Voltage produced by various different materials for both anode and cathode. Take note of the capacity for the negative materials and note the large discrepancy between lithium metal and the intercalation compounds. From ref (5).

One intercalation compound which has recently gained great popularity is lithium iron phosphate ($LiFePO_4$). This olivine structure was discovered at the University of Texas and has become the focus of many lithium ion research projects (27-33). The crystal structure of the $LiFePO_4$ cathode is olivine, which is simply an octahedron and tetrahedron which share corners as seen in Figure 7, from reference (29). This structure has a one dimensional "pore" within its framework which is where the lithium resides and can intercalate in and out of. The intercalation process of lithium into $LiFePO_4$ results in a small swelling of the crystalline network on the order of 6%, which is very minor compared to other intercalation compounds. The fact that the intercalation is very unobtrusive to the cathode results in a very flat discharge curve for $LiFePO_4$ based lithium ion batteries. The other main advantage of this cathode material is that it is iron and phosphate based, which is very environmentally friendly and the constituents are abundant. In contrast, some of the other intercalation compounds such as Co, Ni, and Mn have higher toxicities than iron.

The theoretical capacity for the lithium iron phosphate material is 170 mAh/g. The initial research for this redox couple showed that only 0.6 Li atom / formula unit could be intercalated, reducing the actual capacity greatly (27, 32). This intercalation follows the reaction upon discharge:

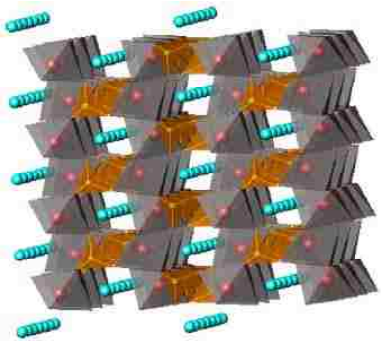

Figure 7 – Olivine structure of $LiFePO_4$. From ref (29).

$$FePO_4 + xLi^+ + xe^- \rightarrow xLiFePO_4 + (1-x)FePO_4 \quad (5)$$

where x is the fraction of lithium intercalated into the electrode (27, 32). The understanding of this partial intercalation has recently improved and cells are now able to come very close to the theoretical capacity of $LiFePO_4$ (30). The high energy density of this cathodic material coupled with the availability and non-toxic nature will play an essential role in the possible use of this material for printed battery application.

Application Specific Battery Design

To understand a printed battery and what utility or novel addition this would contribute to the field of battery research we must consider the job of an engineer when designing and choosing a power source. As shown in Figure 4, each type of battery chemistry has a certain design window which it occupies. This is not just the case for batteries but also applies to fuel cells, biofuel cells, and electrochemical capacitors. For each of these devices there must be an application in mind because the power demand of the application will exclude certain technologies. For example, devices which require very high current for low times may be suited to a capacitor over a battery and conversely devices which require long operation times would exclude the use of a capacitor as seen Figure 8 (34).

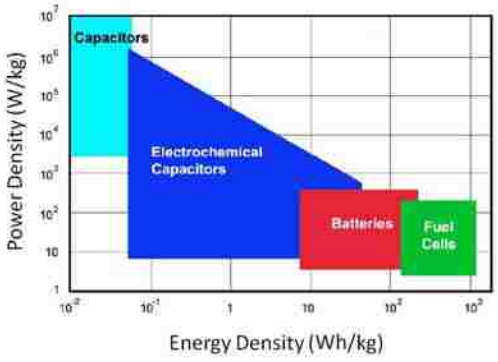

Figure 8 – Window for choices of technologies based on application design specifications. From ref (34).

By selecting the correct technology for the application, one can ensure that the power supplied by the technology will be sufficient. For applications that batteries are appropriate there are many choices for cells, most of which are commercial cells in the standard configurations mentioned in the next section of this manuscript. A problem arises, however, for applications which require small batteries. Since most of the standard cell configurations are macro scale, there is very little option for cells which are microscale and need to provide sufficient power. The only cells currently available commercially are thin film batteries. These have no real standardization for size or form factor. As the size requirements for the cells become smaller, the development of batteries becomes a matter of design for one specific application. This is to accommodate any geometric concerns the application may have. In this way, it is advantageous to have a method of making a cell which conforms to any geometry which may need portable power.

As the size of the battery reaches a lower limit, the amount of power it can produce also approaches zero. This can be seen in Figure 9, with data from Linden and Reddy (3). This trend in the energy density of a cell with respect to the volume of the cell intersects the x-axis at a critical point. This point corresponds to the situation where the cell has a finite volume but is unable to produce any power. This is due to the fact that the inert components within the cell take up a large portion of a battery's volume. When the battery can no longer produce power, the contents of the cell at that point become only inert components. The ability to step off of the trend line in Figure 9 and shift to the left of it on would allow for the creation of cells with much smaller volumes

which would still be able to produce energy. This could be an enabling technology for many applications which require very small cells that are capable of producing power.

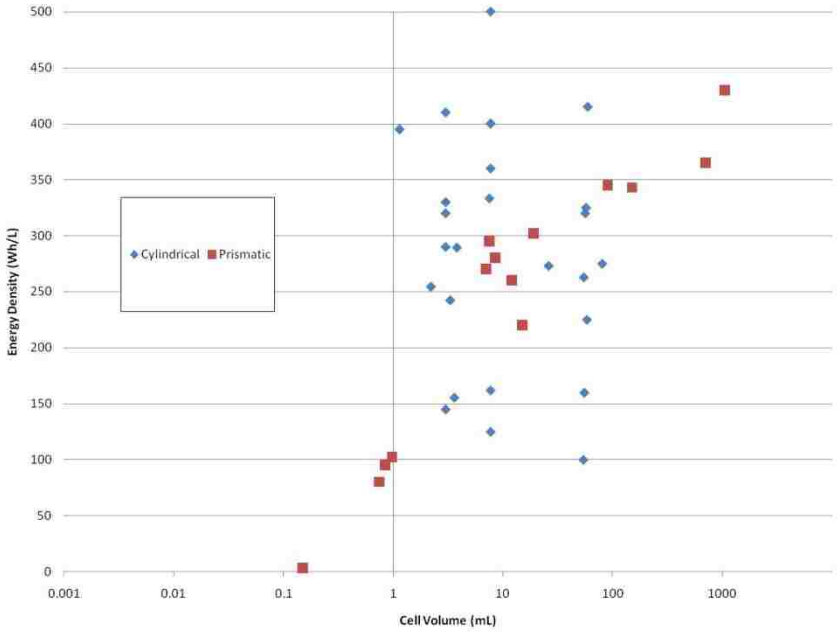

Figure 9 – Influence of battery size on energy density. Note that there is a critical volume where absolutely no energy is produced by the cell.

Traditional Geometries and Fabrication Techniques

Before discussing printed batteries, it is important to discuss more of the traditional battery fabrication techniques and their applications. A brief view of how batteries are made will help to identify a few of the challenges that printing a battery in-situ will help to alleviate.

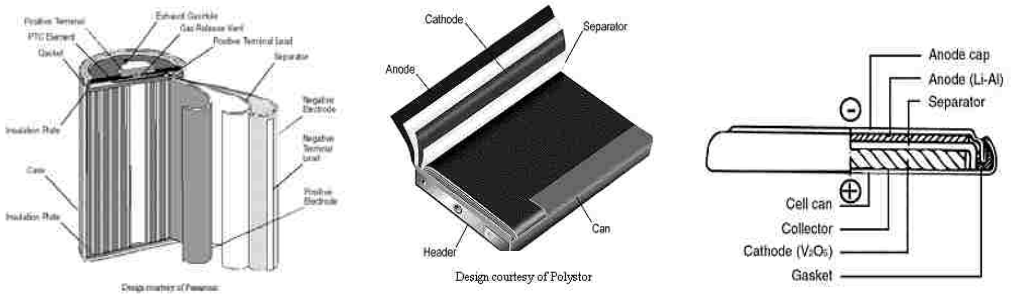

Figure 10 – Common construction layouts for lithium batteries. Shown from left to right are the cylindrical cell, the prismatic cell, and the button or coin cell. From ref (3).

For lithium batteries, there are 4 primary configurations for their construction which can be seen in Figure 10. The three traditional cell geometries are as see in reference (3). The cylindrical cell is essential a rectangular anode sheet, a rectangular separator, and a rectangular sheet for the cathode which are then rolled up into a cylinder. The electrode leads are connected to the top and the bottom of the cylindrical can by using a spark welder to attach the exposed shim material to the can itself. The entire assembly is then capped with a gasket between the two halves of the can assuring that there will be no shorting between the anode and cathode. These cells are the design used the most for consumer primary (and many secondary) batteries. The prismatic cell is the same stack of anode, separator, and cathode but is usually wound or stacked to produce a thin flat rectangular battery rather than a cylinder. Assembly of prismatic cells is very similar to that of a cylindrical cell but results in a thinner battery. This form factor is used often when a system is designed which necessitates the use of a thin cell. The button (or coin) cell is a small metal can that encapsulates the electrochemical material and is then sealed with a cap using a small o-ring to prevent shorting. This type of battery is most commonly known for hearing aid and small device type of applications.

The amount of active material and size of the coin cell is much smaller than both cylindrical and prismatic cells. This is due to the fact that most coin cells only contain one layer of active material, so their capacity comes only from the amount of material which can be placed within the geometric area of the cell. With prismatic and cylindrical cells, the active material is wound upon itself, which increases the use of space within the cell package. Efficiently winding multiple layers within the package increases the power output of the battery. Each of these types of cells has found a market for commercial use and is the current industry standards for their application.

The last main type of cell, which is very commonly used for research, is the pouch cell. In pouch cells, a heat sealable pouch is used as the casing instead of a metal can. This is advantageous primarily due to the ease of fabrication. The infrastructure needed for fabrication of a pouch cell is minimal, making it the ideal cell configuration for testing multiple changes to the battery. The pouch material is volumetrically much smaller than the metal cans of the other three types of cells. Also, there is no need for a gasket or o-ring to prevent shorting between the anode and cathode since each electrode can be sealed at a different point in the package. This type of cell is also easily manufactured and can be made to any size or geometry. There is no standard for pouch cell manufacturing, unlike button or cylindrical cells, so their use is primarily for research situations where quick comparison is needed between samples.

Whatever the form factor of the battery, most of the electrodes are made similarly. Typical electrode formulations consist of the electrochemically active material, a binder for electrode integrity, an additive to adjust the electronic transfer between the active site of the material and the current collector, and a solvent which is evaporated off during the

creation of the electrode. This slurry (or paste) is then deposited onto a current collector foil (aluminum or copper) and baked to remove the solvent either by tape casting or doctor blading the slurry onto the current collector. Each layer of the battery is made this way and each is processed separately. Then all the layers are cut to shape and then either stacked or rolled, depending on the form factor, into a complete cell (3).

During this drying and assembly process, there are several problems. The deposition of the electrode slurry and subsequent evaporation of the solvent can lead to local defects in the electrode layer itself. Battery performance is directly related to the ability for the manufacturer to optimize how the slurry is made into an electrode. This is compounded when the layers of the battery are assembled together. Battery performance is based upon the transport of the lithium ions from one intercalation compound to the other. The interface between layers of the cell can interfere with that transport and slow down or even stop the transport of ions across the battery, resulting in a high internal resistance or impedance and limiting the rate of discharge. In solid or polymer electrolyte batteries, this can be a very large problem that will easily prevent a battery from even functioning.

The traditional method for manufacturing of this type of cell is tape casting or doctor blading. This technique relies on using a blade (planar piece of metal) to slowly spread an even film of the material to be deposited on the substrate. This technique has been adapted for battery applications by using a reel to reel apparatus for the substrate so that large areas may be coated at once. Using this reel technique relies on having a drying unit operation in serial with the doctor blading itself. This is to prevent un-dried slurry from entering the final product roll, as it would destroy the electrode if wound

upon itself in the wet form. A schematic representation of this technique can be seen in Figure 11. This technique is very commonly used in commercial applications for deposition of a linear layer of materials (35). Deposition of unique geometries is difficult using this technique due to the design constraints for the blade. Any change in the desired deposition requires a new blade, which means changing the blade several times during deposition for more complex geometries than a square thin film. Additionally, changing the blade during a deposition process using doctor blading will result in a disconnected or a disjointed film.

The control that is built into this technique is similar to the controls that will be seen in the robocasting technique discussed later. The speed of horizontal travel can be controlled by changing the speed at which the reel to reel substrate rolls moves. The vertical thickness of the film is controlled by the distance between the doctor blade and the substrate, indicated by the letter h in Figure 11. It should be noted that this vertical distance is dependent on the slurry being cast. This can be for a multitude of

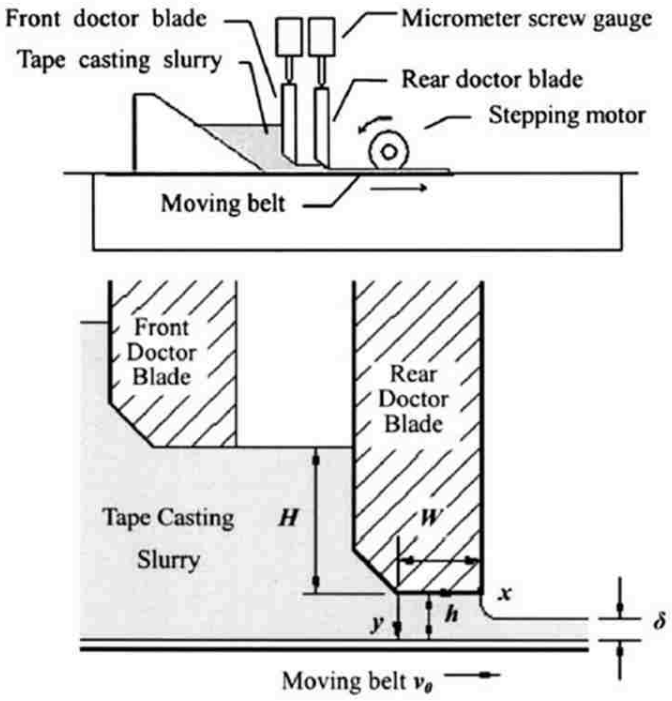

Figure 11 – The doctor blade technique. Note the use of a roll for the substrate on which the deposition is made. From ref (35).

reasons including the amount of solvent used in the slurry, the particle size of material within the slurry, and the rheological properties of the slurry (dilatant, pseudoplastic, and Newtonian). The final film also will not be the same height as h in the figure, since the film will go through a drying process immediately after deposition so the thickness of the film will depend on the solvent loading. Solutions which contain higher percentage of volatile components will thin greatly during drying of the film. This remains up to the engineer for design on a case by case basis on the solid loading of the slurry and how much the film will thin to optimize the doctor blade to substrate gap in order to achieve the desired film thickness.

Doctor blading provides a convenient way to deposit uniform films on a substrate and can achieve a very high throughput due to the continuous nature of the deposition. The obvious limitation in the technique is the ability for it to produce non-standard geometries. Since the deposition is continuous there is no room for changing widths or heights of the blade, therefore anything other than a singular line is excluded.

Thin Film Batteries

Thin film batteries are a new type of battery that has gained attention due to the fact that the all of the layers in the battery are between microns and hundreds of microns in thickness (36). This makes for batteries which must have high energy density electrochemical species otherwise the battery would not have enough power to be usable. This is why one of the focuses of thin film battery technology is the thin film lithium battery. In thin film batteries, where the overall thickness of the battery is hundreds of

microns and the amount of active material is relatively small, the problem of interfacial transport limitations is especially troublesome. Thin film batteries have been designed for use in small portable power applications where size and form factor are an issue (37-39).

Most of the techniques used for thin film batteries are not applicable to normal battery manufacturing demands. A typical schematic for thin film batteries can be seen in Figure 12. These are typically based on some sort of sputtering technique, which is not amenable to the rapid production needed for commercialization, see Figure 12 (36). Sputtering techniques are able to produce very thin films which are incredibly uniform, which produces very good battery discharge characteristics. These techniques include, but are not limited to vacuum thermal vapor deposition (VD), RF sputtering (RFS), RF magnetron sputtering (RFMS), chemical vapor deposition (CVD), electrostatic spray deposition (ESD), and pulsed laser deposition (PLD) (36). There are a few research groups looking at the deposition of lithium intercalation compounds for thin film batteries, but typically the substrates are not amenable for use in flexible applications. The Oak Ridge National Laboratory thin film battery exhibits good performance, but is usually on an alumina or glass substrate (40-43).

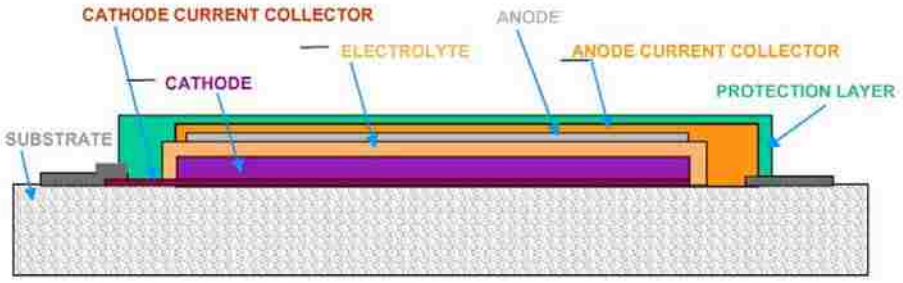

Figure 12 – Schematic for a typical thin film battery manufactured using sputtering techniques. The resulting structure closely resembles silicon wafer processing architectures. From ref (36)

This thin-film battery from the Oak Ridge National Laboratories has actually seen commercial success and uses a lithium phosphorus onynitride (LiPON) separator / electrolyte. Since the initial research into LiPON cells, this solid electrolyte material has become a very large part of the industry for small form-factor cells (44). This chemical setup focuses on the gas phase deposition of the solid electrolyte separator for use with various different anodes and cathodes. The ability for this material to be deposited using the previous mentioned techniques allows for creation of a cell which is comprised of a large percentage of active material compared to the traditional geometries used for cells such as alkaline batteries. Table 1 shows a comparison of the available thin film batteries and their characteristics, from Patil et al (36). There is an overwhelming favor towards use of LiPON cells due to the current understanding and processing of this material. The other materials listed are more research oriented and have yet to be fully realized as commercial cells, but will likely see that occur shortly.

Table 1 – Thin Film Battery Comparison.

Anode	Electrolyte	Cathode	Voltage (V)	Current ($\mu A/cm^2$)	Capacity	Reference
Li	$Li_{3.6}Si_{0.6}P_{0.4}O_4$	TiS_2	2.5	16	45-150 $\mu Ah/cm^2$	(45)
Li	$Li_{3.6}Si_{0.6}P_{0.4}O_4$	TiS_2	2.5	16-30	-	(46)
Li	$Li_{3.6}Si_{0.6}P_{0.4}O_4$	WO_3-V_2O_5	1.8-2.2	16	60-92 Ah/cm^2	(47)
Li	$LiBO_2$	In_2Se_3	1.2	0.1	-	(47)
Li	Li_2SO_4-Li_2O-B_2O_3	TiS_xO_y	2.6	1-60	40-15 $\mu Ah/cm^2$	(48)
Li	Li_2S-SiS_2-P_2S_5	V_2O_5-TeO_2	2.8-3.1	0.5-2	-	(49)
LiV_2O_5	LiPON	V_2O_5	3.5-3.6	10	6 $\mu Ah/cm^2$	(50)
V_2O_5	LiPON	$LiMn_2O_4$	3.5-1	>2	18 $\mu Ah/cm^2$	(51)
Li/LiI	LiI-Li_2S-P_2S_5-P_2O_5	TiS_2	1.8-2.8	300	70 mAh/cm^3	(52)
Li	LiBP, LiPON	$LiMn_2O_4$	3.5-4.5	70	100 mAh/g	(53)
Li	$Li_{6.1}V_{0.61}Si_{0.39}O_{5.36}$	$MoO_{2.89}$	2.8	20	60 $\mu Ah/cm^2$	(54)
Li	$Li_{6.1}V_{0.61}Si_{0.39}O_{5.36}$	$LiMn_2O_4$	3.5-5	10	33.3 $\mu Ah/cm^2$	(55)
Li	LiPON	$LiMn_2O_4$	4.5-2.5	2-40	11-81 $\mu Ah/cm^2$	(56)
Cu	LiPON	$LiCo_2O_2$	4.2-3.5	1-5	130 $\mu Ah/cm^2$	(43)
Li	LiPON	$LiCo_2O_2$	4.2-2.0	50-400	35 $\mu Ah/cm^2$	(57)
Li	LiPON	$Li_x(Mn_yNi_{1-y})_{2-x}O_2$	4-3.5	1-10	100 mAh/g	(58, 59)
Li	LiPON	$LiMn_2O_4$	4-5.3	10	10-30 $\mu Ah/cm^2$	(60)
Li	LiPON	Li-V_2O_5	1.5-3	2-40	10-20 $\mu Ah/cm^2$	(61)
SiSnON	LiPON	$LiCo_2O_2$	2.7-4.2	~5000	340-450 mAh/g	(62)
Li	LiPON	$LiMn_2O_4$	4.3-3.7	~800	45 $\mu Ah/(cm^2-\mu m)$	(63)
SnO	$Li_{6.1}V_{0.61}Si_{0.39}O_{5.36}$	$LiCo_2O_2$	2.7-1.5	10-200	4-10 $\mu Ah/cm^2$	(52)

The schematic show in Figure 12 shows the generic build for thin film batteries, but the encapsulant used is often overlooked. This is a very important part of a battery, and in traditional configurations is the constituent which constitutes the majority of the volume within a cell. This encapsulant or protective layer in thin film batteries is mostly commonly made through sputtering of parylene C or deposition of some sort of

thermoplastic (39, 64). The characteristics of this layer are that it needs to be impervious to oxygen and water, electrochemically inactive in the window for lithium redox reactions, flexible enough for use in a particular application, and have proper adhesion to the underlying substrate so as to exclude diffusion of contaminants (oxygen and water) into the cell.

Robocasting Technique

The technique known as robocasting is an in house technique used at Sandia National Laboratories which has been previously described (65-71). The technique involves the use of independently driven motors for the three physical dimensions and a method for the deposition of material. Typical deposition of materials uses 3 axis (x,y,z) to control the position of a print nozzle in relation to a substrate. This deposition can be either physical extrusion through a deposition tip or an atomization of material for a vapor phase deposition. The method provides for control of extrusion rates through the use of a linear slide attached to a stepper motor. Using this setup, the deposition

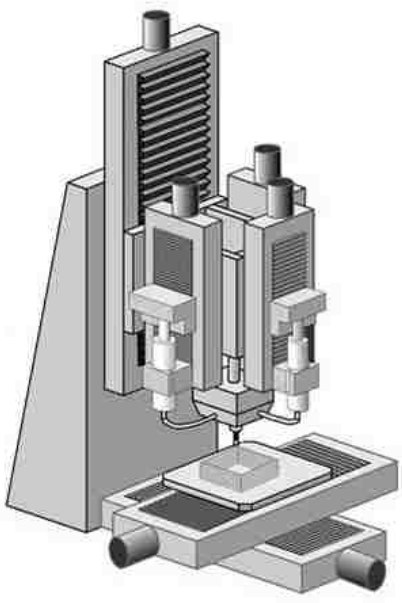

Figure 13 – Schematic representation of a robocasting machine. The control of position is base on the stage (where the square feature is in diagram) movement in x/y axis and the position of the tip in the z axis.

rate can be specified to provide a uniform amount of material during the extrusion process. This is normally done using a syringe attached to a tip of know diameter. The diameter of this tip dictates the size of the extruded "bead" of material. The overlap can be precisely controlled for each bead, creating a film of material which is created by multiple passes along the substrate. The extrusion method works very well for slurry formulation with higher viscosities since atomization of such slurries is difficult.

Along with control of movement in 3 axis (x, y, z) there is also capability with the robocasting technique to control an addition 2 axis with use of an additional sub-stage which attaches directly on top of the normal 3 axis stage as seen in Figure 13. These two additional axis provide control of movement in both θ and φ (the zenith or polar/inclination angle and azimuth/azimuthal angle reference in spherical coordinates). Control of deposition in both traditional Cartesian coordinates and subsequent spherical coordinates allows for control of motion in any geometry available. Deposition in up to 5 degrees of motion is a unique technique and relies on the robocasting technology to make features which are much more complex than traditional machining techniques allow. The slides on the robot have a resolution of ~ 2 μm, allowing for precise control over positioning during deposition processes. A simple example of a structure that robocasting can create which typical machining technologies cannot is the lattice, as seen in Figure 14. Part of the reason this technique can make unique structures is because it is a bottom up technique where material is added to the part until the cast process is

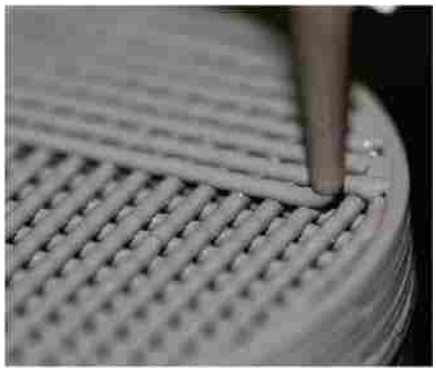

Figure 14 - Robocasting example of a part being casted using the extrusion technique.

complete. All traditional machining techniques are bottom down type of processes where material is taken away until the part is left.

The robocasting technique was initially developed and used for deposition of ceramic materials. These materials exhibit high viscosities and require a relatively large amount of post print processing in order to sinter or anneal the printed slurry into a full ceramic material. Since that time, the technique has expanded towards many more material sets and applications. There have been several applications where the robocasting technique was used to enable fabrication of parts (72-75). All of the techniques rely on development of an ink or slurry which is compatible with the deposition technique whether it is aerosol deposition, spray deposition, or slurry extrusion. Figure 15 shows a few examples of materials which have been printed using the robocasting technique which are appropriate for discussions about printing of battery materials. The examples shown in are not a comprehensive list of applications of the robocasting technique, but do provide some insight into the ability for the technique to be used with a number of material types (polymers, metals, insulators) on a wide range of substrates (polymers, ceramics, metals, plastics, and wafer based technology). Note the ability for the technique to be printed on planar substrates, curved substrates, and even a fully circular substrate. This unique ability for the technique to be used with a wide range of materials on a wide range of substrates in virtually any configuration makes it ideal for use in this work.

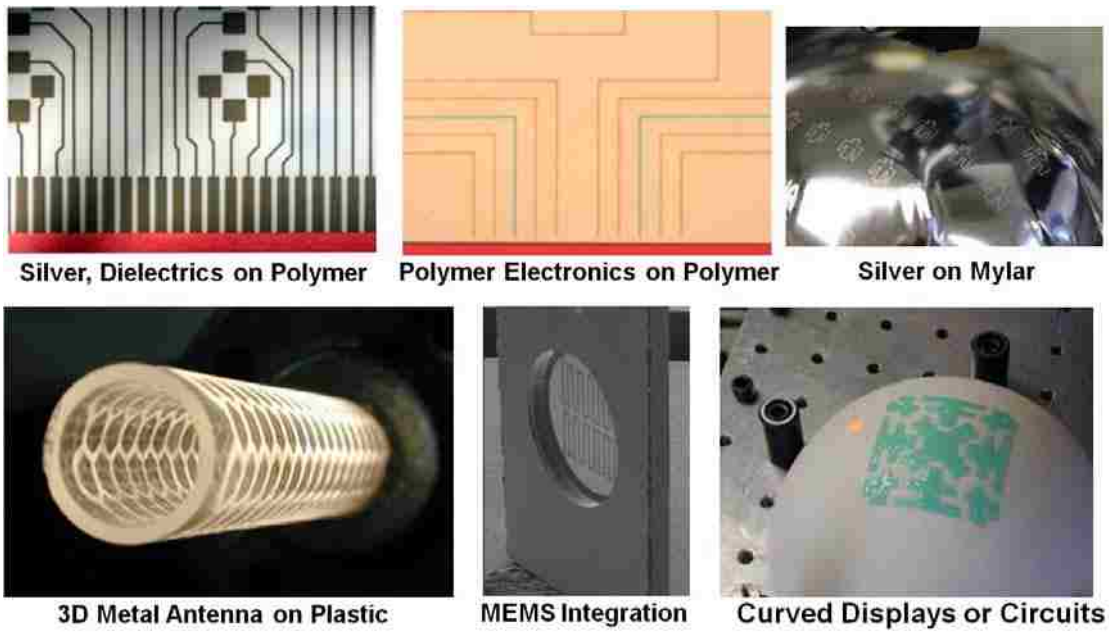

Figure 15 – Examples of materials and features made using the robocasting technique. Examples show the deposition of silver, dielectrics, and polymers on a variety of substrates including planar and non-planar examples of polymers, plastics, ceramics, and wafer based technologies.

Robocasting is not the only "direct-write" technique that is used for fabrication and prototyping of parts in unique geometries. Several techniques and companies have emerged in recent years which use techniques similar to robocasting to deposit materials in a similar fashion. These techniques include nScrypt Inc, Maple, BAE Systems, Mesoscribe, Dip-pen lithography, and Ink-jet spray techniques. These technologies use similar techniques to robocasting, but lack sophistication in placing the end effector tip in three dimensional space. Part of the reason this is the case is because the robocasting technique uses a control software package called Toothpaste, which was developed with Sankel software (http://sankelsoftware.com/) to control the movement of the robocaster machines. This software allows for planning of movement paths along virtually any trajectory that can be imagined for printing of a part. This software package expedites

the introduction of an arbitrary movement path for the robotics and allows for rapid printing and prototyping using the extrusion printing technique through an easy and user friendly graphical user interface (GUI) as seen in Figure 16.

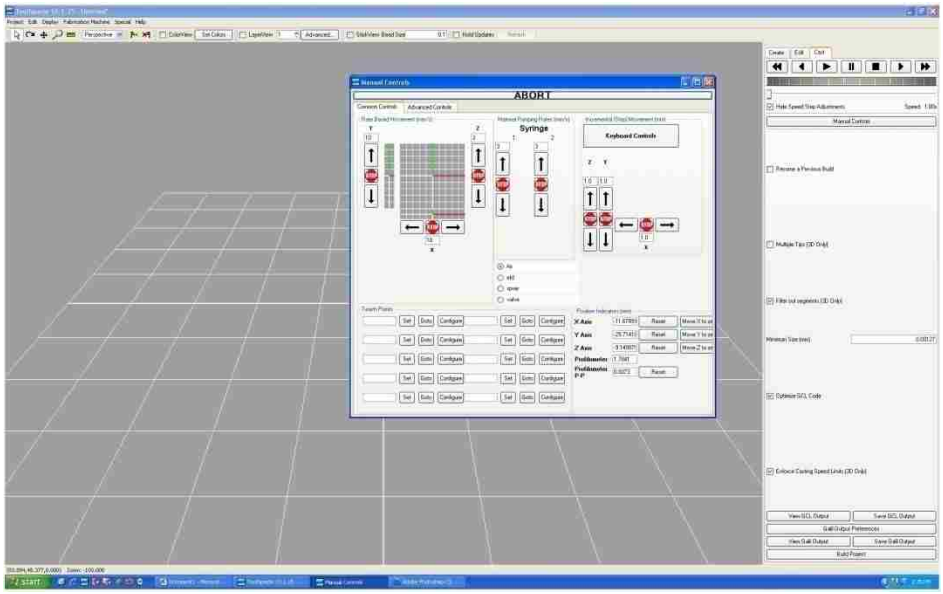

Figure 16 – Graphical user interface for robocasting control program Toothpaste. Shown is the main interface and the casting menu which can control motion in x, y, and z axis on demand. Input of this system is designed for easy fabrication of most any geometry allowing for quick prototyping of unique parts.

Along with the extrusion method for deposition of material from the nozzle of the robocasting machine, there is also an aerosol technique which is employed for deposition of materials. The aerosol method for deposition of materials uses an Optomec M3D system for handling of materials and the robocaster to handle the positioning and movement (http://www.optomec.com/), as seen in Figure 17. The Optomec M3D system has 2 methods for creation of an aerosol stream. The first is an ultrasonic bath, in which a vial of the solution to be printed is placed. The ultrasonic waves are transmitted from the system through a bath of water and into the printing solution. At the correct height

and power, this will cause a fine mist of aerosolized particles to appear within the vial. These particles are then picked up by a carrier gas and sent towards the print tip where they are focused down using a sheath flow of carrier gas to focus the print diameter down as low as ~ 25 μm. The second method of aerosolization is a pneumatic method in which a vial of the printing solution is placed on the system. A gas stream then picks up the solution by passing along a small orifice in the reservoir, as seen in Figure 18. The stream of aerosolized particles are then treated the same as the ultrasonic method, they are focused using an annular sheath flow to focus the print stream down to a fine feature size.

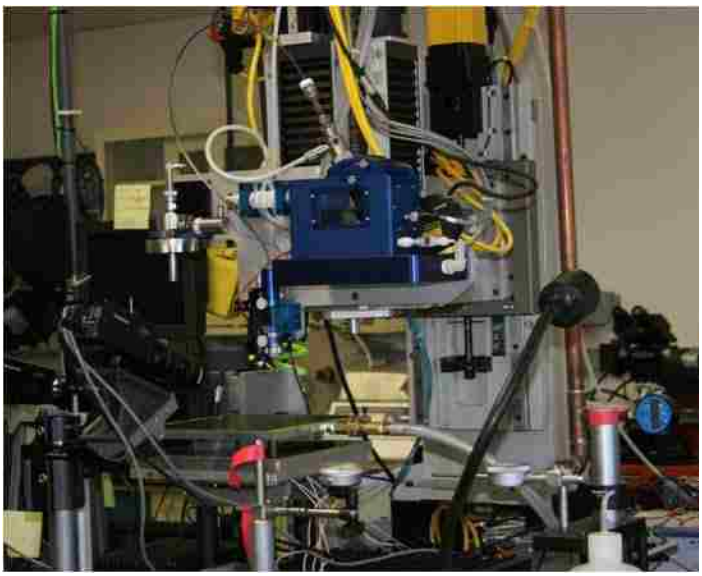

Figure 17 – Optomec M3D system mounted onto a robocasting robot.

The main difference between the two aerosol techniques is the amount of solution that they require to work. The sheath focusing of the print stream is the same in both aerosolization techniques, so they both result in a similar resolution or print size. The reservoir for the ultrasonic method can hold several mL of ink, but tend to work best at

around 1 mL of solution. If more ink is in the vial, then the coupling of the ultrasonic energy with the ink solution does not work as effectively. If less ink is used, then the energy put into the ink by the ultrasonic atomization can drastically change the temperature of the solution, which changes the viscosity and how well it can be atomized. This will often render a solution unable to be aerosolized by ultrasonic atomization. The pneumatic technique requires at least 10 mL of ink to be present. This is due to the fact that the location of the orifice for atomization is part way up the vial. This technique is very difficult to use when printing an expensive ink, and may be the deciding factor for which technique to be used.

The amount of ink which is picked up by the pneumatic technique is also quite a bit greater than that of the ultrasonic technique. The result of this is a print which has the same resolution using the two techniques, but the print done using the pneumatic system will be thicker than the ultrasonic. Typical print heights for the ultrasonic technique are ~ 1 μm, and for the pneumatic are ~ 3 μm.

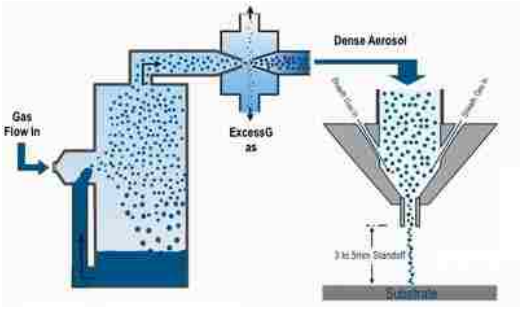

Figure 18 – Schematic of how pneumatic aerosolization works.

Since the robocasting technique allows for precise control of motion, up to 2 μm resolution, it is ideal for creation of features which have geometries in virtually any shape or size. This means that the use of robocasting for lithium battery manufacturing would allow for the integration of portable power into devices with demanding geometries. The robocast technique would allow for the deposition of electrochemically active materials for batteries to be deposited

in virtually any area and even allow for the conformal printing of battery materials over topography or unusual surfaces. The robocasting software also allows for the creation of a 3 dimensional tool path to follow, so the printing of electrochemical species could be conformal to three dimensional objects, not just planar geometries. In this way, the robocast battery could be tailored to any application, including those that need a battery to be retrofit into places where one was not planned.

Motivation for Robocast Deposition of Battery Materials

The development and characterization of lithium electrode (both anode and cathode) materials has been the major research push in lithium battery research. Many publications have emerged recently (~ 10 years) that attempt to describe and characterize all aspects of battery performance using a wide variety of materials (27, 29, 32, 60, 76-81). The body of work is too extensive to explicitly mention, but the publications number easily in the many thousands of publications. The field of materials engineering and characterization is vast for lithium batteries and is continually expanding, resulting in expanding capabilities for batteries in terms of capacity and rate capability based solely on materials engineering. The broad knowledge base for lithium batteries has resulted in many efforts to minimize the size of the lithium battery. This work became a new thin-film battery research thrust which attempted to make ultra thin batteries using many techniques and materials with quite a bit of overlap with the traditional materials research for lithium cells (45, 47, 52, 55, 56, 61, 82-87). Many hundreds of publications have emerged detailing the fabrication techniques and characterization of these types of

batteries. The research thrust of minimization of battery thickness has resulted in many achievements including the commercially viable fabrication of lithium phosphorus oxynitride (LiPON) cells (41, 44, 88-90).

The subject of the capability to print lithium cells, the package materials for lithium cells, and novel separators for lithium batteries are far less common than the development of electrode materials and thin film batteries. The development of new and unique lithium battery separators has been researched and a few hundred publications have emerged detailing techniques and materials for new separators (44, 83, 91-94). This includes the very popular polymer electrolyte poly(ethylene oxide) (PEO), which has gained notoriety as a viable material for use as a solid electrolyte in lithium batteries. Generally, the battery industry has relied on several methodologies and products for the bulk of the separators used for fabrication. While this is an acceptable practice, there are potential breakthroughs in this research area to be made, as seen from the widespread adoption of LiPON as a separator. Research in this area may make it possible for adoption of an entirely new type of lithium battery separator for common fabrication use in the future.

Aside from the electrodes and separator within a cell, the package is the last detail needed to complete the full cell and one of the least explored details. Almost every research endeavor in the field of batteries has excluded this portion of the cell, since it is the most standardized in the industry. While the standardization allows for comparison between research efforts, alternative package schematics offer benefits in regards to the flexibility of batteries to be manufactured towards applications and form factors that may not be otherwise available with standard cell geometries. A few dozen publications have

emerged that have tackled this portion of the lithium battery, but the literature is scarce with respect to this area of investigation (39, 64, 95, 96).

The ability to print components of the lithium battery cell has contributed a small set of knowledge towards the general research and understanding of lithium batteries. There have been several genuine attempts to describe alternative techniques for the printing of lithium batteries using non-traditional methods, but the literature is very sparse compared to the other considerations for lithium battery development (97-99). Additionally, the ability to print separators or package materials is virtually absent from the literature and recent publications in the area are rare. The ability to print battery components (any of the constituents of a battery) could enable for rapid manufacturing of a lithium battery cell and could potentially alter the way cells are made for portable power applications. An example along that line of thinking can be seen in the development of lithium paper batteries (100) as well as efforts to electrospin materials for lithium batteries (101, 102).

The use of the robocast deposition technique for printing of lithium battery materials attempts to establish a new method for fabrication of manufacturing of lithium batteries. While the electrochemical evaluation techniques used in this work remain more traditional in their approach, the concept of printing a unified cathode and separator for use in a lithium battery is quite unique. The small amount of literature in the field of printing lithium battery materials shows the infancy of the idea and technology behind this work. The existing knowledge that is contained in the robocasting technique allows for the immediate use of the technique for this novel purpose and aims to develop knowledge about the performance of printed batteries. The development and maturity of

a lithium battery technology using this technique could greatly contribute to the development of a new type of manufacturing process for lithium cells which could be tailored to suit the application based on the flexibility of the deposition technique when multiple components of the lithium battery are printed.

CHAPTER 2: GOALS AND OBJECTIVES

The use of the robocasting technique to print battery materials would enable the printing of batteries onto non-planar surfaces and in countless geometrical designs. This design flexibility would allow for the use of small volume printed batteries in novel applications. The overarching goal for this work began with Figure 9. The goal was to design a battery which has minimal volume and reasonable specific energy and capacity. The ability to print the active material while retaining reasonable power is also a very attractive goal. The specific balance between these two is the unknown for this type of work. It is unknown if, by printing battery components, retention of battery energy or capacity is possible. The ability to print a material may exclude materials which can produce large amounts of useable power. The understanding of how this balance is the overarching goal for this work.

The basis for the balance between power and printability begins with isolation of the components. The cathode rheology and formulation needs to be explored to be used with the printing technique. This understanding begins with standard battery cathode slurry formulations, which give the cells an optimal chance for battery performance. This will be achieved by application of rheological measurements and SEM microscopy to determine the structure of the material when printed. The goal for the physical characterization techniques is to understand the morphology of the printed material and to identify (if any) drawbacks for deposition of the material using the robocasting technique. The electrochemical and physical characteristics of the cathode need to be investigated. This entails the fabrication of cells and electrochemical cycling in a controlled manner.

This will be accomplished by standardization of cell sizes and forces by use of the traditional 2032 coin cell form factor for the batteries. The electrochemical investigation will evaluate cycling data, impedance measurements, rate capability, and lifetime performance to understand the ability for the printed cathodes for use in cells.

The other main component of the cell, which is much less researched and is the primary objective for this work, is a printable separator. The identification of a suitable material for both battery compatibility and printing performance is important for the development of a stack which will work in conjunction with a printed cathode. Evaluation of materials which emulate the commercially used separators and most highly researched separators will be the aim for the materials set. The difficulty in emulation of commercial separators is the formation of the pores in the polymer film, which is often done through physical stretching. Identification of suitable materials for printable separators will be based on rheological data and print tests to determine the optimal material and printing parameters. Since most commercial separators include a post extrusion step to induce pore formation, which is impossible when developing a printed separator, an alternative method must be used for pore formation. The main idea for pore formation explored in this work is the addition of a porous component to the printable slurry. The electrochemical performance of the printed separator and understanding of how that performance relates to commercial separators will be examined through electrochemical charging and discharging and EIS techniques. Physical examination of the separator materials will also be conducted using electron microscopy. Any new behavior for printed separators will be examined through comparison with traditional theory for battery cycling based upon experimental results.

Another goal for the development of a printed cell is to understand if there is an effect in battery performance due to the layers within the cell being printed on top of each other as opposed to being placed upon each other during cell assembly. Understanding the effect of the printing on the behavior of a printable battery separator is paramount to further implementations of this technique. This will be investigated by use of EIS impedance measurements.

While the development of a fully printable battery including the package and the current collectors is an ideal goal, the evaluation of printable current collectors and a printable package are beyond the scope of this project, but are directly tied to the results that emerge from the cathode and separator printing. This is because both the act of printing battery components as well as the materials choice for both the cathode and separator will impact the overall performance of a battery. Any change in layer formation and battery performance gained or lost by printing will be a factor when printing additional battery layers such as the current collectors or package. This behavior is evident even in traditional battery fabrication techniques, where intermediate preparation steps for interfaces or materials can have a dramatic effect on the battery capacity or rate capability.

Lastly, the objective of developing this printable cathode and separator is to identify if these techniques and materials are capable of battery operation which minimizes cell volume and maximized cell performance as compared to other techniques. The development of competitive battery performance from a cell based on the robocasting technique will be a very optimal result, due to the highly customizable nature

of the printing technique. Development of printable battery with the robocasting technique may enable new applications for printable lithium batteries.

CHAPTER 3: MATERIALS AND EVALUATION TECHNIQUES

The difficulty in acquiring many of the materials required to do research in batteries is that there are very few companies who produce battery materials that sell them commercially. Many of the formulations are proprietary for their product lines and are considered a trade secret for the company itself. The collaboration with Sandia National Laboratories was essential in enabling the acquisition of knowledge and materials needed for this work.

Materials

Deposition of all materials was done using the robocasting machine as described previously in the section titled “Robocasting Technique”. Deposition tips were obtained from Nordson EFD (Westlake, Ohio). Deposition syringes were obtained from both Nordson EFD and Beckson Dickson (Franklin Lakes, NJ). Polypropylene, toluene, polyethylene oxide, all synthesis chemical for silica aerogel, acetonitrile, and xylene were obtained from Sigma Aldrich (St. Louis, MO). Battery electrolyte was obtained from Novolyte Technologies (Cleveland, Ohio). Alumina aerogel was provided by Sasol. Chlorinated polyolefin polymer was provided by Phibrochem LLC (Dalton, GA). All standard laboratory supplies were obtained from Sigma Aldrich and VWR (West Chester, PA). Lithium was obtained from FMC Lithium (Charlotte, NC).

The primary instrument used for all electrochemical cycling tests was the Maccor battery test system, Maccor Inc. (Tulsa, OK). Potientiostats used were obtained from

both Princeton Applied Research (Oak Ridge, TN) and BASi (West Lafayette, IN). Frequency response analyzers were obtained from Solartron (Hampshire, UK). Rheological data was acquired using rheometer equipment from Bohlin (Malvern Instruments Ltd, Worcestershire, UK) and TA Instruments (Wilmington, DE). Profilometry was done using equipment from Detak (Veeco, Plainview, NY). Electron microscopy was done with a microscope from Hitachi High Technologies America, Inc. (Schaumburg, IL) equipped with EDS capabilities from Princeton Gamma Tech (Princeton, NJ).

Cyclic Voltammetry

The most widely used technique for evaluation of electrochemically active systems is cyclic voltammetry. It is often the first experiment performed when working with electrochemical reactions, which includes batteries. It provides information about several important parameters of a reaction including thermodynamics of the redox process and kinetics of the electron transport occurring within the system (3, 104, 105). This technique is traditionally done using a three electrode system. The working electrode is where the redox reaction of interest takes place. The voltage of the working electrode is adjusted based on the reference electrode, which is a standard reversible couple with facile kinetics that is used as a standard, nonpolarizable reference potential. There are many popular reference electrodes used for analytical

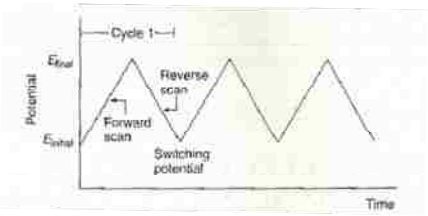

Figure 19 – Scan profile for cyclic voltammetry. From ref (103).

electrochemistry, each has a specific electrochemical potential and is used for various different situations. The counter electrode is used to collect current between itself and the working electrode. The potential is then swept in a triangular wave form between two vertex potentials as seen in Figure 19, usually this is cycled several times, and the current is measured to result in a cyclic voltammogram as seen in Figure 20 (103).

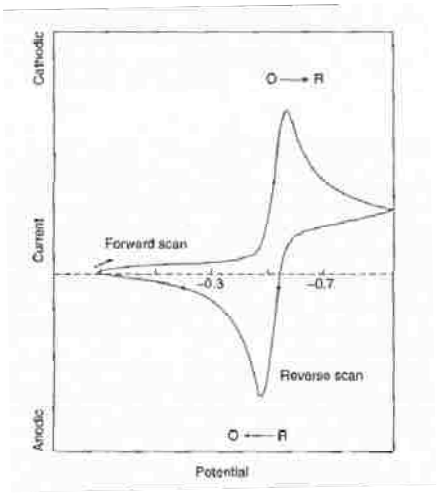

Figure 20 – Example of a cyclic voltammogram. From ref (103).

The peaks correspond to the formation of either the oxidized or reduced species. This peak drops off as the scan moves to higher potentials because there is a diffusion limitation for fresh molecules to react on the electrode. The current shown during these peaks for a reversible reaction is given by the Randles-Sevcik equation:

$$i = (2.69x10^5)n^{3/2}ACD^{1/2}v^{1/2} \quad (6)$$

where i is the current produced, n is the number of electrons transferred in the process, A is the surface area of the electrode (in cm^2), C is the concentration of the species (in mol/cm^3), D is the diffusion coefficient (in cm^2/s), and v is the scan rate of the voltammogram (in V/s). This is only valid for a reversible reaction. These reactions also exhibit the behavior that the peak height for the reductive sweep and the oxidative sweep should be identical. Also, the number of electrons transferred in the reaction can be

experimentally obtained by looking at the peak to peak separation. The separation (in volts) is given by:

$$\Delta E = \frac{0.059}{n} \tag{7}$$

This technique is useful in investigation of lithium battery performance, since it can be used to identify several characteristics of the system. It is capable of showing the potential at which the redox reactions are occurring. Additional peaks or redox couples indicate presence of impurities or of additional oxidations or reductions. Shifts in the position of the peaks indicates a non-reversible reaction is occurring during the Li/Li+ reaction, which is highly undesirable for secondary batteries as that indicates the battery will have short lifetime performance. An example of a simple cyclic voltammogram using $LiFePO_4$ is shown in Figure 21, from (28). Note the potential of the primary red curves, which indicate that there will be a slight difference in potential for this between the charge and discharge cycle. Also, the formal potential for this type of system is considered to be the average between the two potentials. In this example, that potential is a formal cycling potential of 3.4 volts, which is the generally accepted value for $LiFePO_4$. By using cyclic voltammetry, one

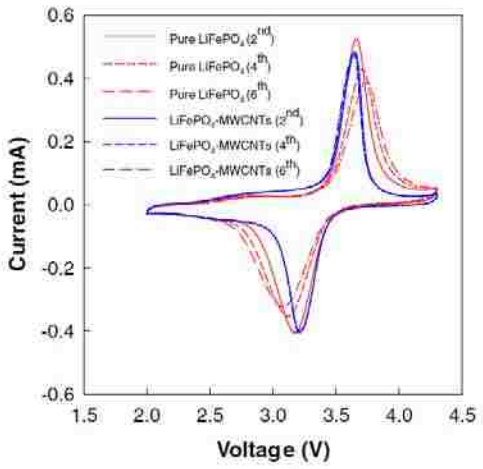

Figure 21 – Cyclic voltammetry of battery using $LiFePO_4$ cathodes. Investigation shows the change in redox potential and current with the addition of carbon multi-walled nanotubes. From ref (28).

can investigate what reactions are actually occurring within the cell and use it to screen for unwanted or side reactions which are undesirable. This is a common technique use to identify what exactly is happening within the cell as well as the components which are compatible with the electrolytes used in lithium cells.

Battery Charge / Discharge Cycling and the Influence on Discharge Curves

When evaluating a battery the primary interest is how the battery discharges or delivers power. For secondary batteries, there is also great interest in how well the battery can cycle over many repetitive charge/discharge cycles. This is especially interesting with lithium cells, due to the additional concern for dendrite growth within the cell after many cycles (7, 19).

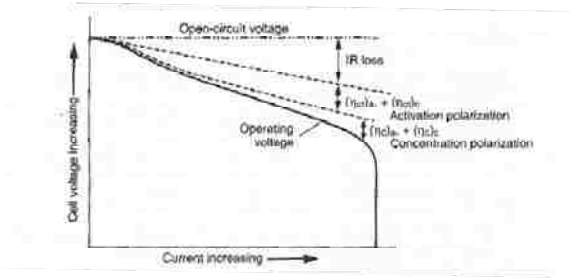

Figure 22 – Change in potential within a cell during discharge operation. From ref (3).

As mentioned previously, in the section titled "Battery Performance and Capacity," there are many factors that lessen the capacity that a fabricated cell will have. These are typically discussed as physical parameters such as fabrication techniques, materials, and handling of unit operations during production. These effects all contribute to the reduction of the potential of the cell as seen in Figure 22. A cell which cycled ideally with no loss in performance would stay as a straight line at the open-circuit potential until all of the lithium within the cell was used, then the voltage would drop drastically. In reality, there are several types of loss that are experienced within the cell, and the potential therefore

drops off significantly with current and time. The other factor that can affect how a cell performs is the cycling of the cell during testing (3, 83, 106, 107). Figure 23 shows an example of how the setup of the discharge conditions has an effect on the overall outcome of the profile.

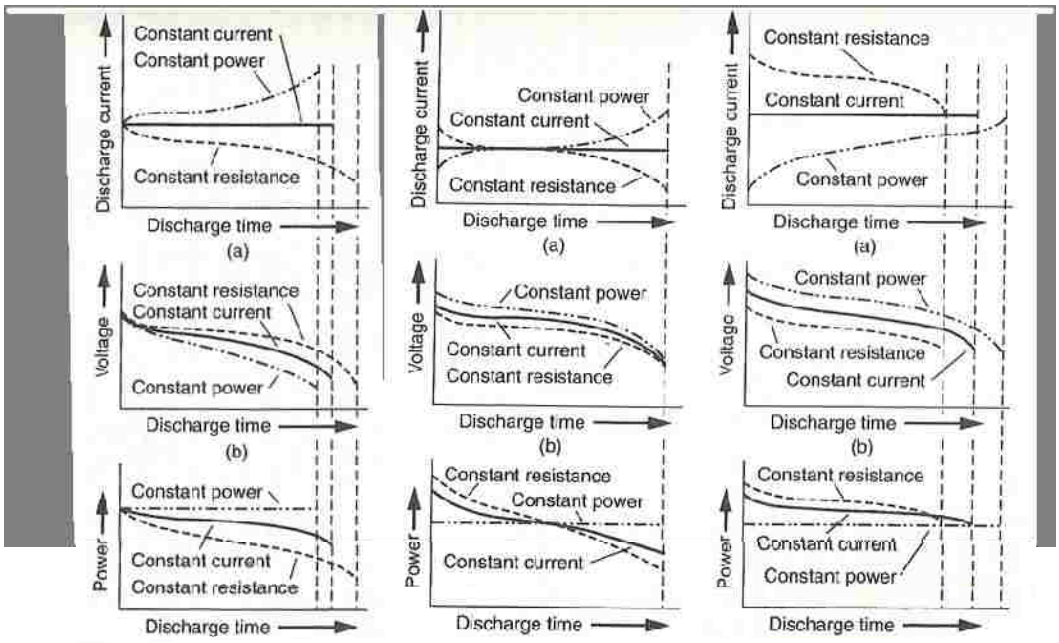

Figure 23 – Different discharge modes and their effect on the resulting battery discharge curve. Left is the case of constant current and power at the start of the discharge, shown are (a) current, (b) voltage, and (c) power profiles. Middle is the case of constant discharge time, shown are (a) current, (b) voltage, and (c) power profiles. Right is the case of constant current and power at the end of the discharge, shown are (a) current, (b) voltage, and (c) power profiles. From ref (3).

It can be seen from Figure 23 the discharge profile for a battery is very dependent on how the testing is performed. It is important to set up each cell that is made for this work in the same way, to insure that differences from cell to cell are only based on

physical parameters such as porosity and thickness, rather than a difference based up testing setup.

This is the primary technique used for evaluation of the printed components of the robocast battery. This was used at varying rates to understand the capability for the cells to produce power and current. The figure of merit that will most often be used will be capacity, with the exception of rate tests, which are used to determine how quickly the cells drop to a certain voltage. This should indicate how fast the ionic transport of the lithium ions within the cell is occurring.

C-Rate Cycling and Nomenclature

The rate at which a battery is discharged or charged has a large effect on the total capacity of the battery. The higher the rate that is used to discharge a cell, the larger the polarization losses within the cell become. This can significantly change the resulting capacity for the battery, up to orders of magnitude. Conversely, the slower the cell is discharged, the higher the capacity will be. This can pose difficulty when comparing printed cells to those of literature or industry, due to the fact that baseline capacity will be dependent on rate of discharge. A common means for discussion of discharge rates used for battery research is the notion of C rate. This is defined such that:

$$I = M * C_n \tag{8}$$

where I is the current (A), C is the numerical value of rated capacity of the battery (Ah), n is the number of hours for which the rated capacity is declared, and M is a multiple or fraction of C. In practice, a 1C rate is the current at which a battery will be discharged in one hour. For example, the 0.1C or C/10 discharge rate for a battery rated at 5 Ah is 0.5A. Or a 250 mAh battery which is discharged at 50 mA, is therefore being discharged at the 0.2C or C/5 rate. Typically the rating will be written without the subscript after the C, which makes the definition undefined as per the recommended nomenclature. Unfortunately, this is almost always the case. The correct term for the 5 Ah rated battery at the 5 hour rate and discharging at the C/10 rate should be $0.1C_5$ or $C_5/10$, which corresponds to a 0.5 A rate or 500 mA. There are also some who will use the E rate, which is the same as C rate, but with power instead of capacity. Most tests are done to determine the overall capacity of a cell at very slow rates, C/10 or slower. This is obviously due to the fact that the slow rates of discharge will result in a higher capacity for the cell, since the kinetic limitations in the cell will be minimized at these slow rates, and give a better measure of the maximum capacity for the cell. This is advantageous for discussions of cell design, as capacity is the main goal for many projects.

Electrochemical Impedance Spectroscopy and Diffusion

Electrochemical Impedance Spectroscopy (EIS) relies on the sinusoidal perturbation of potential while monitoring the phase shift between the perturbation and the response by the sample. This technique is well established and has been employed for looking at the kinetic and transport behavior within a variety of samples including

batteries (8, 28, 107-109). This technique was largely developed by Sluyters (110, 111), with many other contributors who followed to add to the knowledge base about the technique, of which many books have been published (108, 112-114). The primary information that EIS provides is an indication of the interfacial impedance of each of the sample's interfaces as well as a method for evaluation of diffusion through those interfaces. This method is very sensitive so care must be taken to ensure that there is proper control over electrodes and connections to ensure that the system only measures sample impedance. Shielding (either cable based or Faraday cage) is necessary during EIS measurements to minimize the effects of interference from outside electromagnetic signals.

The EIS technique is based on simple circuit theory. The application of Ohm's law is limited to use only with ideal resistors.

$$V = IR \tag{9}$$

where V is voltage in volts, I is current in amperes, and R is resistance in Ω. One important definition of an ideal resistor is that AC current and voltage signals that pass through it are in phase with each other. This is rarely the case for real systems. The technique, therefore, uses the concept of impedance, by applying a sinusoidal voltage and measuring the phase shift and amplitude of the resulting current sinusoid. The sinusoidal perturbation induced in potential is usually very small to ensure that the measurement occurs within a pseudo-linear portion of the response. The measured current to this

induced perturbation will have a phase shift ϕ with respect to the input sinusoidal wave. The measured impedance (Z) from the technique is described by:

$$Z = \frac{E_t}{I_t} = \frac{E_o \sin(\omega t)}{I_o \sin(\omega t + \phi)} = Z_0 \frac{\sin(\omega t)}{\sin(\omega t + \phi)} \quad (10)$$

where ω is the radial frequency of the perturbation and ϕ is the phase shift. This expression is analogous to Ohm's law but expressed for impedance. The impedance is more often expressed as a complex number:

$$Z(\omega) = \frac{E}{I} = Z_o \exp(j\phi) = Z_o(cos\phi + jsin\phi) \quad (11)$$

Presenting the impedance as real and imaginary components allows for plotting impedance on a Nyquist plot, which is the typical data presentation method for EIS. This plots the real portion of the impedance vs. the imaginary portion of the impedance. The shortcoming of the Nyquist plot is that each data point represents a different frequency, so determination of the frequency can be difficult. This is the necessity for the other data presentation plot, which is known as the Bode plot. Bode plots consist of two figures which plot the log of the total impedance vs. frequency and phase shift vs. frequency. Between the two data representation plots, all of the measured data from an EIS experiment can be expressed.

The data interpretation of an EIS experiment can be difficult because it involves modeling of the electrochemical system with an equivalent electric circuit. These are a

combination of resistors, capacitors, and inductors in both serial and parallel configurations. There is a physical meaning to the electrical elements represented in the interpretation of EIS data and care should be taken to consider all elements within an electrochemical system. Many useful parameters and constants can be extracted using the EIS technique when proper care is taken during the evaluation and simulation of the electrical circuit model.

EIS is a very useful tool to support other methods, but is not often used as a standalone technique, which is why it was coupled to the polarization curve analysis as well as cyclic voltammogram analysis. This is partially due to the complexity of the data analysis and the trend for many constants or impedances to be lumped together into the analysis techniques. The technique can, however, be very beneficial in evaluating transport behavior through layers within a battery. This is typically done through use of a Warburg element in the analysis of the data.

Warburg elements are used in situations where transport is primarily diffusion controlled. At high perturbation frequencies the Warburg impedance is small since the chemical species have a very short distance to diffuse and at low frequencies the impedance becomes large. For the case of semi-infinite conditions (similar to that of chronoamperometry) the equation expressing the Warburg element is:

$$Z_w = \frac{V_m}{\sqrt{2}nFAD_o^{1/2}}\frac{dE}{dx}(1-j)\omega^{1/2} \tag{12}$$

where V_m is the molar volume of the electrode structure $\frac{dE}{dx}$, is the slope of the columetric titration curve vs. the mobile ion concentration. This simplifies to:

$$Z_w = \sigma(1 - j)\omega^{-1/2} \quad (13)$$

where σ is the Warburg constant. Once the Warburg constant has been determined, then these two equations may be used to extract the value for the diffusion coefficient of the species which is being transported within the battery, in this case lithium. This is done when the frequency of the perturbation is large compared to the D_o/l^2, where l^2 is the maximum diffusion length for the battery (or the particle size of the material). This ensures that the perturbation is much faster than the actual transport phenomena. The EIS evaluation of the diffusion coefficient for intercalation / deintercalation is very sensitive to the accuracy of the measurements for constants so care must be taken when measuring these values.

Understanding of transport phenomena and properties is essential in linking material changes with battery performance. Through careful preparation of battery materials, prediction of battery performance is based on material choices and their empirical transport characteristics.

Evaluation of Slurry Rheological Properties for Printable Electrodes

The formulation of electrode slurry for a lithium iron phosphate cathode is comprised of several parts: the active electrochemical constituent (lithium iron phosphate), the binder, the electronically conductive additive, and the solvent. This formulation varies in the amount of each that is used as well as where and how the components are acquired or made, but for the most part these components stay the same. Slight changes in this slurry correspond to huge changes in the properties of the material. A good example of this is the binder used in the slurry to give mechanical strength and flexibility, which is polyvinylidene fluoride or PVDF. This is a thermoplastic fluoropolymer also known Kynar®, Hylar®, or Sygef® and is typically used in applications requiring high purity, strength, chemical resistivity to both acids and bases as well as electrochemical stability within the voltage window for lithium battery operation. The amount of PVDF added into the solvent changes the rheological properties of the solution greatly (see Figure 24). Depending on the chain length of the PVDF, a change in loading of 5 wt% PVDF in solution can increase the viscosity of the solution by well over an order of magnitude as seen in Figure 24. It will be important to understand the rheology of the slurry prior to printing because that same 5 wt% change in

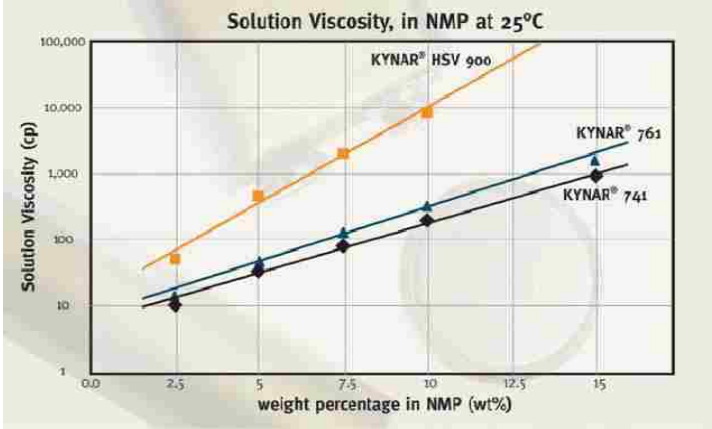

Figure 24 – Demonstration of the logarithmic change in viscosity on higher loading of a solution containing polymer binders. From ref (115)

formulation can mean the difference between a printable solution and something which is too viscous to use.

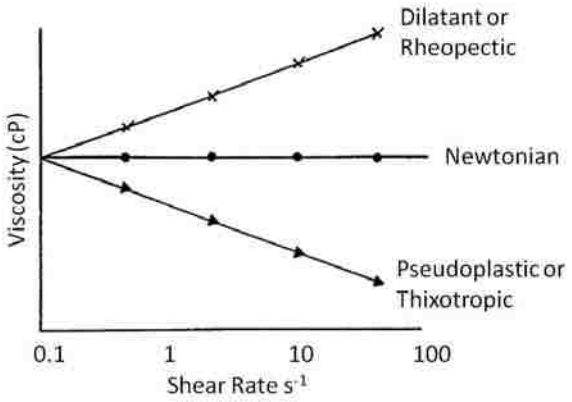

Figure 25 – Types of fluid responses to shear. From ref (116).

The rheological properties of the slurry mixture play a very important part to the ability for an electrode to be printed. The change in viscosity from additional chemical compounds is one way that the viscosity can change. During printing and deposition of the slurry, another form of rheological change can occur which is commonly known as sheer thickening or dilatant fluids. These are fluids which undergo an increase in viscosity with increasing rate of shear. The slope of the shear stress vs. the shear rate, as seen in Figure 25, is the viscosity of the fluid. Since this curve has a zero slope for a Newtonian fluid, there will be no change over the entire range of shear rates. The non-linear curves have changing slopes with respect to changing shear rates. This change in viscosity (increase for a dilatant fluid) will often occur in solutions which contain a suspension of particles in a liquid. The opposite behavior to this is pseudoplastic fluids which exhibit a decrease in viscosity with an increase in shear rate. The last type of fluid which exhibits a change to their rheological properties

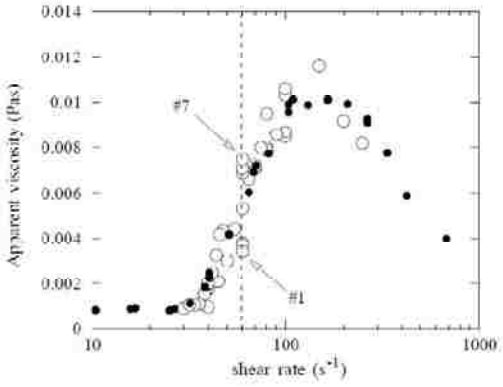

Figure 26 – Example of sheer thickening point in solution. Many examples of these types of dilatant fluids can be found.

with the application of a shear is Bingham plastics, which behave similar to Newtonian fluids with the except that at zero shear rate they have a non-zero shear stress. An example of one of these phenomena can be seen in Figure 26, where a solution of a cetyl-trimethylammonium tosylate in water was examined at varying shear rates on a viscometer (117). There is a point in the curve (indicated by the dotted line) which exhibits severe sheer thickening. The solution undergoes an order of magnitude increase in the apparent viscosity due to the increase in shear rate. This behavior is very common, especially in slurry like solutions. This is exactly the behavior which will result in solution that is unable to be printed or cast using the robocasting technique. This is often unavoidable, especially in systems where there is a suspension of particles (whether they are nano-scale or not) or material flakes. This dilatant behavior of this surfactant in water is analogous to printing a slurry solution for an electrode. As the slurry gets compressed during extrusion from the tip of a syringe, the sheer stress on that solution could exhibit shear thickening (or shear thinning, depending on the solution) and have a major change in the flow properties of the slurry out of the tip. This will have ramifications in how the electrode is cast, the thickness and uniformity of the cast, the ability for solvent to evaporate off after the cast, and the overall performance of the battery made from this electrode.

By understanding the rheological properties of the slurry to be printed, the slurry can be refined in order to maximize the quality (uniformity) of the resulting print. This effort aims to intelligently design electrode and separator slurries based on the behavior of the material with respect to the stress involved with printing that material. The rheological behavior of the slurry can potentially also exclude some slurry formulations

from being compatible with this fabrication technique use in batteries. This is the case when the material exhibits very high viscosities or very an extreme dilatant response to the stress induced by the robocast extrusion. This case has the potential to appear for printed separators as design of these slurries requires the solution to contain a very high loading of solid particulates for electrochemical discharge considerations. The rheological properties of this material may exclude it from being compatible with the extrusion technique. Care must be taken when developing slurry for printing of battery materials. While addition of additives or surfactants may potentially help the rheological properties of the slurry, they may also cause unwanted side reactions within the electrochemical window for the battery.

Traditional Formulations of Battery Materials and Possibilities for Printing

Electrode Slurry Formulation and Characterization

The development of printable $LiFePO_4$ cathode slurry compatible for use with the robocasting technique will be largely based on traditional formulations. The starting point for this material will be an 85:10:5 ratio of $LiFePO_4$: PVDF binder: conductive carbon. The necessity for the binder is to enhance adhesion of the printed slurry to the substrate used for printing, which is the aluminum current collector in this case. The carbon is added due to the non-conductive nature of the $LiFePO_4$. Without the addition of the conductive carbon, there would be little electrical connectivity between the redox point for the lithium within the cathode and the electrical circuit.

This slurry, based on the common deposition methods, should be relatively compatible with the robocasting technique. There are a few considerations that should be made when switching this type of material from traditional doctor blade techniques to robocasting. The viscosity of the materials must be high enough that it does not deposit prematurely or spread from the print tip after deposition. This must be balanced with the fact that in order to make customizable geometries using the control software, the robocast tip must make many passes in order to build up two dimensional widths for the print. As multiple passes are made, traces of slurry are laid down next to each other, causing a scallop effect on the surface of the resulting film. This can be seen in Figure 27, from both the side and front view. The relaxation of this scallop effect on the surface of the cathode can occur while the cathode is still being printed provided the viscosity is low enough to allow for some fluid flow after deposition of the material. This approach will result in the deposition of uniform electrodes before drying in an oven. Maximizing the planarity of the surface of the electrode is important as it can have an effect on the performance of the overall cell especially when coupled with a printed separator.

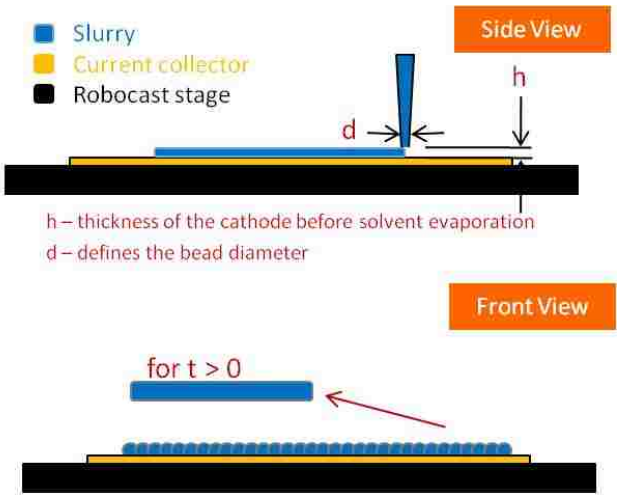

Figure 27 – Considerations for robocast deposition using the extrusion technique. Also shown (bottom) is the progression of the print and how the top surface of the printed film is formed.

The printing of a separator directly onto a printed cathode is a relatively unknown subject but several hypotheses can be made based on this type of deposition technique. Since the separator material is being directly deposited onto the surface of the cathode, the act of printing the separator will ensure there is intimate contact at the interface between the two layers. Since the separator is not physically placed on top of the cathode during cell assembly, there is no chance for gaps to occur between the two layers. This could potentially have implications (both positive and negative) for the performance of the battery. The schematic shown in Figure 27 depicts the interface between a printable separator and a printable cathode. If the surface of the cathode is completely flat, then the separator print will lay flat atop the cathode layer. If the scallops persist from the print of the cathode, then there could be settling of the separator print into the low lying spaces of the scalloped cathode, resulting in an uneven separator. The exact nature of interface can be affected by the print conditions during each layers deposition, so care must be taken to minimize any changes in print conditions from cathode to cathode in order to ensure that the performance of the batteries made using this technique remains consistent.

Formulation of Research Concept for Printable Separator

The idea of a printable separator for batteries is not necessarily new, but is something that has not been fully understood and no commercially viable method has yet been produced. The principle of this work is to base the printable separator on currently available commercial batteries. The most widely used separator in batteries is Celgard

(http://www.celgard.com). These membranes are typically a three layer polymer separator comprised of polypropylene (PP), then polyethylene (PE), then polypropylene. The PP layers are responsible for governing the transport across the membrane. This is the layer that typically contains pores which are filled with electrolyte and allows for the ionic conductivity in the membrane itself. The PE layer is typically used as a defense against thermal runaway of the battery, as mentioned earlier in the section titled "Lithium Battery Development". The PE has a lower melting point than the PP and will melt if the battery temperature ramps up to unsafe levels. The melting of this layer completely stops all transport across the membrane.

These polymeric materials are the most common in lithium battery separators. This is due to several things. They are electrochemically stable in the window used for operation of lithium batteries. This ensures that there will be no parasitic side reactions between the separator and the electrolyte or the lithium to cause either a drop in battery capacity or an unsafe reaction. The polypropylene and polyethylene also readily wet the electrolytes used for lithium batteries. A high degree of wetability of the separator by the electrolyte assures that there will be a continuous liquid phase for the diffusion of lithium to occur within the cell. This is necessary to ensure the maximum possible electrochemical performance from the cell.

The formulation of a printable separator seems to be achievable through emulation of commercial designs. The formation of polymer solutions, while not trivial, is something that has been studied before in the plastic industry (83, 118). The use of these polymers in commercial plastics industry has ensured the availability of

information regarding their safe handling, appropriate manufacturing specifications, and their transport properties.

The traditional materials are the starting point for investigation into a fully printable separator. The materials used for commercial separators are primarily made up of polymers, which are very compatible with the robocasting technique. The polypropylene and polyethylene polymers are the most widely used for commercial separators and can, with proper design, be made into a printable slurry using the rheological properties and the results of various prints. In this way, we aim to use this novel technique with traditional chemistries in order to develop a new type of separator. This will allow for this technique to take from the already established body of knowledge for the separator material properties and performance.

Considerations for Electrolyte use in Robocast Battery

During operation of the battery, the ionic transfer is facilitated by the battery electrolyte. The solid or liquid electrolyte must be printed into the system before the encapsulation of the battery can be completed. There is quite a bit of literature on the formulation of lithium battery solvents (31, 119-124). Most are based on carbonate solvents with lithium salt and other additives. Due to the wide research on these electrolyte solutions, engineers can tailor an electrolyte for their application including any additives needed (125, 126). A small sample of common solvent and additives can be seen in Table 2.

Liquid electrolytes for lithium batteries have two main disadvantages. They are typically hazardous and flammable, which is compounded by the concern for safety when lithium is present. The second disadvantage is that in order to print a complete battery, the electrolyte must be solid in order to be able to print the anode over it. The ability to print one layer on top of another during the casting of a battery would be interrupted by a liquid layer and would make for a difficult engineering challenge.

Table 2 – Common battery solvents and additives

Chemical	Notes
Dimethoxyethane (DME)	Main solvent for primary lithium batteries.
Propylene carbonate (PC)	Exfoliates carbon in cathode.
Ethylmethyl carbonate (EMC)	Added to reduce the viscosity of the electrolyte.
Vinylene carbonate (VC)	Used with carbon anodes at 1% by weight to suppress SEI layer.
Biphenol	Used for overcharging applications.
Hexafluorophosphate (PF6)	Primary salt for secondary lithium batteries, typically at 1 - 1.2M. Has problems above 65 C.
Trifluorosulfonoimide (TFSI)	Used as salt for primary batteries or at higher temperatures in secondary.
Bix(oxalato)borate (LiBOB)	Used with TFSI for high temperature stability.
Tetrafluoroborate (BF4)	Very high temperature applications.
N-methylpyrrolidone (NMP)	Primary solvent to form electrode slurry.
Ethylene Carbonate (EC)	Common solvent for secondary batteries.

Solid electrolytes have received great attention lately due to their inherent safety compared to liquid electrolytes (77, 83, 118, 121, 123, 126-129). These solid electrolytes are typically linear chain polymers complexed with lithium salts. This idea was first discussed as early as the 1960's (83, 130). Typical polymers are polyethylene

oxide (PEO), propylene oxide, polyethers, and polyvinylidene fluoride. The greatest challenge with these solid electrolytes is that they possess very low ionic conductivity (10^{-6} to 10^{-8} S/cm). In order to be a commercially viable separator, a conductivity of $>10^{-3}$ S/cm should be attained. This has been remedied by adding more salt moieties on the polymer chain backbone or by "swelling" the polymer electrolyte. The latter technique is known as gel electrolytes.

The advantage of polymer electrolyte batteries is that the electrolyte typically also serves as a separator. This is ideal for a printed battery, where one layer can take the place of both the separator and the electrolyte and the problem of how to print on a liquid substrate would be alleviated.

The primary focus of this work will be using traditional liquid electrolytes for lithium batteries. This is to ensure that any loss in transport within the cell is only due to the separator or printed electrode. Part of the work of this thesis is to isolate these changes and monitor the affect they have on the capacity of the cell. If the electrolyte were changed at the same time as the deposition method of the electrodes/separator, then determination of the dominating factor in the change of capacity would become difficult.

Evaluation of Slurry Printing and Battery Characterization with Profilometry

Knowing the surface morphology and heights of printed layers allows for understanding of the size scale needed for processes to occur within the battery. The technique used for the primary investigations into thicknesses of printed materials with the robocast technique is profilometry. The Detak 150 surface profilometer was used for

most measurements of surface topography or print heights for any materials printed, as seen in Figure 28. The equipment uses a stylus with a pointed tip which touches the surface of the sample and is scanned linearly across the sample. Variations in height of the sample cause the amount of force exerted and the deflection of the stylus to change. This is measured and translated into the movement of the stylus tip and the software outputs a line scan of the surface of the sample being investigated. The profilometer is capable of scanning in only one direction, so care must be taken to ensure that the sample is set up to facilitate the investigation of areas of interest in the sample.

The capability and resolution of the technique vary greatly depending on the model and manufacturer of the machine. For this investigation the profilometer has a vertical maximum travel (z height) of 1 mm. The vertical resolution is 1 Å with a maximum line scan length of 2000 μm. This technique enables the assessment of the surface profile for robocast materials. This assessment is often used for understanding how each layer contributes to the overall thickness of a battery stack.

Figure 28 – Dektak 150 profilometry system.

CHAPTER 4: EVALUATION AND PERFORMANCE OF ROBOCAST CATHODES FOR LITHIUM BATTERIES

General Slurry Considerations and Comments

The primary formulation for the slurry used to print cathodes is very simple and is considered to be the basic formulation for a $LiFePO_4$ cell cathode. This slurry formulation consists of a PVDF binder, carbon powder for increasing the conductivity, and the active $LiFePO_4$. The ratios used for most cathodes that we printed for deposition using the robocasting technique are approximately 85/10/5 w/w/w of $LiFePO_4$/Carbon/Binder. The reason these are needed is that the iron phosphate is naturally an insulator so the carbon is introduced to increase the conductivity of the mixture so that the entirety of the electrode is accessible electrically during charge/discharge. The binder is added to create an adhesive which holds the electrode onto the current collector. Cathode slurries made in this way begin with a starting viscosity of ~ 170 cP and were adjusted for printing by adding more NMP. Many times, the viscosity of the slurry requires no adjusting for robocasting using the extrusion deposition technique.

The initial tests done to determine the viability of this cathode formulation for use with the robocasting technique were done using pneumatic atomization. This was thought to be best method for creation of a uniform film of the cathode material. An electrode deposited using the pneumatic technique can be seen in Figure 29. The electrodes that were made using the pneumatic side of the robocasting machine yielded

very non-uniform films. Moreover, there was no possibility for deposition of cathodes that didn't contain extensive amounts of cracks. The cracks typically led to delamination of the cathode from the substrate. By atomizing the slurry in an aerosol, the drying process was initiated at the moment of atomization. This resulted in a very fast drying stream of slurry being printed. This result was indicated by the fact that the print was being deposited onto the substrate in a very dry state. The fact that the slurry was much too dry when deposited onto the substrate led to cathodes which were not ideal for use in a full battery. The deposition method was re-examined after the resulting cathodes were tested using the pneumatic technique. After testing with an extrusion method, cathodes were repeatedly printed with no issue of cracking or drying. The resulting films were continuous and could be printed in a much more controlled fashion than possible with the atomization technique. The solvent level in the starting slurry is maintained in the resulting print using the extrusion method. The absence of the rapid drying during the extrusion technique made it the primary choice for printing during these experiments and was used all subsequent samples.

Figure 29 – Example of electrode made using pneumatic atomization on the robocasting machine. The substrate used for deposition is carbon coated aluminum.

Evaluation of Robocast Cathodes in Full Cell Batteries

All cathodes were printed using a casting tip which has an inner diameter of 225 μm. The standoff typically used for robocasting is about ½ the inner diameter of the print tip away from the substrate. Since the substrate for the print (carbon coated aluminum) has some bow to the surface, despite all precautions, a standoff of 150 μm was found to produce consistent film heights for cathode slurries. Cathodes were printed using a custom program for the robocasting machines which consisted of a 10 mm lead-in (sacrificial initial print line to allow for settling of the resulting print), then a square of dimension 30 mm x 30 mm. The overlap (a portion of the overall width of each pass which is written back over during the next pass) used during the print was 0.5 (so the robocaster would move ½ of the printed line-width each pass instead of the whole line width), ensuring that each pass of the deposition tip would overlap the previous pass and that there would be no breaks in the film, unless a clog or air bubble occurred within the

tip. After printing was completed, the cathode films were dried in a vacuum oven at 105 °C to drive off the NMP. During this drying process, the cathode slurries which were correctly made exhibited no cracking and resulted in a uniform film. If there were inconsistencies in the slurry or the printed film was too thick, cracks would form upon drying.

The result of a typical print using this technique can be seen in Figure 30. The three examples present show the normal output for a robocast cathode. The top cathode shown, if inspected carefully shows two small spots where the cathode slurry did not deposit. This was a result of an air bubble within the deposition tip itself formed during the printing process. These were minimized by careful de-aeration of the syringe used for printing during the loading of the slurry into the syringe. Despite this careful preparation of the slurry, this was an observable phenomenon that occurred and did occasionally interfere with the successful printing of the cathodes. Since these printed cathodes will eventually be used in a coin cell format, the sections that are printed continuously can still be used for evaluation of battery performance and the non-continuous sections may

Figure 30 – Robocast cathodes as prepared.

also be discarded. Profilometry scans for many of the prepared cathodes show an average electrode height of 60 μm.

The dried cathodes are then baked overnight at 120 °C in a vacuum oven in a dry room to ensure that any residual water from being printed in the open atmosphere was driven off. Without this step, the batteries created from the robocast process had too many contaminants within them to cycle at their full capacity. In addition, the presence of any water within the sample could lead to the undesirable and unsafe reaction of the lithium with water.

The 9 cm2 printed cathode yields enough area to punch out two 2032 button cell cathodes. The two cathodes were punched out and placed within the coin cell canister. Celgard 2032 was placed on top of the cathodes for evaluation of the cathode with a commercial separator. The Celgard was capped by a circular punch of lithium, the electrolyte was added and the whole cell was capped and sealed. Evaluation of the robocast cathodes was done using the standard electrolyte of 1:1:3 PC:EC:DMC with 1.2 M $LiPF_6$ salt. The resulting coin cell was the same size and shape as alkaline cells sold for hearing aid batteries as seen in Figure 31. The primary choice for use of the coin cell is to place uniform pressure on the cathode/separator/anode stack due to the spring washer within the cell. This ensured that changes seen from cell to cell were based on the materials and print of the electrodes and not the contact of the layers within the cell. Standardization of the impedance based on physical contact was intended to be minimized within the coin cells.

The cells were cycled using the Maccor battery test system (model 4304) to evaluate the capacity, discharge rate capability, and lifetime performance. The discharge curves of a robocast cathode in a 2032 coin cell can be seen in Figure 32. This cell was cycled at 0.4 mA discharge current, which was than the C/10 rate for determination of the overall capacity. The cells were cycled from 3.6 volts to 2.5 volts. The discharge curves for the printed cathodes exhibit capacities ranging from 75 – 115 mAh/g. This was slightly lower than the theoretical capacity for the $LiFePO_4$ cathode material, but was considered to be a reasonably good amount of practical capacity for this material. The rate used in Figure 32 corresponded to a 2/3C rate for this cell, since the cell was overall a 0.6 mAh cell with 19.6 mg of active material (30 mAh/g). Most cathodes printed using the robocasting technique showed high repeatability for performance very similar to these discharge curves. Note the plateau region during discharge due to the olivine structure of the cathode active material. This is ideal for applications which have a small operational range on the voltage. Operation of these batteries in the state of high charge (cycling only down to approximately ½ of full capacity) allowed for very consistent operational voltages.

Figure 31 – Complete 2032 coin cell assembly containing robocast cathode.

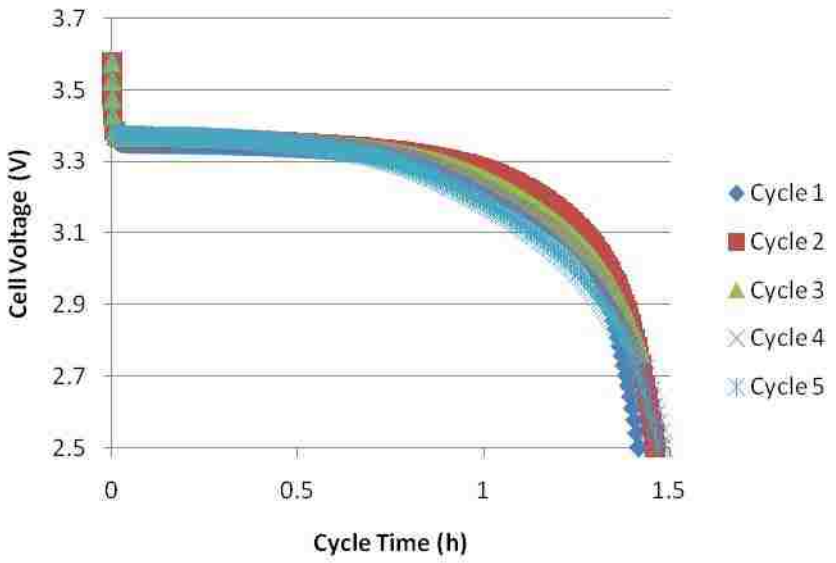

Figure 32 – Cycling performance of robocast cathodes in a 2032 button cell at 0.4 mA discharge rates. Cycling was performed over a 48 hour period.

The robocast cathodes were evaluated using charge/discharge cycling to evaluate the rate capability for these cells. The goal of these tests was to understand how well the batteries could operate under varying external load conditions. C rate performance for the robocast cathodes can be seen in Figure 33. There was a quick drop in capacity and usable power generated by these batteries as soon as the current increased to over ~ 2C. At rates higher than 2C the battery immediately dropped in voltage and produced very little power before hitting the cutoff voltage set for these cathodes.

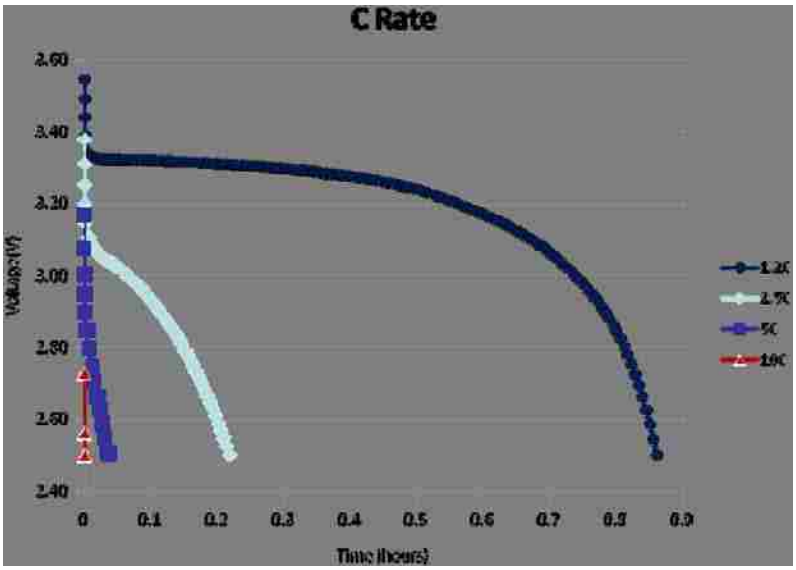

Figure 33 – Rate capability of robocast cathode batteries.

The robocast cathodes were also evaluated for lifetime performance. This was done by cycling on the Maccor test system for long time periods at moderate current levels. A 2032 coin cell was setup for test at 0.9C discharge rates to cycle. The results for lifetime cycling can be seen in Figure 34. The cathode materials printed with the robocast technique exhibited 89% capacity retention after 60 cycles or 2 weeks of continuous cycling. This high level of capacity retention allowed these batteries to be used in applications which require longevity and high cycle life. The fade in capacity could be dependent on the discharge rate the cell was subjected to, so for lower discharge rates, the capacity retention may even increase compared to the data shown in Figure 34. This capacity retention makes these cells viable for applications which require multiple cycles at low currents.

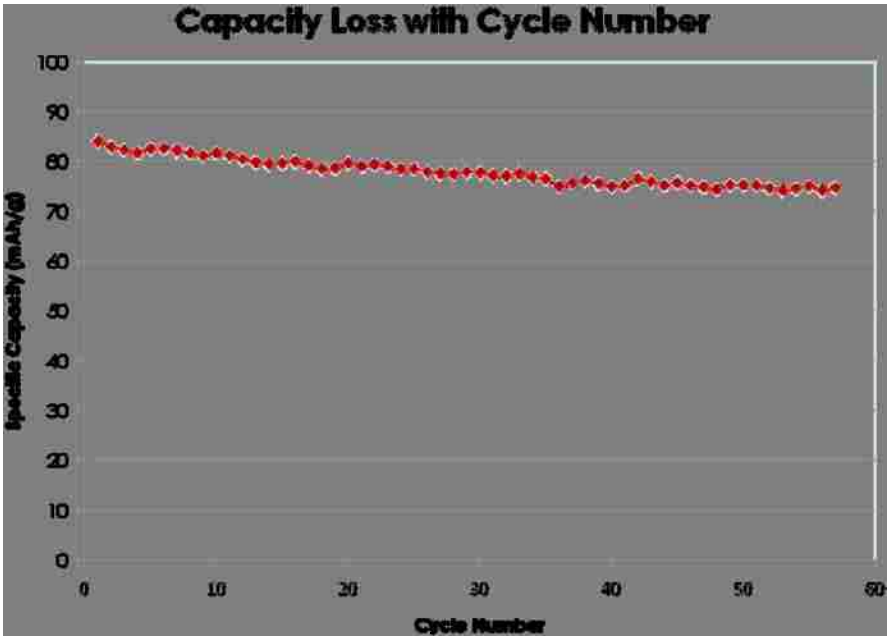

Figure 34 – Lifetime cycling tests of printed LiFePO4 cathodes in a 2032 coin cell configuration. Cycling was carried out at 0.9C rate, indicating losses could be minimized even more by cycling at a lower rate.

The robocast technique was capable of creating viable cathodes for lithium battery cells (131). The consistent lifetime capacity and stable operating voltage show promise for a number of applications.

EIS experiments were conducted on the coin cells containing the printed LiFePO4 cathodes with the Celgard separator. These scans were conducted at various voltages near the discharge potential for the cell, as seen in Figure 35. The Nyquist plot shows that the semicircular portion of the impedance was relatively stable with respect to the potential within the cell. The primary time constant for the cell did not vary with changing potential. The primary change in the impedance spectra occurs at low frequencies.

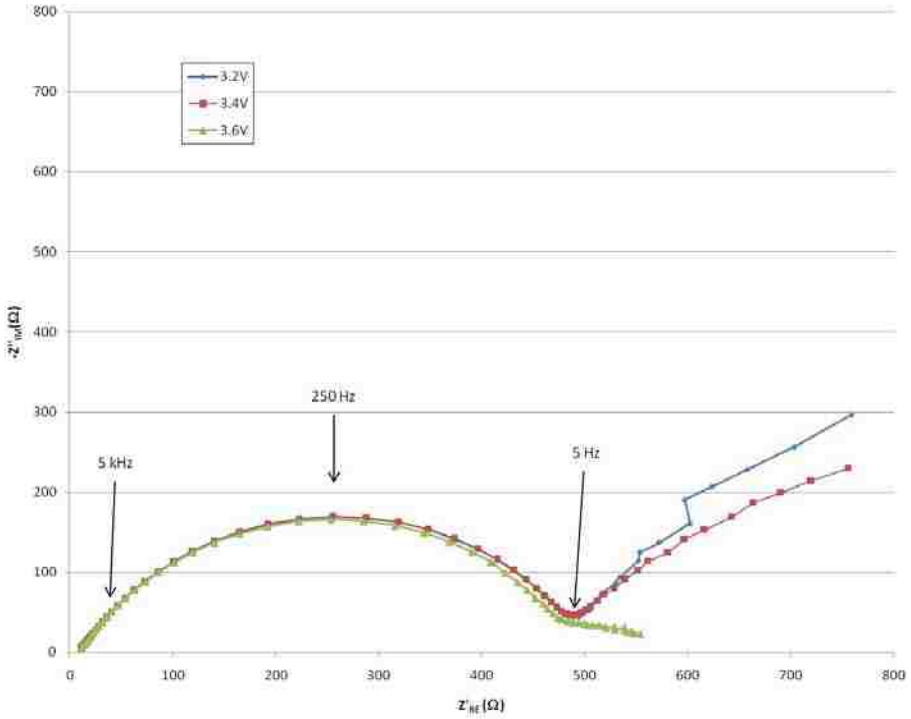

Figure 35 – Electrochemical impedance spectroscopy of a battery with robocast LiFePO4 and Celgard separator.

The electrochemical impedance shown on a Bode plot can be seen in Figure 36. The overall impedance of the cell was 540Ω, which remained unchanged based on the voltage of the cell at low frequencies. The phase shift also exhibited some deviation at lower frequencies based upon the voltage. Both the Bode plot and the Nyquist plot showed that there was a similar time constant involved with the cell and the only thing that changed with voltage of the cell is the low frequency response. Increasing the voltage increased the observed phase shift and slope of the tail seen in Figure 35. As the potential increases from 3.2 to 3.6 volts on the cell, the polarization of the cell actually reverses from the open circuit potential and attempts to drive the reactions backwards within the cell. At high polarization (3.6V) this is seen as a negative slope at low frequencies.

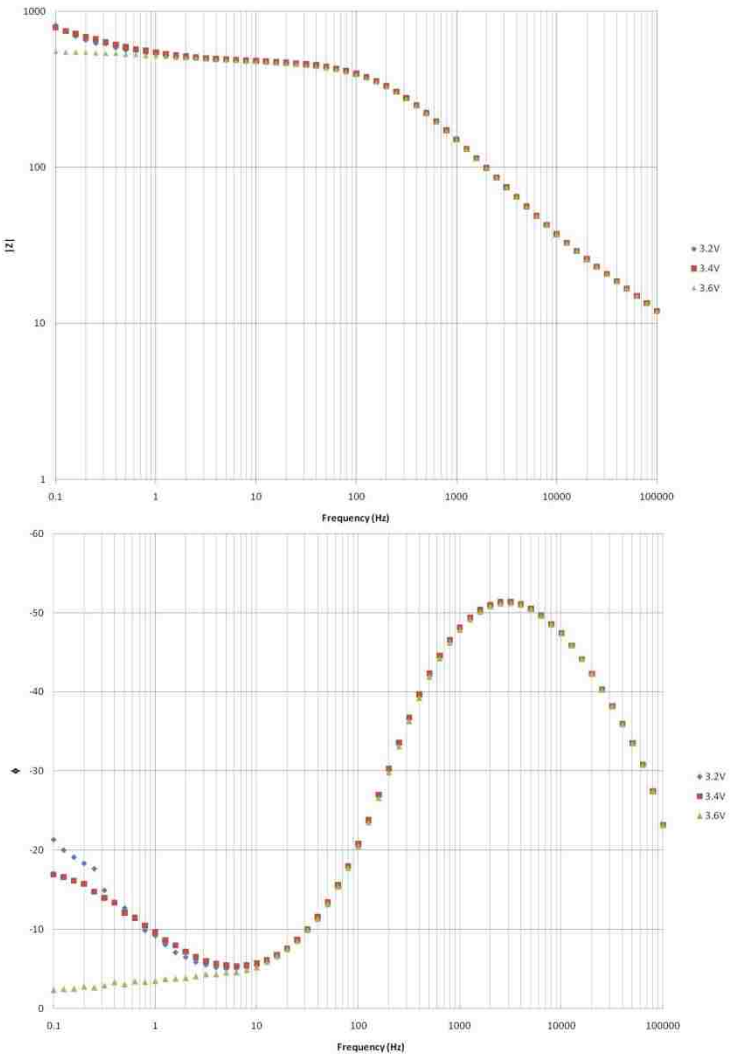

Figure 36 – Bode plot representation of the electrochemical impedance spectroscopy for a printed $LiFePO_4$ cathode with a Celgard separator at various voltages.

Evaluation of Micro-Scale Features within Robocast Cathodes

Many of the cathodes prepared by the robocasting technique were evaluated using scanning electron microscopy to evaluate the structure of the materials. The microscopy was carried out on a Hitachi S-5200 Nano SEM equipped with a Princeton Gamma Tech

(PGT) EDS mapping system. The initial reason for the use of this system was that it had excellent resolution for a scanning electron microscopy (SEM). This unit has nearly the resolution of many commercial transmission electron microscopes (TEM) and has the added benefit of containing an electron dispersive spectroscopy (EDS) unit equipped. The resolution of the system @ 1kV is 1.7 nm and at 30 kV is 0.5 nm. The zoom capability on the microscopy is 100x to 2,000,000x. This allows for inspection of any size scale needed for the cathode characterization. The only obvious drawback to evaluation of lithium cathodes is that the EDS technique is unable to detect the presence of lithium, so any spectra will be void of a lithium signal. This is typically due to the absorption of the signal by the lenses on the EDS system itself for signals of elements smaller than C on the periodic table (atomic number <6).

Micrographs of several robocast cathodes as prepared at several different zoom levels can be seen in Figure 37. The robocast cathodes for the most part exhibited a very heterogeneous distribution of particle sizes and shapes. A calculation for each of the zooms used in Figure 37 showed that the average particle sizes were 2.13 and 4.63 μm for pictures a/b and c/d respectively. The severely heterogeneous nature of the material was seen in the fact that the standard deviations for the particle sizes on these micrographs are 1.25 and 4.25 μm for pictures a/b and c/d, which was essentially the same as the average particle size. This information can only tell us that there are no discernable trends for particle size or shape in this material and that it truly does exhibit a random orientation and size.

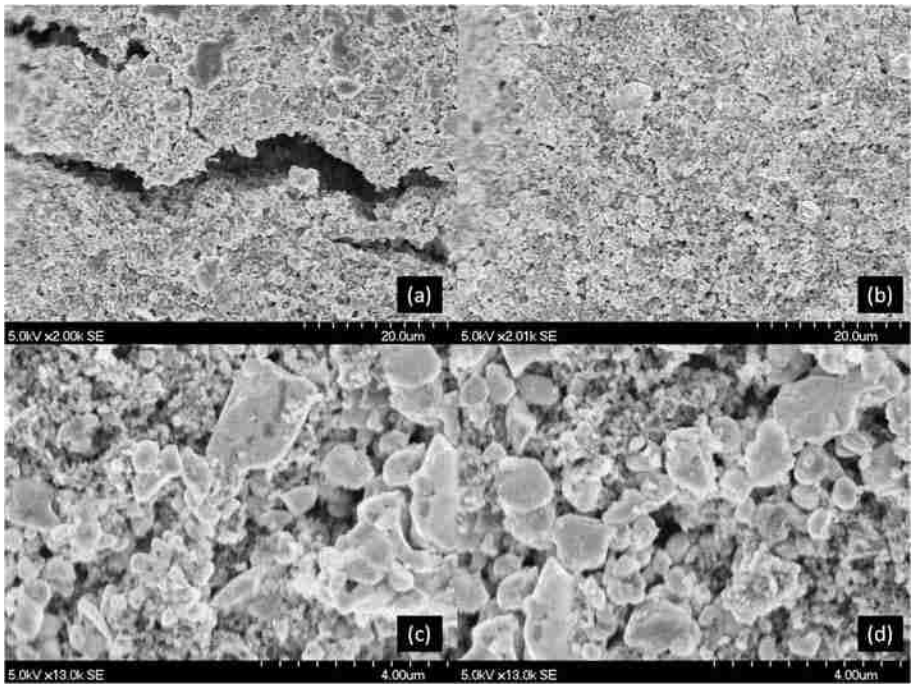

Figure 37 – SEM micrographs of robocast cathode materials. Most of the cathodes are uniform and continuous (b) but some cracks develop during drying and pre-examination preparation for SEM (a). Take note that the slurry does not produce a homogenous mixture of active material particles (c,d), the distribution of particle size is very high.

Analysis of the robocast cathodes was also carried out via EDS techniques. This was done simultaneously to the SEM micrographs, so the EDS spectra were indicative of the actual composition in the regions captured on the SEM images. The EDS spectra can be seen in Figure 38. The EDS spectra showed the primary contribution of the cathode was carbon and oxygen, which came from the phosphate group for the oxygen and the carbon added to the slurry formulation. The other contributing elements were the iron and the phosphorus from the active material in the cathode. This was confirmation that the cathode was composed of the elements that we expected. This technique can identify impurities in relatively high levels, which did not seem to be present in these micrographs. This however, does not rule out impurities that may be present near the detection limit of the technique (~ 1 wt%) (132).

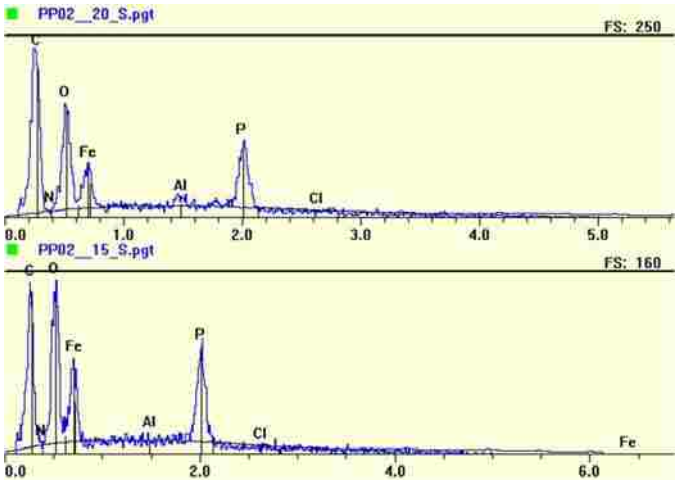

Figure 38 – EDS spectra for several robocast cathodes. The spectra are exactly what are expected for $LiFePO_4$ cathodes, as they contain mostly carbon, iron, phosphorus, and oxygen. Please note that the EDS technique is unable to detect the presence of lithium.

Pulsed Power Testing of Robocast Cathodes

The use of cathodes prepared using the robocasting technique was demonstrated for an application in which a power demand was supplied that required the pulsed operation of the battery. The application dictated several design parameters for the cell including battery size, operational lifetime, cell overpotential, and power profile. The profile for these tests can be seen in Figure 39. It was obvious from this profile that the coin cells with robocast cathodes were unable to provide such high currents. The performance of the 2032 cell in rate testing showed that

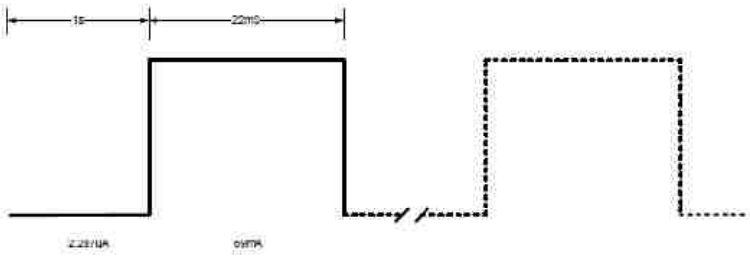

Figure 39 – Profile needed for useable battery performance in application specific design.

even at 5C rates (10 mA current) that the drop in voltage is dramatic enough to not produce useable power out of the cell. The best way to increase this was to increase the size of the active material within the cell. The other design constraint was that the thickness needed to be minimized, and ideally kept less than 400 μm of total thickness including the package. This also excluded coin cells as they had a typical thickness of 3.2 mm. The design of the cells was also specified so that the operational voltages allowed were between the operational 3.4 V of the cell and 2.0 V as the lower limit. The overall cycling lifetime of the cell was also specified to be low, such that 15 minutes of useable cycling would be sufficient to accomplish the goals for the test.

The initial attempt for evaluation of design of a cell which would be viable for this technique was done by robocasting the cathode material in the normal manner. Instead of punching out the cathodes for coin cells, a pouch cell was used to minimize the size of the cell as per the design requirements. In order to keep the battery as thin as specified, ultrathin lithium shim and copper shim was used in the construction of the pouch cell, as seen in Figure 40. The pouch was made with the normal blue heat-sealable coated aluminum. Overall, these cells were ~425 μm in thickness, which was right within the design window for the application. This satisfied the design requirement of thickness and cell size, but performance was necessary to understand the current produced by the cell.

Figure 40 – Pouch cell constructed for evaluation of robocast battery cathodes for pulsed power application.

The first test step for these cells was to print cathodes which had a geometric area of 25 cm^2 and a height of 450 μm. These cathodes were made into batteries using the pouch cell and then cycled several times under normal conditions. Then they were discharged using a pulse profile at varying pulse heights to determine the voltage drop due to the increasing current during the pulse. The results in Figure 41 show how the cell performed during normal operating conditions and resulted in a 34 mAh capacity at 3 mA charge and discharge current. The cell was then charged to full and pulsed discharge was performed. This consisted of pulses varying in magnitude from 40 to 100 mA. During the 40 and 70 mA pulses, the voltage of the battery was able to stay above the compliance voltage of 2 V but during the 100 mA pulse, the voltage dropped well below that limit. In between each pulse cycle the cell was charged to full before the beginning of the next pulse discharge step. This cell fabrication technique and size was appropriate for the target application, making the creation of similar cells to meet any design specifications possible using the robocast technique.

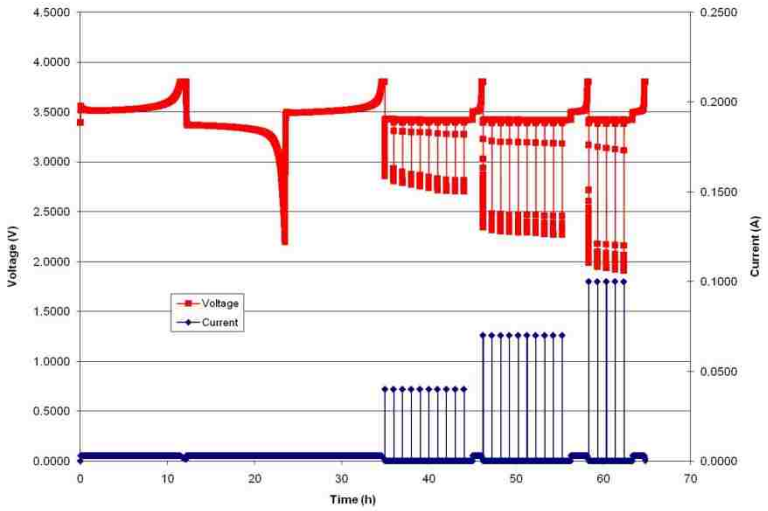

Figure 41 – Initial testing of batteries for use in pulse power applications.

A secondary requirement for pulsed discharge in this application was for a pulse every hour over the course of approximately 10 hours with a resting current of 3.2 μA

and discharge pulses of 80 mA for 36 seconds. This required fabrication of cells large enough to allow for the long times during rest and high enough capacity to still be able to maintain the compliance voltage during the large current draws. Cathodes were printed with geometric areas of 16 cm^2 and fabricated into pouch cells. The pulse profile was followed directly this time so as to test the actual performance of the cells under operating conditions, as seen in Figure 42.

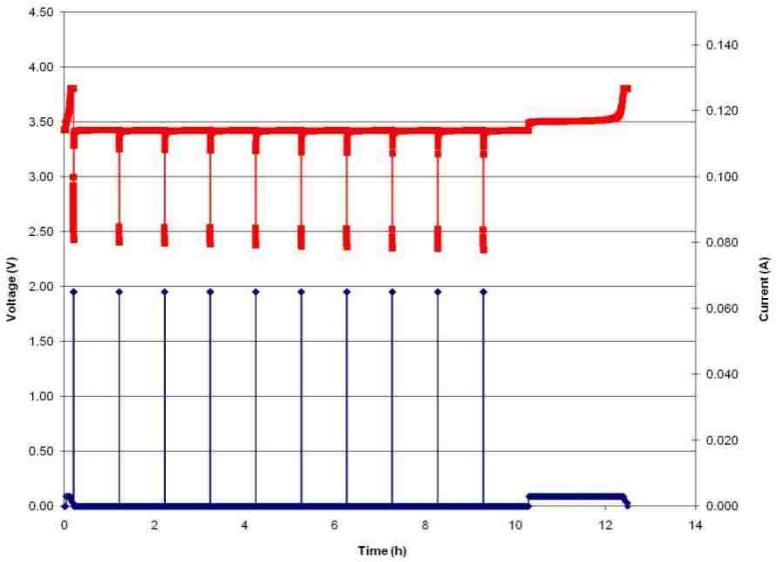

Figure 42 – Pulse discharge profile for specified current profile.

The cell was able to supply the required pulse current while maintaining the compliance voltage due to an iterative process of printing cathodes which were expected to meet the design requirements, testing their capability and then adjusting the area of the printed cathode while keeping the thickness and bead size constant. This allowed for tailoring of a battery to meet exactly the design requirements from the application. This was one of the benefits of the robocasting process for use in development of batteries; the current produced by the printed cell can be uniquely tailored for the application.

CHAPTER 5: EXPLORATION AND DEVELOPMENT OF PRINTED SEPARATORS FOR LITHIUM BATTERY APPLICATIONS

Battery Separator Considerations

Battery separators are a key component within a cell due to the fact that the separator controls the ionic diffusion within the cell. There has been a great research effort into the understanding the role of the separator in battery performance (20, 83, 107, 121, 124, 133-136). This has enabled many advances in battery performance due to better performance of the separator.

Separators for lithium batteries have several key requirements for viability in cells. Separator materials must be electrically insulating to prevent a short between the anode and cathode during cycling and to avoid safety issues when building the cell. Separator chemistry must be stable for use in the battery electrolyte. Side reactions between the separator material and the electrolyte must be minimized for both safety and performance reasons. The thickness of the separator material must be minimized. This is important since the separator controls ionic transport within the cell and a thicker separator will result in a longer diffusional distance and a subsequent higher internal resistance. Minimization of the thickness while still maintaining separation between anode and cathode is an important engineering consideration for cell design. Porosity and permeability of the separator material must be maximized to ensure proper performance from the battery. Ideally the pores will be homogenous and straight through the separator to ensure the fastest possible transport across the film. Unfortunately, the

separator always contains some tortuosity, so minimization of that is preferred. The transport for the separator is typically compared using the MacMullin number, which is the ratio of the electrical resistance of the separator in the presence of the electrolyte vs. an equal volume of electrolyte itself. This number is typically kept under 4-5, as there is significant loss of battery performance if this ratio is above 5. The addition of the electrolyte to the separator material also should have good wetting characteristics. For safety considerations and to allow for flexible cells, the separator must have good mechanical stability. The final consideration for lithium battery separators is cost. Separators typically contribute 20% of the total cost of a battery and increases in the cost of the separator can easily exclude a battery from commercial viability based solely on cost.

Traditional Separator Types and Ideas

There have been many proposed methods for making a battery separator. Generally, these fit into four categories. Each of them has benefits based on the application of the battery, since one type of separator will perform better for certain applications. Again, the development of batteries and printable cells is very application driven and the specific requirements of the cell need to be considered.

The first type of traditional separator is the microporous separator. This is by far the most common separator used in lithium batteries. These separators consist of non-woven fibers or polymers which are mats of material laid down to form a film. These films typically have pores which have diameters >100 Å. These separators are most

commonly extruded into sheets of appropriate width for the application (type of cells being made from the film) and then rolled onto spools, see Figure 43 (137). The spools can then be used in a commercial cell manufacturing process which is a reel to reel manufacturing technique. Many companies manufacture these types of separators including Asahi Kasai, Celgard LLC, Entek Membranes, Mitsui Chemical, Nitto Denko, DSM, Tonen, Ube Industries and the resulting separators go by many trade names including HiPore, Celgard, Teklon, Solupur, Setela, and U-Pore (138, 139). These separators are available in many configurations and chemistries. The most common chemical makeup for this type of separators is polypropylene (PP), polyethylene (PE), polyvinyl chloride (PVC), and polyvinylidene fluoride (PVDF).

Figure 43 – Celgard battery separators as prepared. Image from manufacturer's website, http://www.celgard.com/products/specialty-membranes.asp

The microporous separators are manufactured using either a dry or a wet process. The dry process involves melting the polyolefin resin and extruding it into a film. Once the film is formed it is then stretched to create the pore structure. This is done because a lamellar crystal structure is formed during the extrusion process. This structure allows for a physical stretch step after film formation which stretches the lamella apart to form the pores. Because the pores are formed with this stretch technique, they take the form of a slit or diamond shape within the film (138). These films are also anisotropic due to the form of the pores. Emulation of this process for printing lithium battery separators is ideal, but the application of the post extrusion stretch process is not feasible.

The wet process used to form microporous separators typically involves mixing a hydrocarbon or low molecular weight material with the polyolefin which is then heated and extruded similar to the dry process. The resulting film is then introduced to a high volatility solvent to extract the hydrocarbon. This phase inversion process uses a solvent to enable pore formation rather than using the physical stretch technique of the dry process. The wet technique can be further tailored per application by adding blends for the polyolefin or hydrocarbon.

The second type of traditional separator used for battery fabrication is fibrous separators. These separators are made from fibers laid down into a mat which creates the porosity of the separator. Fibrous separators can be either oriented or random. The pores are defined by the interstitial space between fibers and can be designed to be either random or highly controlled.

The third type of separator is gel electrolyte separators, which contain a porous material similar to the microporous separator which has been swollen with a liquid electrolyte or gel. The liquid electrolyte that is used to swell the pores of the membrane contain some type of gelling agent such as PEO, poly(acrylonitrile) (PAN), PVDF, or poly(methyl methacrylate) (PMMA) (138, 140). The benefit of these separators is that since there is no extra liquid electrolyte they are easy to package, ship, and handle. Additionally, the high loading of binder materials such as PVDF allow for laminating the separator to the other layers within the cell as opposed to just physical contact (138).

The last type of separator for lithium batteries is the polymer or solid electrolyte separator. These separators use no liquid electrolyte and the lithium transport across them occurs along the backbone of the solid material. The most common materials used

for this type of separators are PEO and poly(propylene oxide) (PPO) (11, 41, 94, 129, 141, 142). These separators are one of the most rigorous and expanding areas of lithium battery research as they offer many benefits over liquid electrolytes, particularly safety. The drawback to solid electrolyte separators is that the ionic transport across them is many orders of magnitude lower than in liquid electrolytes. For example, the room temperature conductivity of lithium though PEO which is 10^{-6} to 10^{-8} S/cm whereas most liquid electrolytes have a conductivity > 10^{-3} (83).

Due to the inability for the post processing steps used traditionally to induce pores into a polymer separator, a printed separator must have the pores induced another way. The method was used is the introduction of a porous phase into the printable polymer before robocast deposition. Introduction of the porous material before printing of the separator will allow for a porous film to be deposited without any subsequent materials. This technique has been investigated previously (143, 144). This method is described as an idea for introduction of the pores within an otherwise nonporous separator. Enabling this printed system allows for much more flexibility during application specific design of power sources. The printing of the separator directly onto a cathode could potentially also decrease the impedance of the cell by ensuring the best possible interface between the two components of the battery.

Viability Studies for Separator Materials for Printable Separators

Investigation into Material Properties Based on Sample Loading

The use of traditional separator materials for printable separators was done in order to ensure the viability of the materials during cycling. Three materials systems were investigated to produce solutions capable of being printed and tested to understand if the resulting separators were capable of supporting battery cycling. The materials were polypropylene, PEO, and a chlorinated polyolefin blend of both polypropylene and polyethylene. Since there is no way to induce the physical pore forming stretch operation with both the polypropylene and polyolefin blend, a porous silica aerogel was added to the polymer to create the pore structure.

Aerogels are solids which have extremely high volume fraction porosities up to 99.9% (145). These materials can be made from organic or inorganic precursors and are typically dried using a supercritical drying technique. We used aerogels prepared by a technique where surface groups are added to the gel to induce a springback effect drying, making the drying shrinkage reversible (146, 147). This porous material is what will become the pores where ionic transport of the lithium across the battery separator will occur. The use of this porous material will enable creation of a printed porous film of polyolefin material without the need for the post extrusion stretch which is traditionally employed. The important factors for performance of the cell will be the porosity of the material and the ratio of the polyolefin blend to aerogel. There will be a balance between ability to be printed and ability to create a cycleable battery.

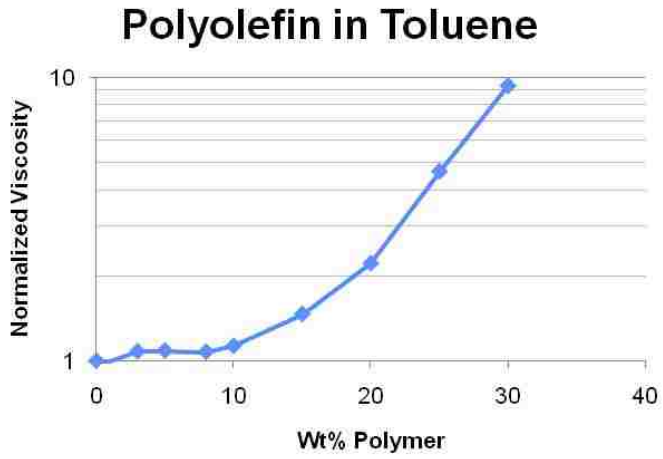

Figure 45 – Rheological response of the polyolefin blend in toluene based on wt% of the polymer.

The materials were dissolved in appropriate solvents at varying ratios to determine the slurry loading which would yield a printable solution using the robocasting technique. After mixing of each sample, they were left overnight on a shaker plate to ensure complete dissolution of the polymer in the solvent. Higher loadings of polymer (>30 wt %) resulted in solutions which were unable to be completely dissolved even after one week of agitation.

Samples were evaluated using a cone and plate rheometer (Bohlin model CS10) at a constant sheer stress of 20 Pa using a cone and plate with an angle of 1 degree on the cone. Each of the samples was normalized to the supporting solvent.

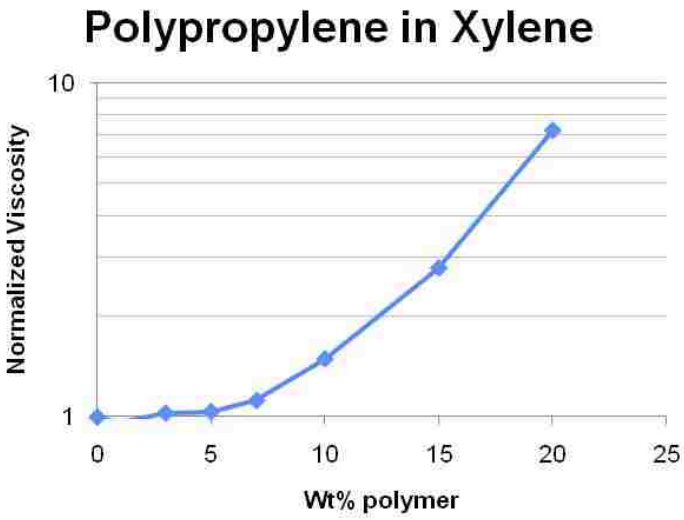

Figure 44 – Rheological response of polypropylene in xylene based on wt% of the polymer

Results can be seen in Figure 44, Figure 45, and Figure 46. For both the polypropylene and the polyolefin blend there is an increase a 10 fold increase in viscosity as compared

to the initial solvent of that respective slurry with a 20% mass addition of polymer. The PEO exhibited an increase in viscosity of five orders of magnitude as compared to the supporting solvent. At polymer wt% greater than 5 %, the solution exhibited gelation and was no longer able to flow. Slurries with viscosities this high are very difficult to work with using the robocasting technique and produce films that are usually non-continuous.

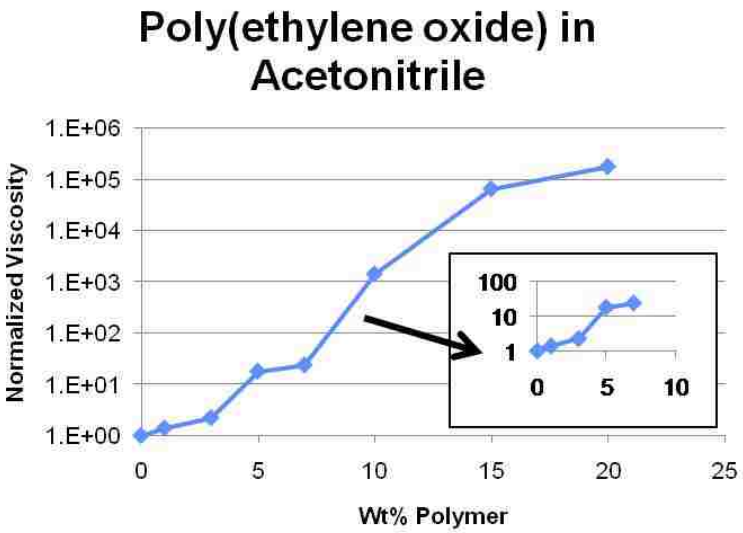

Figure 46 – Rheological response of PEO in acetonitrile based on wt% of the polymer

Robocasting of Characteristic Line Prints

Slurries were the evaluated to determine if there was an optimum loading for deposition using the robocast technique. This was done by printing test coupons on a glass slide. Each solution was loaded into a 3 mL syringe with a 0.250 mm diameter tip and placed on the robocaster for printing. The dispense nozzle was brought into contact with the glass substrate then lifted up 0.150 mm in the z direction for a constant standoff

from the substrate during printing. The print was conducted with a stage speed of 10 mm/s. Results came from scanning multiple passes at the 4 different points along the print. This is to minimize any differences due to variations along the length of the printed line.

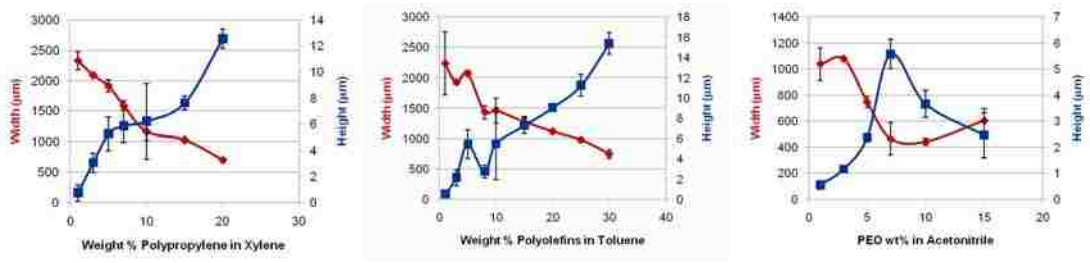

Figure 47 – Line scan results for test prints using three materials for use as a printable separator. Shown are: (left) height and width of polypropylene in Xylene, (middle) height and width of chlorinated polyolefin blend in toluene, and (right) height and width of PEO in acetonitrile.

Figure 47 shows the result of the line scans for the three different printable separator materials. The results for both polyolefin and polypropylene show a decrease in printed line width with increasing weight loading of polymer. This is because the lower loading of polymer spreads easily after the print, so the solution widens upon deposition onto the substrate. This is confirmed by height data, since the widening of the print results in a reduced line height. The PEO shows a slightly different trend, since there is a maximum for height and a minimum for line width. The minima/maxima correspond directly to the point mentioned previously when the viscosity of the material increases by two orders of magnitude. It is at this point that the dilatant nature of the material makes the printing of the material very difficult. The line tests printed at 10 wt% PEO were very difficult to print and had difficulty extruding the material in a uniform fashion unlike the lower loading samples.

The 5 wt% sample of PEO and the highest loading samples for the polypropylene and polyolefin as shown in Figure 47 were used for further examination within battery coin cells.

Evaluation of Viable Separator Materials by Electron Microscopy

The porosity on these materials was investigated using a scanning electron microscope (SEM). The three materials tested were printed using the robocasting technique, and then slices of the resulting print were transferred to a sample holder for use in the microscope. The evaluation was to determine the possibility of pore creation simply through deposition using the robocasting technique. No aerogel (or other similar material) was added to introduce pores into the printed films.

Figure 48 – SEM image of the printed polypropylene film at 2.0 kV.

Figure 49 – SEM image of the printed polyolefin film at 2.0 kV.

The printed polypropylene film and the polyolefin film can be seen in Figure 48 and Figure 49. There is no evidence of porosity within these samples. The samples were very susceptible to charging during evaluation with the SEM, even at low accelerating voltage. This interfered with the acquisition of proper images for these two materials, but the images do definitively show that there is no porosity to these films without addition of materials or other techniques to create pores. The printed PEO film can be seen in Figure

50. These films appear to be very smooth and also do not contain pores. These samples did tend to chip and were brittle compared to those using the polyolefins.

SEM was also performed on the silica aerogel to evaluate the structure of the material. As seen in Figure 51, there is definitely a structure to the material. There is no order to the pores which is acceptable for the separator since the primary concern is the presence of pores to facilitate transport.

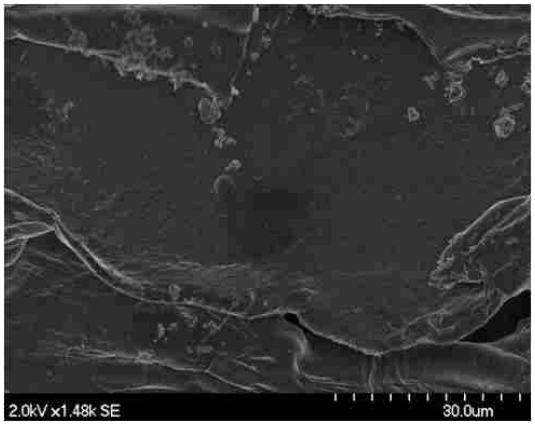

Figure 50 – SEM image of the printed PEO film at 2.0 kV.

Evaluation of Charge/Discharge Behavior for Printable Separator Materials

Cathodes were printed as described in the previous section "Evaluation of Robocast Cathodes in Full Cell Batteries". The different separator material sets were then printed in a similar fashion to the cathode. Due to the higher viscosity of the separator materials, the prints were conducted with a 0.41 mm tip and a 0.2 mm standoff between the dispense tip and the cathode material. This meant that in the area where there was only current collector (varnephite) the standoff was slightly higher (the height of the cathode print or 65 μm). Each of the separator prints was an

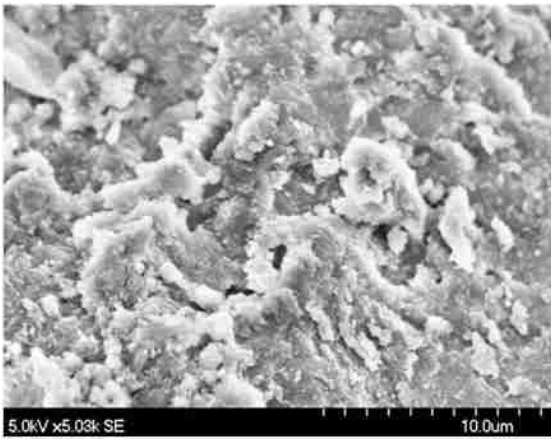

Figure 51 – SEM image of silica aerogel powder at 5.0 kV.

extra 2.5 mm wider per side to make sure that there was no exposed cathode. Any exposed cathode would immediately short when assembled into a full cell since no other separator materials were added to the cell.

The polypropylene separators were printed and 2032 coin cell electrodes were punched into disks with a diameter of 0.625 inches. Both films were baked at 120 °C in a dry room to ensure that there was no residual water in the sample. The lithium disks used were punched out to have a diameter of 0.5 inches in an effort to make sure there was no shorting when these cells were assembled. If the two disks were the same diameter, there is a risk that during sealing of the coin cell they may shift and the edges of the two electrodes could short the cell. The two disks were assembled into a 2032 coin cell with enough standard electrolyte of 1:1:3 PC:EC:DMC with 1.2 M LiPF6 salt to just wet the area of the robocast separator (~ 200 μL for most cells). The resulting robocast polypropylene separator cells were then cycled with a current of 1 mA. The result of the cycling can be seen in Figure 52. The linear increase in voltage within this cell at constant current is likely to indicate that there was no transport occurring within this cell.

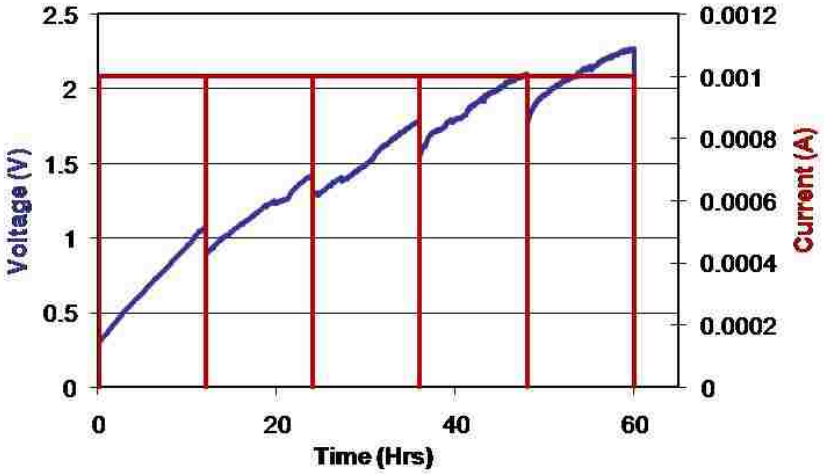

Figure 52 – Charge / Discharge curves for 2032 coin cells with a robocast polypropylene separator. Cathode material was robocast $LiFePO_4$ and anode was metallic lithium.

This ohmic behavior appears for long periods of time and only during the charge portion of the cycle. The constant slope for the voltage curve indicates that there is some associated capacitance to the cell. As soon as the discharge cycle is started, the current immediately disappears and no usable capacity can be measured in this battery. This shows that even though this material is the primary commercial battery separator material, without a pore formation step during processing it is unable to support discharge within a battery.

The PEO was printed in the same manner described for the polypropylene. Coin cells were assembled and cycled as seen in Figure 53. This type of behavior was the second type of cell response during these tests. The PEO material showed promise since the correct voltage for was able to be achieved.

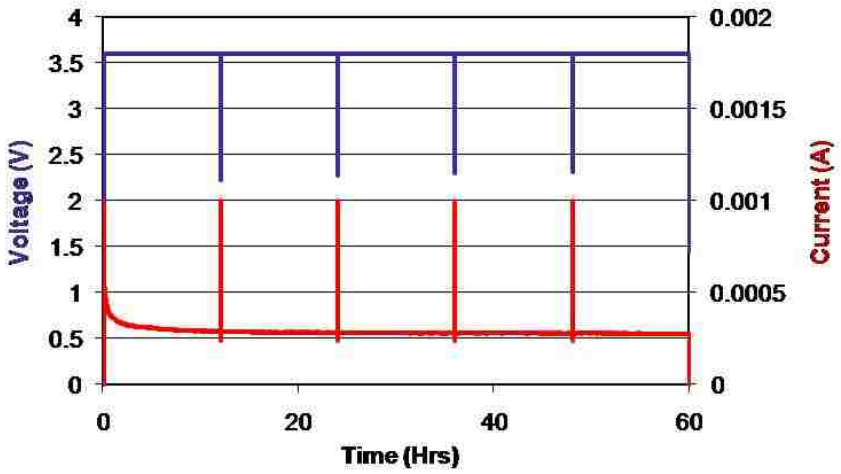

Figure 53 – Charge / Discharge characteristics for a 2032 coin cell with a robocast LiFePO4 cathode, metallic lithium anode, and robocast poly(ethylene oxide) (PEO) separator.

The voltage was completely constant in cells using the PEO material as printed, indicating that the transport within the cell was very poor. The discharge of these cells at 1 mA did not occur due to very poor transport within the cell. The cells proved to be unable to be discharged and the current immediately dropped to zero after switching tests

into discharge mode. This indicates that the PEO separator material without addition of any type of salt to increase conductivity is a poor choice for robocast separator materials.

The last type of behavior that was seen from the materials for printable separators occurred during cycling with the polyolefin / aerogel mixed separator. The separator was printed the same as both the polypropylene and the PEO but was mixed in an 18/82 w/w% of silica aerogel to polyolefin blend. The aerogel was ground to a fine powder with a mortar and pestle before mixing with the solvent and polymer. The resulting print was much different than the other two materials due solely to the addition of the aerogel. During print, the aerogel would filter press, resulting in concentrated areas of aerogel in the resulting film due to the press of solid being extruded in surges during the print. The printed separator was therefore very heterogeneous containing "islands" of solid porous material with interconnecting polymer films. These were processed and fabricated into coin cells and cycled the same as the other material tests for the separators, as seen in Figure 54. The battery with this separator was able to charge

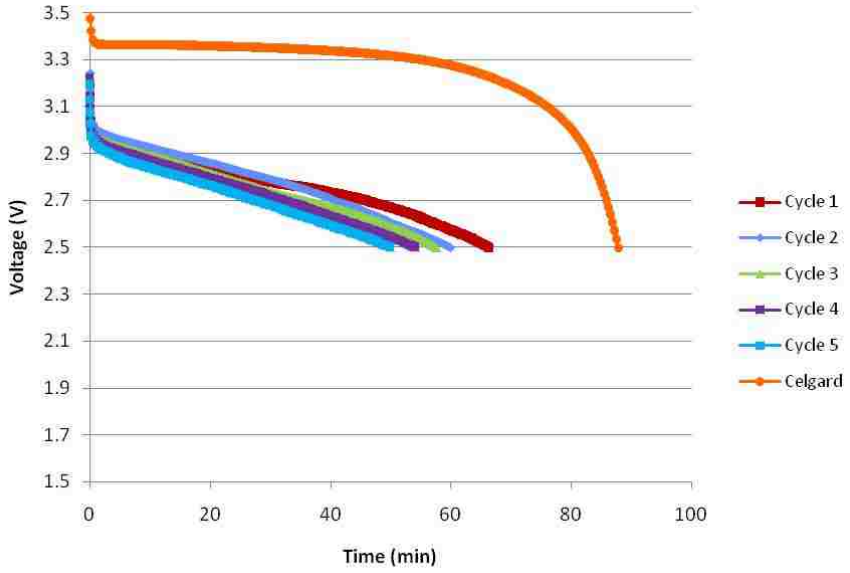

Figure 54 – Coin cell discharge curves for a battery containing a robocast LiFePO4 cathode, metallic lithium anode, and robocast polyolefin separator containing silica aerogel material for pore formation.

and discharge correctly. The ability to discharge indicates that the porous material created a percolative path through the separator film. Lithium ions were able to transport from the anode to the cathode during discharge through this percolative path. Figure 54 also includes (in orange) a discharge curve for robocast cathodes in a 2032 button cell with the same electrolyte but with a commercial Celgard 2325 separator. The five cycles shown for discharge of this cell exhibit a capacity of 42 mAh/g. For comparison, the capacity of the cell containing Celgard as the separator is 115 mAh/g. Cells containing the printed aerogel / polymer separator exhibited capacities as high as 59.5 mAh/g, but the average was significantly lower. Also, the very flat discharge plateau due to the $LiFePO_4$ is gone. This indicates that transport through the separator is the limiting step in the discharge rather than the intercalation into and out of the electrode material. There is a 5.5 % loss in capacity from cycle to cycle with this cell, indicating irreversibilities between the charge and discharge cycles.

These tests resulted in a very clear indication of the materials which are viable for printed separators in this investigation. Two of the three materials tested were unable to discharge with any useable capacity after fabrication into a coin cell (148). These materials were actually the materials which have the most commercial applications, but the inability to use subsequent steps after printing excludes them from viability for a printed separator using this method.

Evaluation of Binder/Aerogel Mixtures for Battery Performance

The mixture of chlorinated polyolefin and aerogel material provided a viable printable separator which was able to support lithium diffusion for charging and discharging of the cell. The creation of this material allows for the direct robocast deposition of the separator onto the cathode material. The lithium was added during the assembly of the coin cell. This method is a very viable way to made printed separators, but not without drawbacks. There was some difficulty in getting the material to print, due to the filter pressing exhibited during printing. This is the reason for the heterogeneous nature of the printed film. The chemistry involved with making the silica aerogel also proved to be strenuous and expensive. As mentioned previously, in "Battery Separator Considerations", the cost of the separator in a lithium battery can be up to 20% of the total price. This makes the use of this silica aerogel impractical. There are alternatives to costly silica aerogels, which are commercially available. One is the substitution of the silica for alumina aerogels. This exhibits very similar behavior, have similarly high porosity, and have several methods for manufacturing that makes it viable for use in battery applications (149-151). Commercial aerogel material (Aeropal® 400) was acquired from Sasol. This material has a surface area of 100 m^2/g and a pore volume of 1.8 mL/g according to the manufacturer. SEM images of the material can be seen in Figure 55.

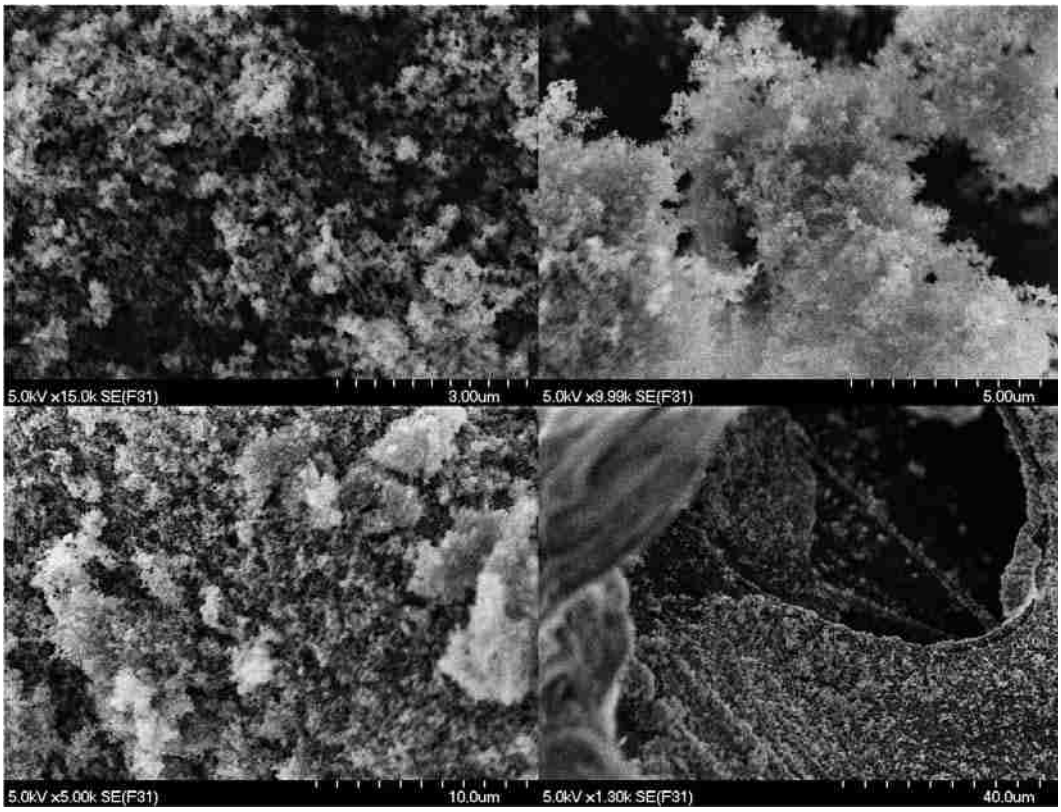

Figure 55 – SEM images of alumina aerogel alumina. Images show varying zoom levels at 5 kV accelerating voltage.

The images show the material to be very heterogeneous in the size of clusters present in the powder form of the material. The actual crystal size for the material is ~ 40 nm, which appears to be clumped together to make the fractal structure seen in the SEM images.

The solution for printing of the separator was investigated to optimize the polymer to aerogel loading. This is a balance between ideal polymer loading for battery capacity and ideal rheology for printing. The ideal condition for capacity with this type of printed separator exists in the situation when the entirety of the separator material is porous. This is obviously not feasible because there would be no adhesion to the cathode

layer underneath the separator. The maximization of the accessible area for transport is the key to a highly performing (good rate capability and high capacity) cell. The idea situation for printability is on the other extreme than that of the battery performance. This is the case when the material is completely suspended in a relatively low viscosity fluid (~ 100 cP) which exhibits no dilatant behavior when extruded through a print nozzle. This obviously excludes good battery performance since a film robocast in this type of configuration would be non-porous. Ideally, a compromise between the two can be found such that the polymer binder is present in low enough levels to allow diffusion through the porous network but high enough to promote adhesion of the aerogel to the cathode and itself.

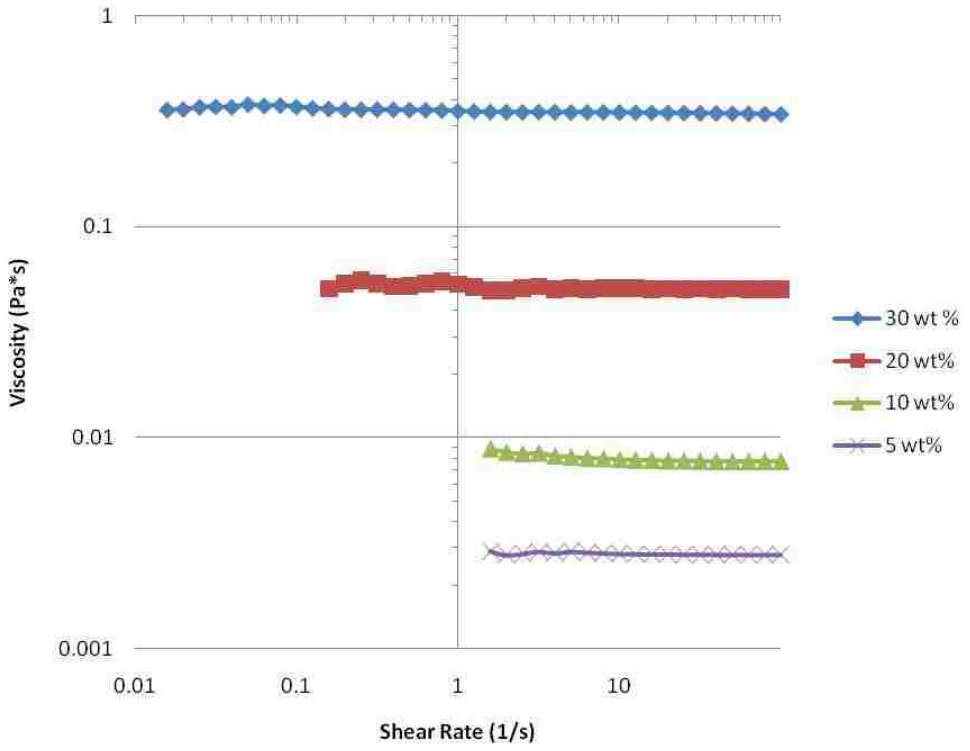

Figure 56 – Rheological evaluation of polyolefin mixtures in toluene. The solutions have no discernable response to increasing shear rate so they behave as a Newtonian fluid.

The rheology of this slurry was investigated starting with the evaluation of the supporting polymer solution to understand the optimal printing solution. Solutions containing several different loadings of polyolefin were mixed with Toluene and their rheological behavior was investigated, as seen in Figure 56. The solutions have no significant response to varying shear rate, indicating that they behave as a Newtonian fluid. This is beneficial for printing since Newtonian behavior is optimal behavior for printing. A fit of the data, as seen in Figure 57, shows that there is a relationship between the expected viscosity of a solution and the weight loading of the polyolefin with the relationship of:

$$\mu = 0.0011e^{0.192x} \tag{14}$$

where μ is the viscosity in Pa*s and x is the wt% of polyolefin in the mixture. This is the behavior for the polyolefin mixture in toluene but does not include the addition of the aerogel porous

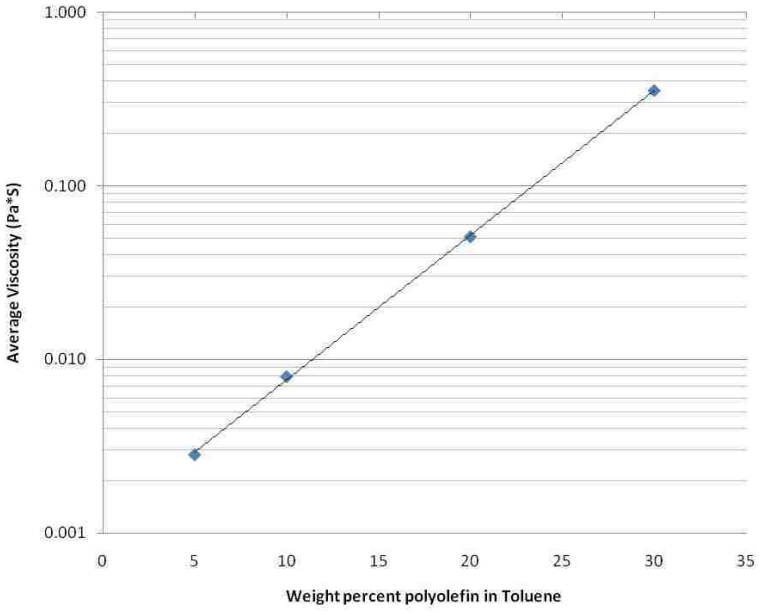

Figure 57 – Fit of the viscosity of a polyolefin polymer in toluene based on the weight percentage of polymer.

particles. Robocast cathodes and separators were printed onto the standard carbon coated aluminum substrates as mentioned previously in the section “Evaluation of Charge/Discharge Behavior for Printable Separator Materials”. Several of the separator slurries were unable to be printed due to the fact that there was not enough polymeric binder to support extrusion through a print tip. This resulted in many separator prints which were either non-existent or too sparse to create a continuous phase, as seen in Figure 58. Many of these prints were punched and assembled into coin cells for purposed of testing whether or not they would cycle at all, to limited success. The prints which yielded useable films were then punched into disks and assembled into coin cells as per the section titled “Evaluation of Charge/Discharge Behavior for Printable Separator Materials”. The electrochemical performance of the cells was evaluated by charging and discharging the cells at various rates to determine if the polymer to aerogel ratio affects the rate capability and capacity of the cell.

In order to understand the ability for the printed cathodes and separators, cells were constructed and cycled at varying currents. Each battery contained a separator which has a different loading of polymer, so each had a widely different C rate based on the currents used for the discharge. The data is shown as specific capacity since each cell was the exact same size and same form factor. The

Figure 58 – Example of printed separator which exhibits separation upon printing, resulting in a non-cycleable battery.

currents for discharge were 0.1 mA, 0.5 mA, 1 mA, 5 mA, and 10 mA. The results from the discharge rate tests can be seen in Figure 59. The primary trend seen is that the higher the polymer loading, the higher the cell capacity. This is very counter-intuitive as it is normally accepted that less polymer binder that is present in the separator, the better the transport through the separator would be, due to the lower tortuosity. Due to printing considerations, the higher polymer containing samples actually print much better and create a uniform film with very little cracks or holes. In contrast, the 5 wt% and several of the 10 wt% samples (not shown for discharge) were completely unable to be printed due to their very high viscosities. These samples were so viscous that there was no possibility for them to even be drawn through the tip of a commercially available syringe even without a print tip. Attempts to even doctor blade these samples proved unable to create a film which was continuous enough to punch out a cathode/separator for assembly into a 2032 coin cell.

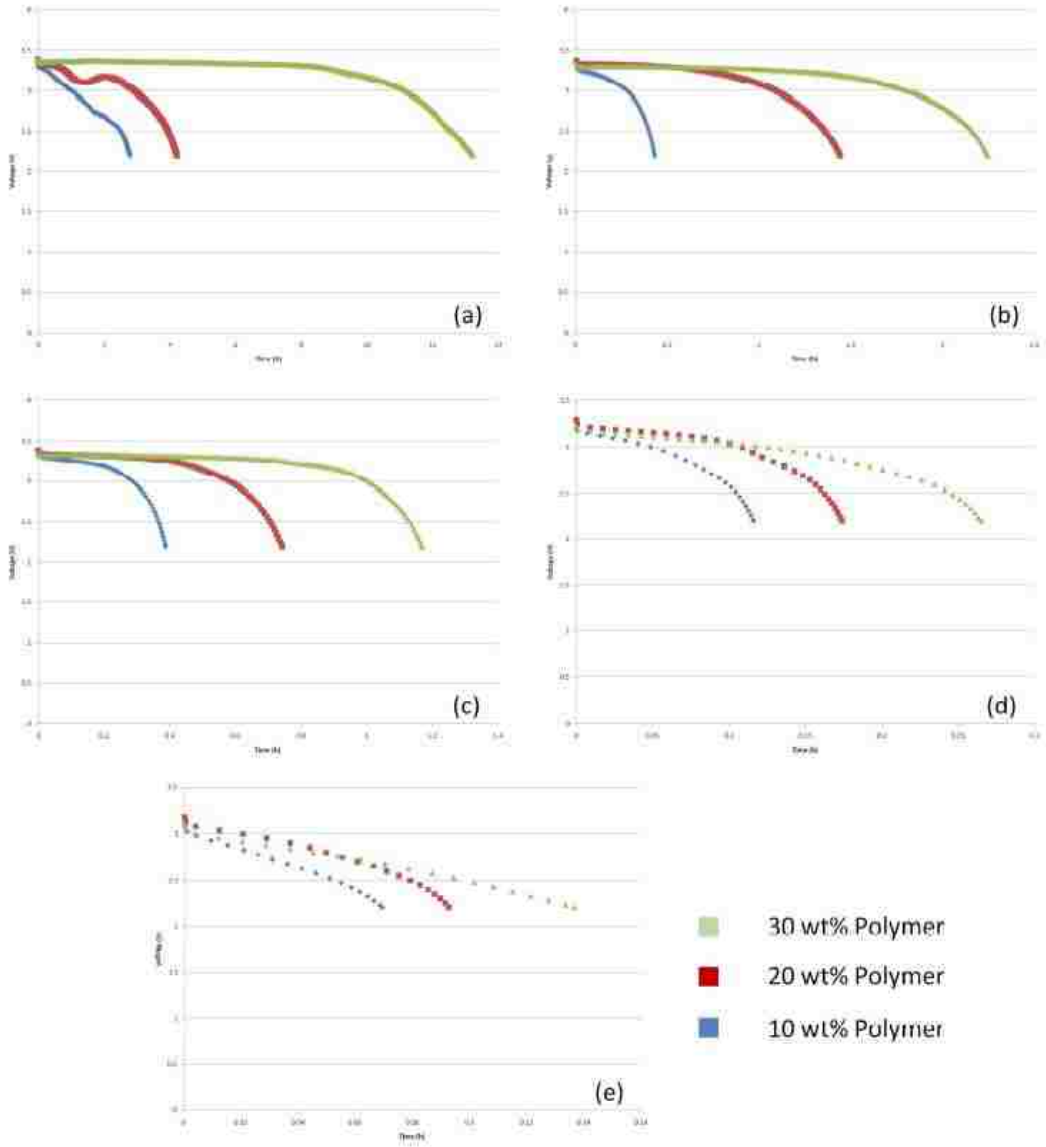

Figure 59 – Rate characterization for 2032 coin cells with robocast $LiFePO_4$ cathodes and polymer/aerogel robocast separators. Each plot shows separators containing a ratio of polymer/aerogel (w/w) at values of 10/90, 20/80, and 30/70 (blue, red, and green). Discharge rates are a) 0.1 mA, b) 0.5 mA, c) 1 mA, d) 5 mA, and e) 10 mA.

The relationship between viability for use in a printing deposition method and battery capacity or rate capability is a very important result. The fact that such a relationship exists implies that there will be an inherent sacrifice of battery performance

for the benefits of a printable cell configuration using this material set. In order to create cells which can be customized to any form factor there is a trade-off that is made in the form of battery capacity. The overall size of a cell which has been printed with a polyolefin/aerogel hybrid separator should be adjusted to ensure that capacity and rate capability will be met for the application at hand.

The resulting capacities for each of the discharge rates can be seen in Table 3. From this table, it can be seen that there is a relationship between the polymer loading and the capacity of the cell. The higher polymer loading samples exhibited a much higher capacity than the lower polymer loading samples. There is a fivefold increase in the capacity between the 10 wt% and the 30 wt% polyolefin separators. One explanation of why that is the case is due to the impedance of the interface between the cathode and the separator.

Table 3 – Rate capability results for printed aerogel and printed $LiFePO_4$ cells.

Polymer wt%	Rate (A)	Specific Rate ($\mu Ah/cm^2$)	C Rate (with respect to first discharge)	Capacity (mAh)
10	0.0001	50.52	0.36	0.28
10	0.0005	252.59	1.79	0.21
10	0.001	505.15	3.57	0.39
10	0.005	2525.54	17.87	0.58
10	0.01	5052.22	35.75	0.69
20	0.0001	50.52	0.24	0.42
20	0.0005	252.63	1.18	0.72
20	0.001	505.22	2.36	0.75
20	0.005	2524.38	11.81	0.87
20	0.01	5053.39	23.64	0.93
30	0.0001	50.52	0.08	1.33
30	0.0005	252.71	0.38	1.12
30	0.001	505.22	0.75	1.17
30	0.005	2524.38	3.76	1.32
30	0.01	5051.07	7.53	1.37

The cell capacities based on polymer loading are counter intuitive from the generally accepted knowledge of slurry formation. In the case of the robocast battery separators, the addition of non-porous polymeric binder actually increases capacity. Many of the formulations for slurries that are used in batteries actually try to minimize the polymer loading in order to allow for more electrolyte to exist within the separator. This trend can be illustrated by the capacitances of the cells at the very beginning of the discharge for each value of current. The separator for the printed batteries was a tri-phase system consisting of the polymeric binder which was supporting the alumina porous phase while the liquid electrolyte penetrated and filled the porous phase. The ratio for each of these phases varies, so the capacitance change seen in the discharge curve can be compared to the theoretical values for capacitance based on a three capacitors in series. The slope of the discharge curves were determined via linear fit on the discharge curves seen in Figure 60. The magnitude of the values for the discharge slopes can be seen in Table 4.

Table 4 - Initial discharge slopes of printed $LiFePO_4$ cathodes and printed polymer/aerogel separators at varying discharge current.

Polymer Loading	Current (A)	Initial Slope (V/h)
10	0.0001	0.2909
10	0.0005	0.702
10	0.001	0.429
10	0.005	3.102
10	0.01	9.4294
20	0.0001	0.0593
20	0.0005	0.0392
20	0.001	0.1391
20	0.005	1.29
20	0.01	5.202
30	0.0001	0.0058
30	0.0005	0.0185
30	0.001	0.0575
30	0.005	1.26
30	0.01	4.602

The capacitance can be calculated according to:

$$I = C\frac{dV}{dt} \tag{15}$$

where C is the capacitance in Farads. Based on the slopes of the discharge curves (dV/dt) from Table 4 and the current for the discharge the capacitances for each polymer loading cell can be calculated. The capacitances for the printed cathode and separator batteries can be seen in Figure 60. The increase in the capacitance based on the polymer loading is the primary result from the experimental data.

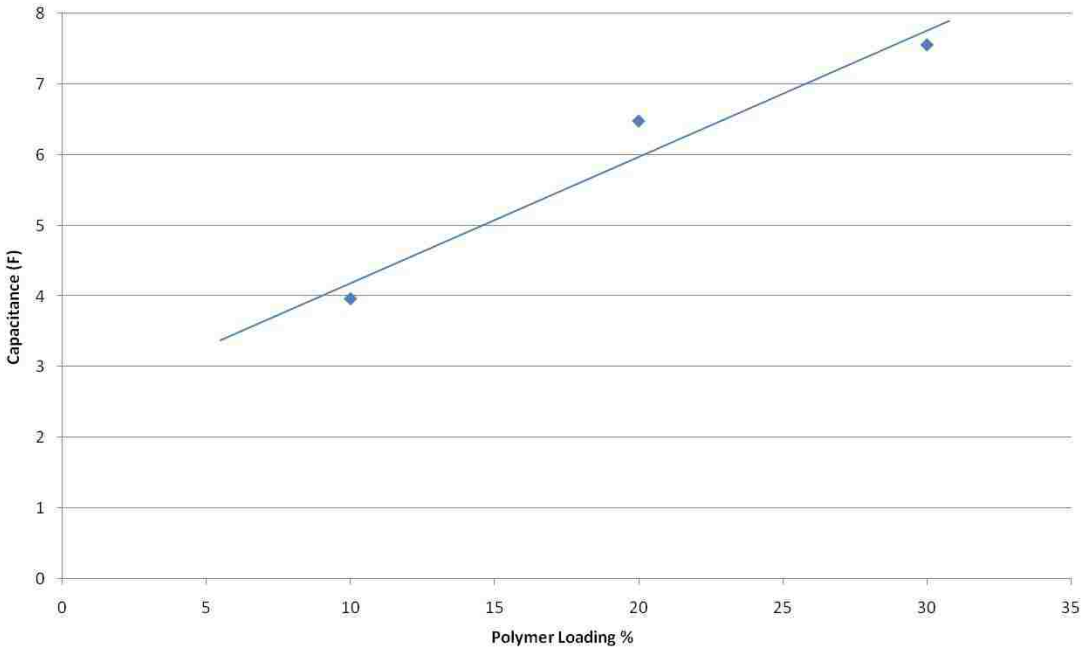

Figure 60 – Capacitance of printed cathode and separator cells based on initial discharge.

To understand the more conventional understanding of what is occurring within the printed cells, we can model the separator as the three phase system. The polymer, the porous aerogel, and the battery electrolyte each have a different capacitance in the system and each contributes to the overall capacitance depending on their relative amounts in the separator. The schematic for the calculation can be seen in Figure 61. The contribution of capacitors arranged in parallel can be calculated using:

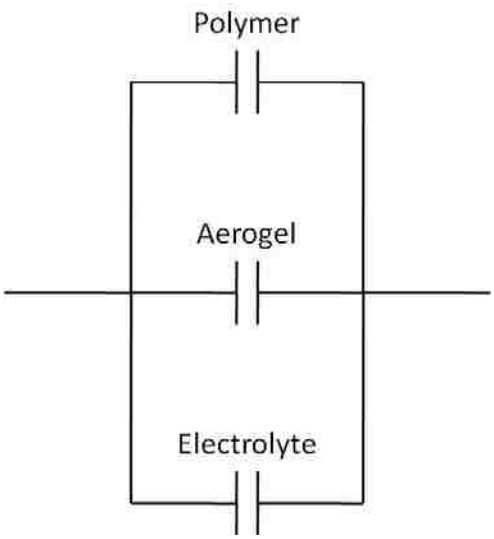

Figure 61 – Schematic for calculation of capacitance within printed cell.

$$C_T = x_1C_1 + x_2C_2 + x_3C_3 \quad (16)$$

where C_T is the total capacitance, $C_{1\text{-}3}$ are the capacitance of each contributing member, and $x_{1\text{-}3}$ is the fraction that each capacitance contributes to the overall capacitance. The value for each of the dielectric constants or relative permittivity were taken to be 2.02E-11 F/m for the polyolefin blend (152), 8.46E-11 F/m for the alumina (153), 5.70E-10 F/m for PC, 8.44E-10 F/m for EC, and 2.74E-10 F/m for DMC (21, 154). Using the relative contributions for each of the individual electrolyte components, the overall dielectric constant for the electrolyte was calculated to be 2.99E-10 F/m. The electrolyte dielectric constant is significantly higher than the dielectric constant for both the polymer and the porous component of the separator. Since the batteries were tested in the same geometry

(2032 coin cell) and the print conditions were held as constant as possible, the capacitance of the cells were dependent on the overall dielectric constant based on the proportions of each of the three materials present in the printed separator. A plot of these capacitances can be seen in Figure 62.

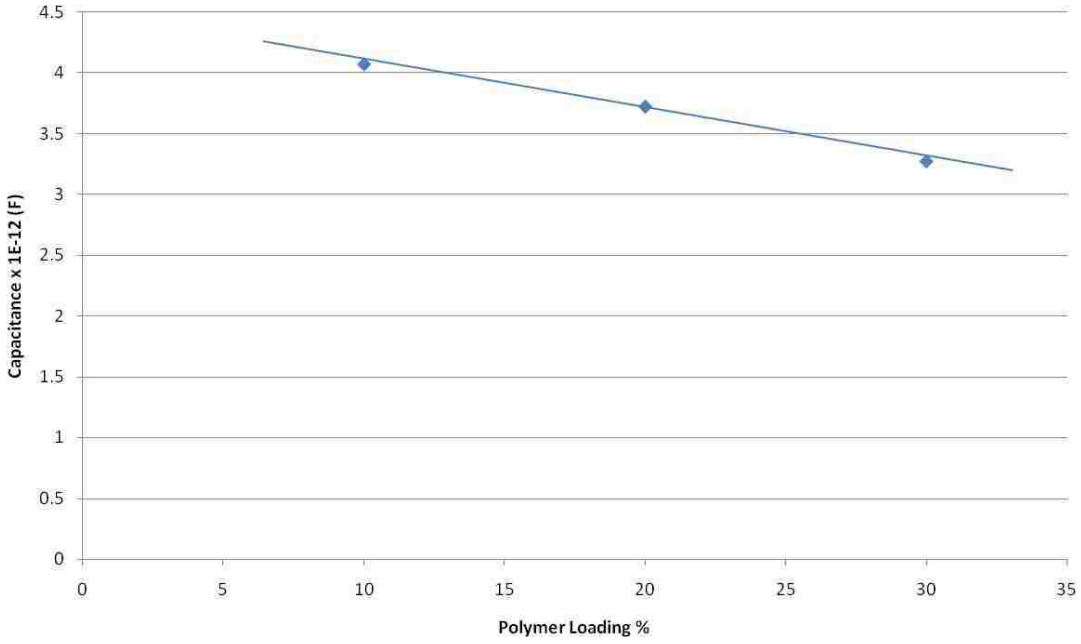

Figure 62 – Capacitance of batteries based upon materials and geometric considerations.

The relationship between the loading of the polymer and the capacitance is negative when calculated based on the materials within the cell. Increasing the polymer loading in the cell should result in a decrease in overall capacitance according to the calculated values for capacitance. This directly contradicts the results from the actual printed separator experiments. The increase in loading of the polymer should mean that the overall contributions of the aerogel and electrolyte should decrease. Since the dielectric constant for the electrolyte is higher than that of both the polymer and the

aerogel, that should mean a decrease in the capacitance of the cell. The prediction for the relationship that should be occurring is exactly opposite of what was seen experimentally. This indicates that there is another explanation for the increase in capacity and increase in capacitance with increasing polymer loading within the printed separator.

A possible explanation for the counter intuitive relationship seen between polymer loading and battery capacity is based on the impedance of the interface between the printed cathode and the separator. By printing each layer directly onto the last, there could be a potential to decrease the impedance between the two. Because each layer within the cell stack is formed contacting the next layer, there could be minimal impedance as compared to forming each layer individually and then stacking them into the cell. The decrease in impedance could explain why there would be an increase in battery performance with increasing polymer loading. This is due to the fact that the increased polymer loading samples were more amenable to deposition using a printing technique. Since the higher polymer loading samples contain more polymer and exhibit better print characteristics based on their rheology, the interface between the printed separator and printed cathode is potentially less resistive and more uniform than the lower polymer loading samples. If there is a much more uniform and intimate interface between the printed cathode and the printed separator, which would occur with slurries that exhibited optimal print conditions, then the impedance of the battery could be reduced. This reduced impedance could enable for better performance solely based on the contact of the battery layers.

Cells containing printed aerogel/polyolefin separators were examined using EIS to determine the overall impedance within the cell. The results of the measurements can

be seen in Figure 63, as shown in a Nyquist plot and Figure 64, shown in a Bode plot configuration.

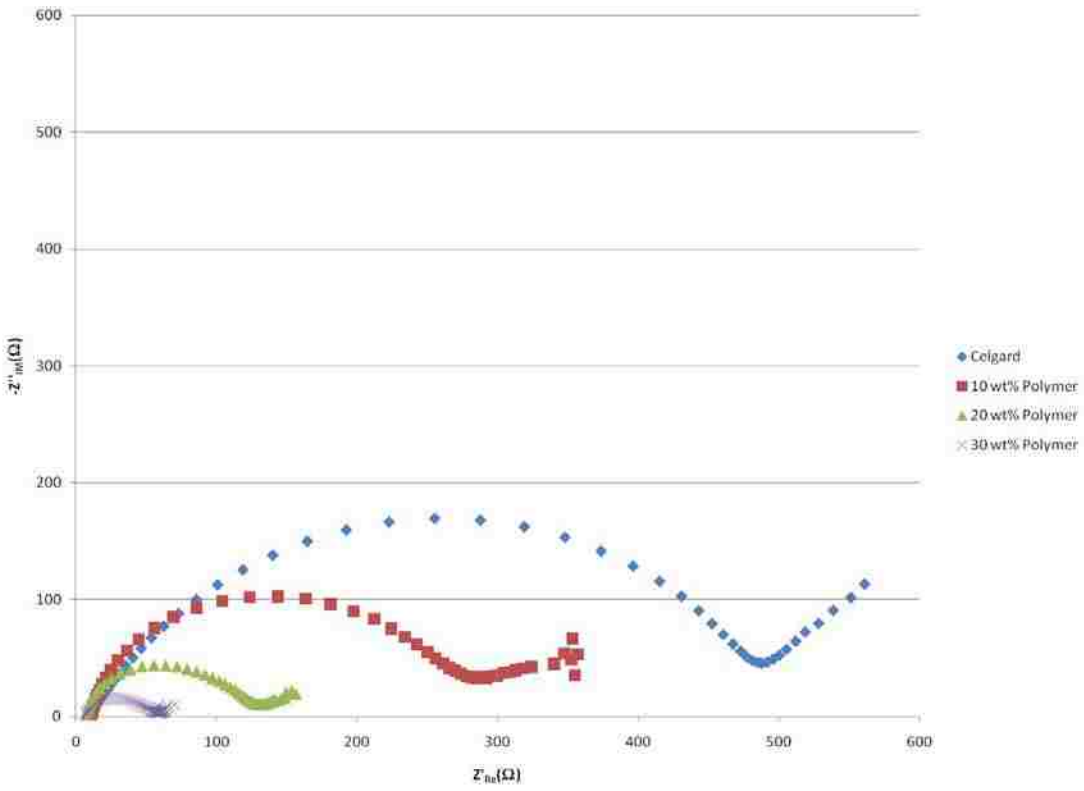

Figure 63 – Nyquist plot showing the comparison of 2032 coin cells that contain a printed $LiFePO_4$ cathode and a printed polyolefin/aerogel separator. The separator was printed directly on top of the cathode.

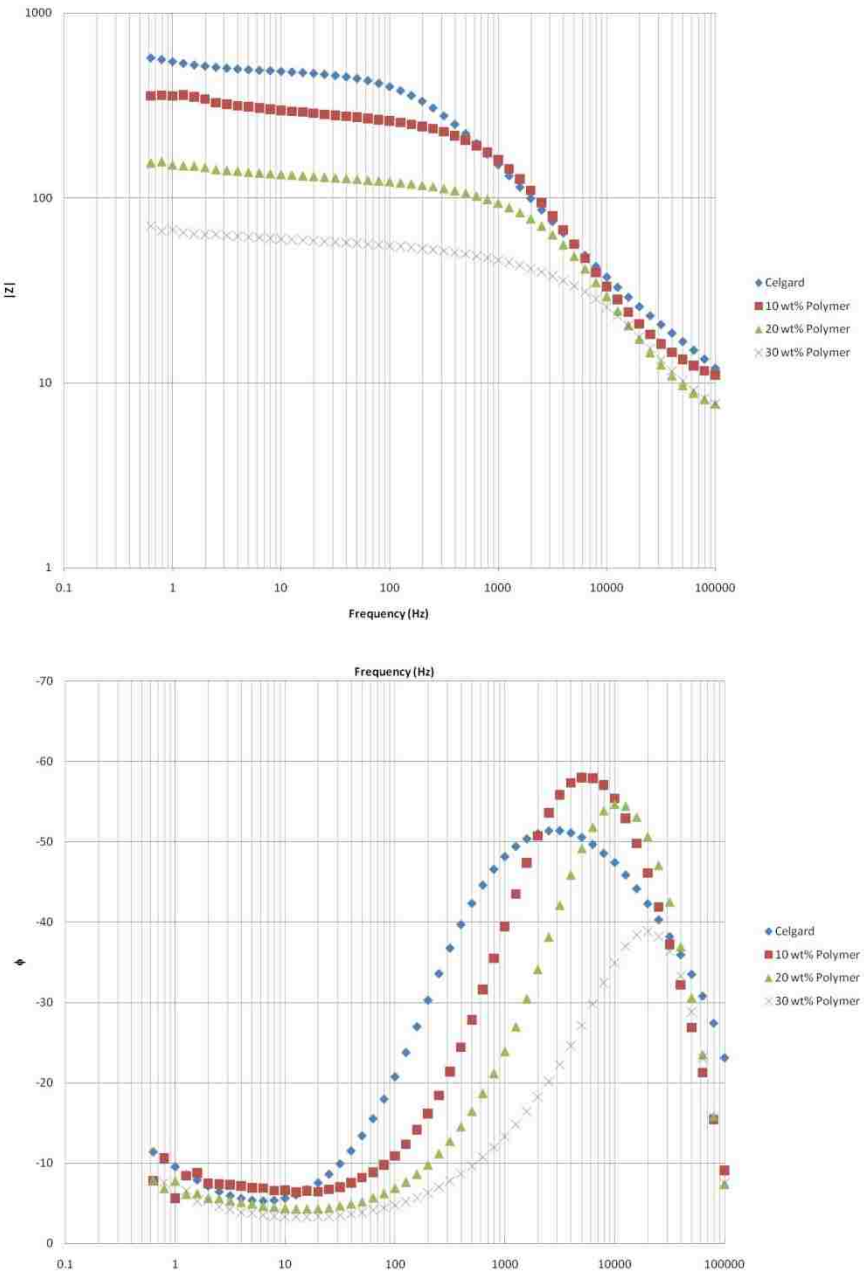

Figure 64 – Bode plot comparing 2032 coin cells which contain printed cathodes and either a commercial Celgard separator or robocast separators containing various amount of polymer/aerogel loading.

The primary result of interest from Figure 64 is the overall impedance for the cell. At low frequencies, where diffusion of the lithium ion is of primary importance, there is an explanation for the fact that the higher polymer loading printed separators have better

electrochemical performance. The impedance of the battery containing the Celgard separator at the lowest frequency is 570 Ω. The impedance of the printed polyolefin/aerogel separators are all lower than the commercial separator at 10 wt%, 20 wt%, and 30 wt% polymer impedances being 355 Ω, 155 Ω, and 70 Ω. This supports the hypothesis that by printing the separator immediately upon the cathode it is possible to lower the impedance of the cell by ensuring an excellent contact between the cathode and the separator at the interface. The fact that the higher loading of polymer has the lowest overall impedance suggests that by having extra liquid polymer in the slurry during the print, the interfacial impedance is minimized. The liquid phase polymer seems to penetrate the micropores and cracks on the surface of the cathode, thus minimizing the impedance of the resulting cell.

One way to visualize the physical orientation of the interface and the reason for the decrease in impedance with increasing polymer loading is to first approximate the surface of the cathode as a packed array of spherical particles. The close packing of the particles assumes that the upper hemisphere is what will be exposed during printed of the separator. The SEM micrographs from Figure 37 show that the particles are not necessarily spherical and do have a fairly broad particle size distribution. Using the average particle diameter, the coverage can be calculated for each particle based on the resulting impedance for the interface.

The calculation of the effective surface area for each of the samples was taken from a standard surface area integral for a sphere in spherical coordinates.
The polar angle (θ) is integrated between the angle in question (x) and $\pi/2$ because of the assumption that the spheres are close packed. The angle x can be quantitatively solved

for based upon the relative impedance measurements and the area of the upper hemisphere of the spherical particle, as seen in Figure 65.

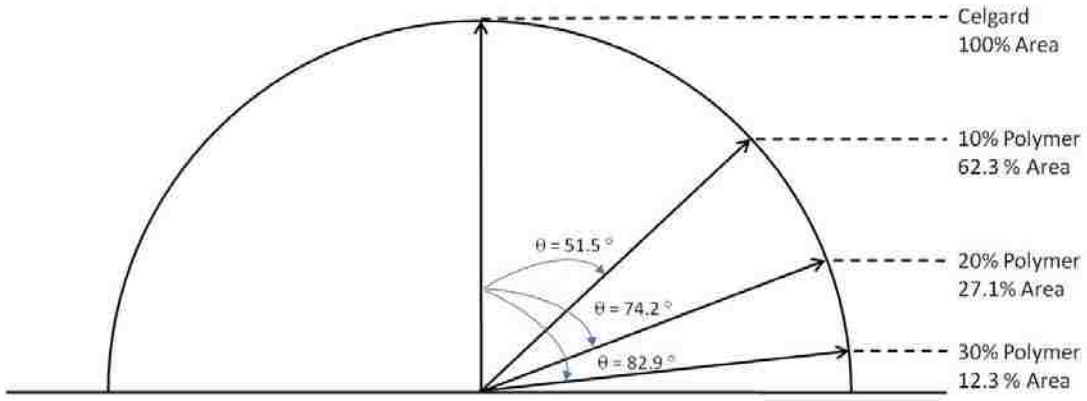

Figure 65 – Surface area coverage of the polymer on the battery active materials based upon the impedance difference based on polymer loading.

The area of coverage for the Celgard containing cells, which have the highest impedance based upon the EIS measurements, is the situation where the entire surface area is uncovered by the separator. The polymer of the printed separators for the 10%, 20%, and 30% polymer loading occupy 62.3%, 27.1%, and 12.3% of the surface area of the particles on the cathode. The reduction in surface area between the cathode particle and the separator leads to the reduction in impedance of the interface between the two layers. This evaluation for the contact between the two printed layers within these cells demonstrates the reason for the reduction in impedance with increasing polymer loading but is not a literal explanation. The reduction of surface area coverage based upon the polymer loading may not follow exactly the polar angle on the particles. The overall reduction in contact between the porous portions of the printed separator is distributed

along the particles themselves and may not be located in the exact physical position as indicated by Figure 65.

While the impedance of the printed cells did decrease with increasing polymer content, it should be noted that this is only applicable to the case of printed batteries. The ability to print a continuous layer seems to have more of an effect on the battery performance than any other factor. The polymer was able to help stabilize the interface between the cathode and the separator for these cells. This is solely because the higher polymer content separators were more able to be printed using the robocasting technique. Obviously, the extreme case where only polymer and no porous media is present would perform terribly in a battery (as seen in Figure 52) but that is the implication from the tests for battery performance based upon printing separators. The physical act of printing a separator for use in a lithium cell makes the conventional knowledge of slurry formulation different. If an extrusion process is used, the lowest loading of binder may not be the best choice for the battery capacity. The correct formulation for the printed separator will inevitably be based on the application for which it is intended. The tradeoff between printability and battery capacity becomes a very important factor when developing printable materials for lithium batteries.

CHAPTER 6: RESEARCH CONCLUSIONS AND FUTURE DIRECTIONS

The cathode formulation for printing using the robocasting technique was determined based upon trial and error using a common formulation for $LiFePO_4$ cathode slurry. Due to the high cracking exhibited when sprayed using an aerosol technique, the extrusion technique was determined to be the most reliable deposition method. Robocast cathodes were examined with SEM to determine the average particle size was ~ 2 μm and the grains were very heterogeneous in morphology. The examination of EDS for the printed cathodes indicates no significant presence of impurities occur during the printing process. The printed cathodes were assembled into both 2032 coin cells and pouch cells for electrochemical performance testing in both constant current and pulsed current discharge modes.

The electrochemical discharge characteristics showed that the printed $LiFePO_4$ cathodes were able to supply up to 110 mAh/g of material, which is lower than the theoretical capacity of the material but is a realistic value for operational full cells. The rate capability of the cathodes indicates that at currents higher than 2C the capacity of the cells fades dramatically. The lifetime of the printed cathode batteries indicated a reduction in capacity of 11% after 60 cycles. The ability to print the cathode material with good electrochemical performance is an enabling technology for use in many applications. The robocasting technique allows for the deposition of cathodes in virtually any configuration for assembly into a full battery.

The development of a printed separator designed to be printed directly onto a printed cathode started with the selection of a materials set that was compatible with the robocasting extrusion technique. Since the robocast cathodes were printed using this technique, a compatible separator material is important to facilitate ease of fabrication for a printed cell. Three materials were tested for viability for use with the robocasting technique through print tests at various polymer loadings to identify the correct loading for printing based on viscosity. The PEO and polypropylene were determined to be unsuitable for use as a separator with the robocasting technique due to no electrochemical performance. The polyolefin blend containing porous aerogel was identified as a suitable material for a printed battery separator. This material was able to be electrochemically charged and discharged.

The capacity of the printed separator containing cells was tested and determined to be up to 60 mAh/g in a 2032 coin cell. The rate performance of the robocast cathode and separator was investigated by cycling with discharge currents of 0.1, 0.5, 1, 5, and 10 mA using separators with varying loading of polymeric binder material as compared to the porous aerogel. The initial understanding of the system indicated that there the lowest possible polymer loading should result in the best capacity and rate performance, however, the sample containing the highest polymer content (and therefore lowest portion of porous media) was found to have the highest capacity at all discharge currents tested. This complex phenomenon that occurs within the cell when using printed techniques for layer deposition within a cell was obviously based upon something other than polymer loading.

A capacitive model was used to understand the theoretical trend which consisted for three capacitances in parallel. This showed that there actually should be a decrease in capacitance for the cell with increasing polymer loading based on initial rates for discharge at the tested discharge currents. To better understand why the act of printing the battery materials exhibits the opposite trend, impedance spectroscopy was performed to investigate the interfaces within the cell. The highest polymer loading samples were shown to have the lowest overall impedance. The extra polymer content within the printed slurry seems to fill in the unoccupied areas on the surface of the cathode substrate during the printing thereby resulting in lower electrical impedance between the layers. This coating of the cathode material allowed for focused transport to occur through the porous constituent of the printed separator. Reducing the impedance of the interface by directly printing higher polymer loading separators led to increased battery performance.

The development of a small volume printable battery using the robocast deposition technique aimed to try and reduce the size of $LiFePO_4$ cells and enable unique electrode geometries to be printed. The resulting cells were similar in size to many of the thin film and small cells available, Figure 66. The types of cell created exhibited similar energy density as compared to the more traditional battery types and chemistries.

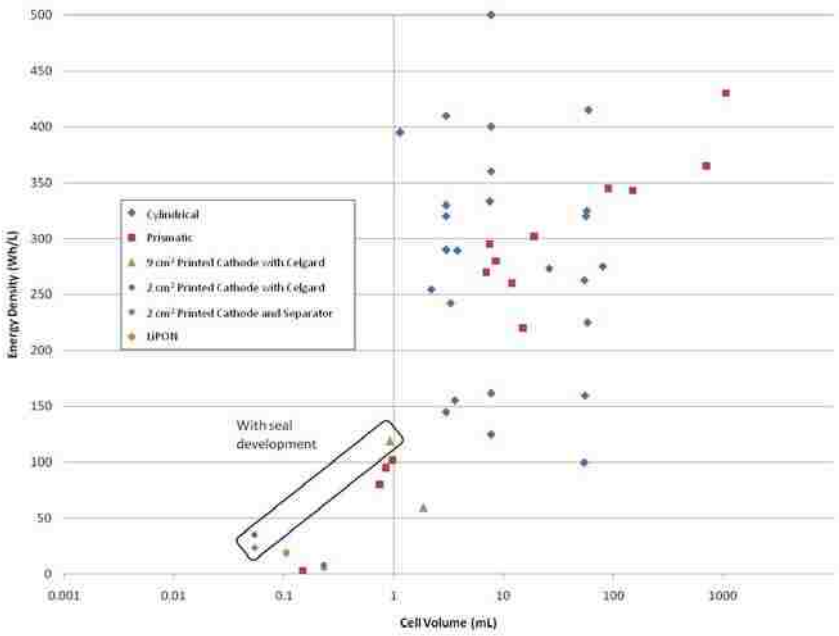

Figure 66 – Energy Density comparison based on cell volume for various battery types including printed cathodes with commercial separators and printed cathodes with a printed separator.

The plotted data shows 9 cm^2 and 2 cm^2 cells which contain 200 μm thick packaging and their positions based upon the energy capacity from the results of the electrochemical discharge behavior as compared to traditional battery chemistry and geometries. The three cell types shown indicate that the robocasting technique is capable of producing batteries which have respectable energy capability compared to other commercial cells. The volume of the smaller cells is still larger than the sputtered thin film batteries (shown in orange). Further refinement of the method for producing these batteries is needed to really shift the energy density of these cells past the solid state batteries. Highlighted in Figure 66 with a rectangle are the cells which are potentially creatable using this technique with the development of a water and oxygen impervious seal. By eliminating

the excess packaging material, the energy density of the robocast batteries could be enhanced greatly. This would allow for even smaller cells and higher energy densities than sputtered thin film cells.

The development of printable package material and a printable seal are the primary next steps for this research. The development of a printable package is difficult due to the need for the package to be impervious to water and oxygen diffusion. This issue is easily solved through use of metal containers traditionally, but printing a metallic film that can be uniformly deposited upon an already printed stack of battery materials is a very non-trivial problem. The other option for this dilemma is to use metallic current collectors for the printing substrate and then use a seal to essentially cap the cell. The oxygen and water transport needs to also be understood at the seam or interface between a printed package and the substrate. This seal should be robust enough to allow for mechanical manipulation of the battery and reliably exclude the transport of atmospheric chemicals into the cell. This development will allow for numerous new applications for lithium batteries which are currently unavailable due to size constraints.

Appendix

Development of Printable Seals

The development of printable seals for lithium batteries relies on the use of a thermoplastic polyolefin blend which can be printed onto the substrate to surround a printed cathode. This would enable the use of the current collector as the package and would eliminate 200 μm of thickness from a lithium pouch cell. A demonstration of a battery made in this way can be seen in Figure A1. The main requirement for this type of seal is that it must be able to prevent the diffusion of water and oxygen into the battery.

The printable polyolefin blend used in the printable separator investigation was used due to the thermoplastic behavior of the material. Application of heat to the polymer creates a seal to metallic surfaces such as aluminum or copper, making it a suitable choice for fabrication of a seal. The material was printed on samples of aluminum current collector and copper current collector foils. Then a seal was made between the samples and another sheet of copper or aluminum foil using an impulse sealer. The adhesion between both materials using the thermoplastic seal was suitable for cell fabrication and was ~ 60% as strong as the bond created with an impulse

Figure A1 – Schematic of a cell fabricated using a printable seal. The aluminum cathode current collector and printed LiFePO4 cathode are seen at the bottom of the stack. The copper anode current collector, lithium metal, and commercial separator are shown on the top of the stack.

sealer between the layers of a traditional pouch cell. This verified the possibility for use of the material as a seal.

In order to investigate the transport properties of the material a diffusion test apparatus was designed and constructed, as seen in Figure A2. The apparatus consisted of two chambers, which are on the top and bottom of a metal disk which is held in position with an o-ring on top and bottom of the metal disk. Each chamber can be independently filled with either nitrogen or oxygen gas. By bubbling the gas through a humidifier unit allows for the control of the humidity within the chamber. Each chamber contains both a humidity and oxygen sensor. Placement of a material onto a metallic disk with known area for diffusion to occur allows for the quantification of diffusion rate for both oxygen and water from one chamber to the other.

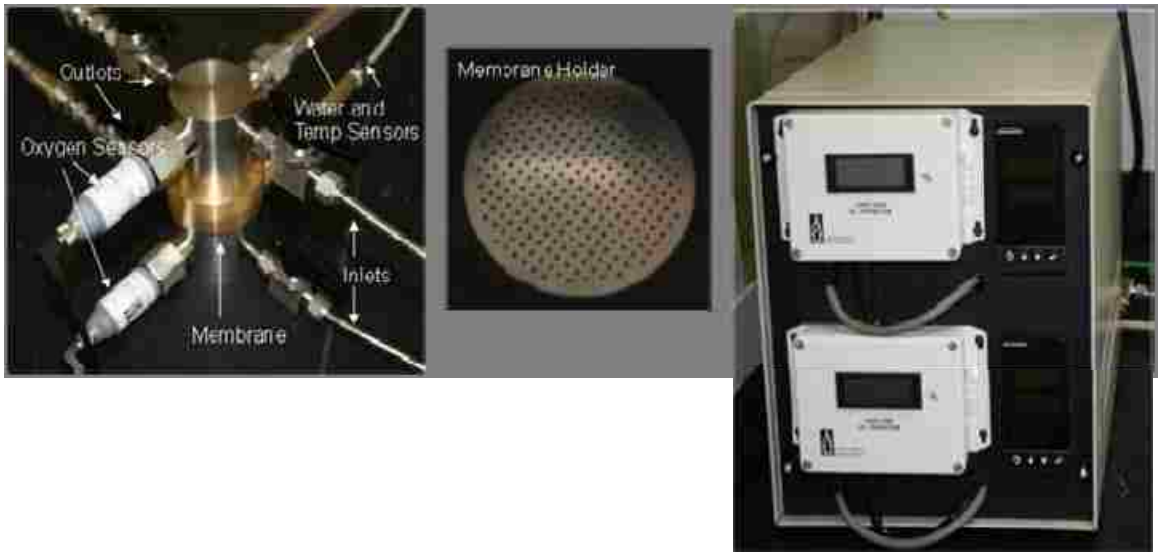

Figure A2 – Diffusion test apparatus setup.

To determine the baseline for the apparatus a solid meta disk was used to separate the chamber from the bottom chamber. Both chambers we filled with nitrogen gas. Eac chamber was then cut off fro supply and the outside environment and allowed to s while the oxygen content wit each chamber was monitored seen in Figure A3. The same was performed with oxygen i top chamber and nitrogen in t in the background leak rate depending on the gasses present in the top chamber, Figure A4. All of the tests indicated that there is a constant leak rate of 0.056 % O_2/min in the test chamber.

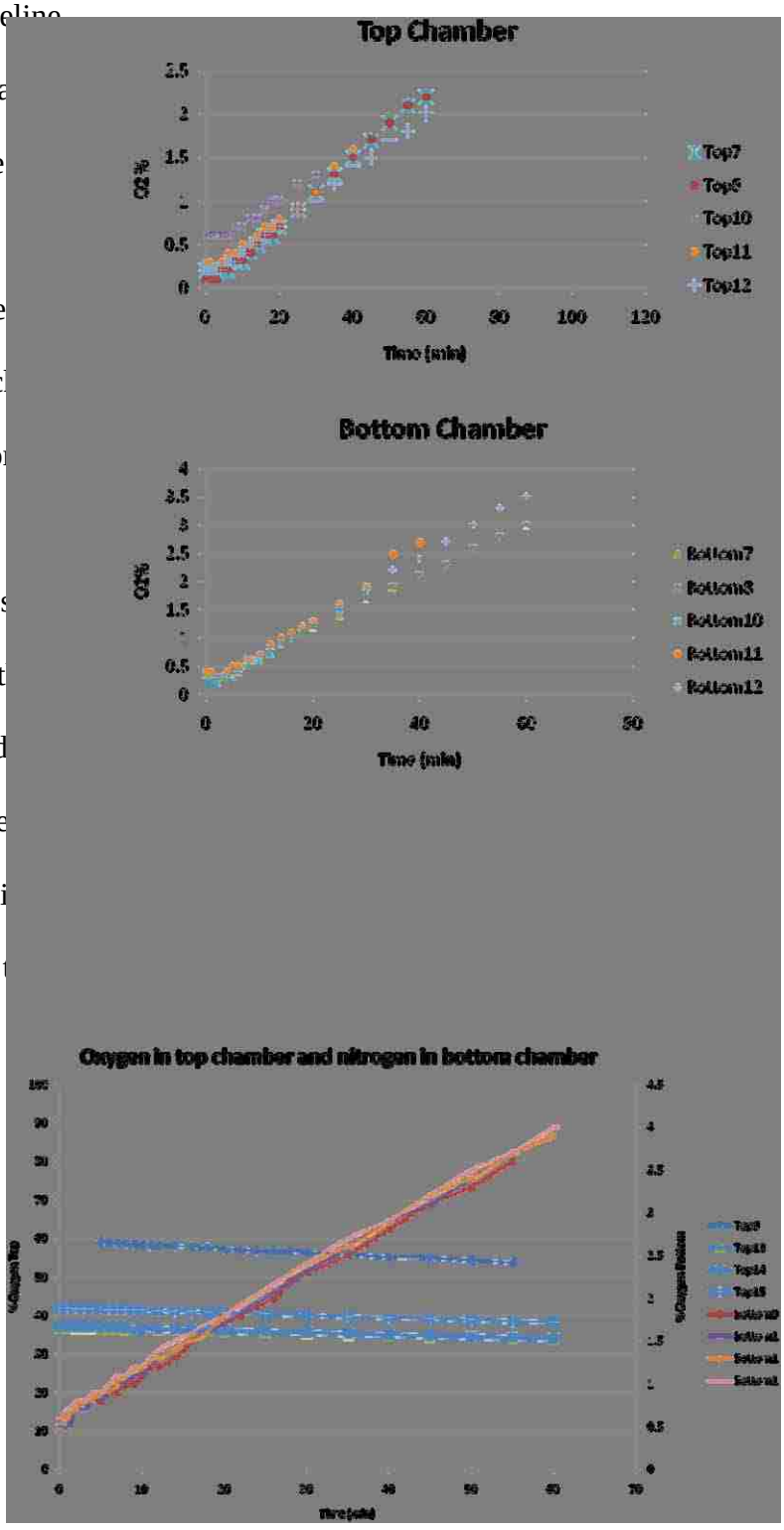

Figure A4 – Leak rate determination with oxygen in the top chamber and nitrogen in the bottom chamber. The curves in blue indicate the oxygen reading in the top chamber.

The metallic plate was then replaced with a plate containing 1 mm diameter pores. The pores were filled with the polyolefin material so that the diffusion of the gasses occurs through the polymer. The filling of the pores was done by attaching the metallic disk to dicing tape and doctor blading the polymer over top of the metallic shim. This process was repeated several times until the pore was entirely filled (confirmed via profilometry). The same test was conducted for determination of the diffusion rate of oxygen through the polymer using the diffusion test apparatus, as seen in Figure A5. The apparatus was setup with nitrogen in both chambers then oxygen was introduced into the top chamber. The system was isolated and the measurement of oxygen in both chambers was monitored. Since there is an inherent leak rate in the system, this was used to normalize the data seen in Figure A5.

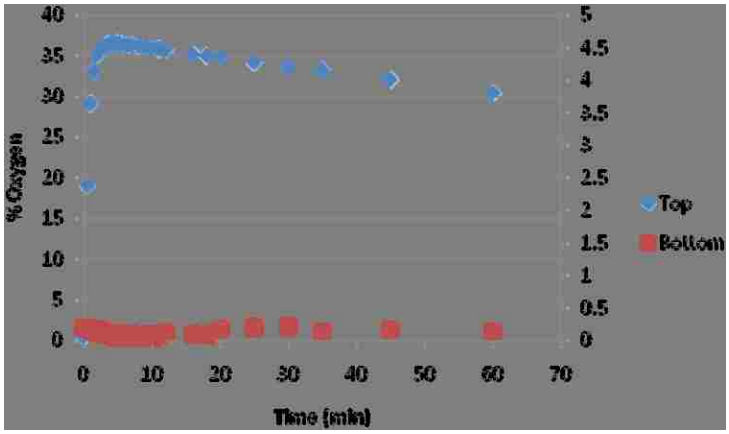

Figure A5 – Oxygen diffusion through the polyolefin material.

The determination of water diffusion through the polymer material was much more difficult. This was due to an issue with the water sensor hardware. The detection of water in any situation showed erroneous results. The leak rate tests indicated that the humidity sensors were incompatible with the system due to erroneous data for tests conducted with oxygen in the top chamber and nitrogen in the bottom chamber, as seen in Figure A6. The increase in water levels within the chamber without the introduction of

any humidity indicates that there is an error in the detection system for the humidity sensors. This test was repeated with several different oxygen and nitrogen sources with the same result.

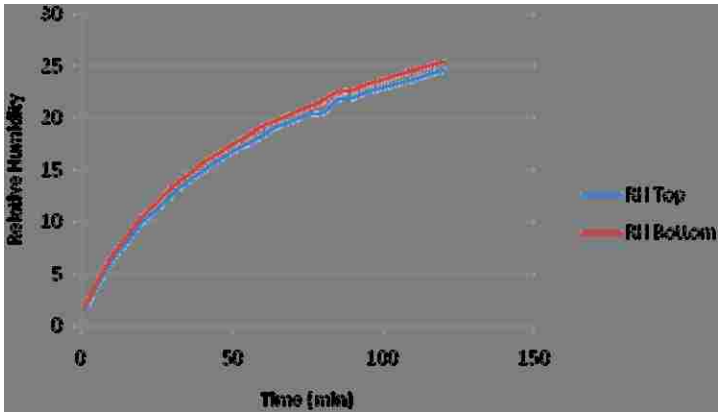

Figure A6 – Response of the humidity to nitrogen in the top and bottom chambers.

The design of the diffusion apparatus and choice of sensor hardware made it difficult to determine the diffusion rate through the printable seal. The sensors were unable to accurately read the necessary humidity and oxygen levels. Also, the system leaked during testing, which necessitated the use of a baseline. For the development of a printable seal for lithium batteries this is unacceptable. The danger involved with the introduction of water within a battery necessitates full understanding of the transport properties for the seal. The estimation of the rate based upon a leak rate baseline was deemed unacceptable for this research. The knowledge gained from these tests can help future attempts to quantify the transport through a printable seal material.

REFERENCES

1. C. Vincent, *IEE Review*, **45**, 65 (1999).
2. http://www.frontedgetechnology.com/index.htm
3. D. Linden and T. B. Reddy, *Handbook of batteries*, McGraw-Hill, New York (2002).
4. B. Scrosati, *Nature Nanotechnology*, **2**, 598 (2007).
5. J. M. Tarascon and M. Armand, *Nature*, **414**, 359 (2001).
6. http://www.candlepowerforums.com/vb/showthread.php?t=64660
7. O. Crowther and A. C. West, *Journal of the Electrochemical Society*, **155**, A806 (2008).
8. Y. M. Choi and S. I. Pyun, *Solid State Ionics*, **99**, 173 (1997).
9. J. M. Rosolen and F. Decker, *Journal of the Electrochemical Society*, **143**, 2417 (1996).
10. R. A. Powers, *Proceedings of the Ieee*, **83**, 687 (1995).
11. A. K. Shukla and T. P. Kumar, *Current Science*, **94**, 314 (2008).
12. E. I. Eweka, C. O. Giwa, G. O. Mepsted, K. Green and D. Scattergood, *Journal of Power Sources*, **162**, 841 (2006).
13. G. Nagasubramanian, *International Journal of Electrochemical Science*, **2**, 913 (2007).
14. C. X. Wang, Y. Y. Xia, T. Fujieda, T. Sakai and T. Muranaga, *Journal of Power Sources*, **103**, 223 (2002).

15. K. Edstrom, T. Gustafsson and J. O. Thomas, *Electrochimica Acta*, **50**, 397 (2004).

16. P. Verma, P. Maire and P. Novak, *Electrochimica Acta*, **55**, 6332 (2010).

17. T. Zheng, A. S. Gozdz and G. G. Amatucci, *Journal of the Electrochemical Society*, **146**, 4014 (1999).

18. W. S. Kim, K. I. Chung, J. H. Cho, D. W. Park, C. Y. Kim and Y. K. Choi, *Journal of Industrial and Engineering Chemistry*, **9**, 699 (2003).

19. M. Rosso, C. Brissot, A. Teyssot, M. Dolle, L. Sannier, J. M. Tarascon, R. Bouchetc and S. Lascaud, *Electrochimica Acta*, **51**, 5334 (2006).

20. B. Scrosati and J. Garche, *Journal of Power Sources*, **195**, 2419 (2010).

21. J. T. Dudley, D. P. Wilkinson, G. Thomas, R. Levae, S. Woo, H. Blom, C. Horvath, M. W. Juzkow, B. Denis, P. Juric, P. Aghakian and J. R. Dahn, *Journal of Power Sources*, **35**, 59 (1991).

22. R. Oesten, U. Heider and M. Schmidt, *Solid State Ionics*, **148**, 391 (2002).

23. Y. E. Hyung, D. R. Vissers and K. Amine, *Journal of Power Sources*, **119**, 383 (2003).

24. Y. S. Chung, S. H. Yoo and C. K. Kim, *Industrial & Engineering Chemistry Research*, **48**, 4346 (2009).

25. G. Venugopal, J. Moore, J. Howard and S. Pendalwar, *Journal of Power Sources*, **77**, 34 (1999).

26. M. Satoh, N. Ohyama, M. Shirakata, R. Shimizu, H. Yageta and Y. Bannai, *Nec Research & Development*, **41**, 18 (2000).

27. A. K. Padhi, K. S. Nanjundaswamy and J. B. Goodenough, *Journal of the Electrochemical Society*, **144**, 1188 (1997).

28. B. Jin, E. M. Jin, K. H. Park and H. B. Gu, *Electrochemistry Communications*, **10**, 1537 (2008).

29. D. Jugovic and D. Uskokovic, *Journal of Power Sources*, **190**, 538 (2009).

30. C. M. Julien, A. Manger, A. Ait-Salah, M. Massot, F. Gendron and K. Zaghib, *Ionics*, **13**, 395 (2007).

31. C. H. Mi, X. G. Zhang and H. L. Li, *Journal of Electroanalytical Chemistry*, **602**, 245 (2007).

32. A. K. Padhi, K. S. Nanjundaswamy, C. Masquelier, S. Okada and J. B. Goodenough, *Journal of the Electrochemical Society*, **144**, 1609 (1997).

33. A. Yamada, S. C. Chung and K. Hinokuma, *Journal of the Electrochemical Society*, **148**, A224 (2001).

34. Basic Research Needs for Electrical Energy Storage, Department of Energy, *http://www.sc.doe.gov/bes/reports/files/EES_rpt.pdf* (2007).

35. G. N. Zhang, Y. G. Wang and J. S. Ma, *Materials Science and Engineering a-Structural Materials Properties Microstructure and Processing*, **337**, 274 (2002).

36. A. Patil, V. Patil, D. W. Shin, J. W. Choi, D. S. Paik and S. J. Yoon, *Materials Research Bulletin*, **43**, 1913 (2008).

37. M. Duclot and J. L. Souquet, *Journal of Power Sources*, **97-8**, 610 (2001).

38. W. Y. Liu, Z. W. Fu and Z. Qin, *Journal of the Electrochemical Society*, **155**, A8 (2008).

39. K. Marquardt, R. Hahn, T. Luger and H. Reichl, *ESTC 2006: 1st Electronics Systemintegration Technology Conference, Vols 1 and 2, Proceedings*, 1410 (2006).

40. J. B. Bates, N. J. Dudney, D. C. Lubben, G. R. Gruzalski, B. S. Kwak, X. Yu and R. A. Zuhr, *Journal of Power Sources*, **54**, 58 (1995).

41. J. B. Bates, N. J. Dudney, B. Neudecker, A. Ueda and C. D. Evans, p. 33, Halkidiki, Greece (1999).

42. Y. I. Jang, B. J. Neudecker and N. J. Dudney, *Electrochemical and Solid State Letters*, **4**, A74 (2001).

43. B. J. Neudecker, N. J. Dudney and J. B. Bates, *Journal of the Electrochemical Society*, **147**, 517 (2000).

44. X. H. Yu, J. B. Bates, G. E. Jellison and F. X. Hart, *Journal of the Electrochemical Society*, **144**, 524 (1997).

45. K. Kanehori, K. Matsumoto, K. Miyauchi and T. Kudo, *Solid State Ionics*, **9-10**, 1445 (1983).

46. K. Kanehori, Y. Ito, F. Kirino, K. Miyauchi and T. Kudo, *Solid State Ionics*, **18-9**, 818 (1986).

47. F. Kirino, Y. Ito, K. Miyauchi and T. Kudo, *Nippon Kagaku Kaishi*, 445 (1986).

48. G. Meunier, R. Dormoy and A. Levasseur, *Materials Science and Engineering B-Solid State Materials for Advanced Technology*, **3**, 19 (1989).

49. R. Creus, J. Sarradin, R. Astier, A. Pradel and M. Ribes, *Materials Science and Engineering B-Solid State Materials for Advanced Technology*, **3**, 109 (1989).

50. M. Baba, N. Kumagai, H. Kobayashi, O. Nakano and K. Nishidate, *Electrochemical and Solid State Letters*, **2**, 320 (1999).

51. M. Baba, N. Kumagai, N. Fujita, K. Ohta, K. Nishidate, S. Komaba, H. Groult, D. Devilliers and B. Kaplan, *Journal of Power Sources*, **97-8**, 798 (2001).

52. S. D. Jones and J. R. Akridge, *Solid State Ionics*, **53-6**, 628 (1992).

53. S. S. Zhang, *Journal of Power Sources*, **161**, 1385 (2006).

54. H. Ohtsuka and J. Yamaki, *Japanese Journal of Applied Physics Part 1-Regular Papers Short Notes & Review Papers*, **28**, 2264 (1989).

55. H. Ohtsuka, S. Okada and J. Yamaki, *Solid State Ionics*, **40-1**, 964 (1990).

56. N. J. Dudney, J. B. Bates, R. A. Zuhr, S. Young, J. D. Robertson, H. P. Jun and S. A. Hackney, *Journal of the Electrochemical Society*, **146**, 2455 (1999).

57. B. Wang, J. B. Bates, F. X. Hart, B. C. Sales, R. A. Zuhr and J. D. Robertson, *Journal of the Electrochemical Society*, **143**, 3203 (1996).

58. B. J. Neudecker, R. A. Zuhr, B. S. Kwak, J. B. Bates and J. D. Robertson, *Journal of the Electrochemical Society*, **145**, 4148 (1998).

59. B. J. Neudecker, R. A. Zuhr, J. D. Robertson and J. B. Bates, *Journal of the Electrochemical Society*, **145**, 4160 (1998).

60. J. B. Bates, D. Lubben, N. J. Dudney and F. X. Hart, *Journal of the Electrochemical Society*, **142**, L149 (1995).

61. J. B. Bates, N. J. Dudney, D. C. Lubben, G. R. Gruzalski, B. S. Kwak, X. H. Yu and R. A. Zuhr, *Journal of Power Sources*, **54**, 58 (1995).

62. B. J. Neudecker, R. A. Zuhr and J. B. Bates, *Journal of Power Sources*, **82**, 27 (1999).

63. Y. S. Park, S. H. Lee, B. I. Lee and S. K. Joo, *Electrochemical and Solid State Letters*, **2**, 58 (1999).

64. K. Marquardt, R. Hahn, T. Luger and H. Reichl, *MEMS 2006: 19th IEEE International Conference on Micro Electro Mechanical Systems, Technical Digest*, 954 (2006).

65. J. Cesarano III, Stuecker, J.N., Smay, J.E., Robocasting 2001: Layered Manufacturing by Slurry Extrusion, SAND2001-1820P, Sandia National Laboratories (2001).

66. J. A. Lewis, J. E. Smay, J. Stuecker and J. Cesarano III, *Journal of the American Ceramic Society*, **89**, 3599 (2006).

67. A. Safari, Cesarano III, J., Clem, P.G., Fabrication of Advanced Fundamental Electroceramic Components by Solid Freeform Fabrication Methods, SAND2002-1956P, Sandia National Laboratories (2002).

68. J. N. Stuecker, J. Cesarano III and D. A. Hirschfeld, *Journal of Materials Processing Technology*, **142**, 318 (2003).

69. J. Cesarano III, Segalman, R., Calver, P., Robocasting: Moldless Fabrication from Slurry Deposition, SAND098-0364J, Sandia National Laboratories (1998).

70. J. Cesarano III, King, B.H., Denham, H.B., Recent Developments in Robocasting of Ceramics and Multimaterial Deposition, SAND098-2195C, Sandia National Laboratories (1998).

71. J. Cesarano III, Robocasting of Ceramics and Composites Using Fine Particle Suspensions, SAND099-2778C, Sandia National Laboratories (1999).

72. J. E. Miller, L. R. Evans, J. N. Stuecker, M. D. Allendorf, N. P. Siegel and R. B. Diver, *Proceedings of the ASME International Solar Energy Conference*, 311 (2007).

73. J. Russias, E. Saiz, S. Deville, K. Gryn, G. Liu, R. K. Nalla and A. P. Tomsia, *Journal of Biomedical Materials Research Part A*, **83A**, 434 (2007).

74. E. Saiz, L. Gremillard, G. Menendez, P. Miranda, K. Gryn and A. P. Tomsia, *Materials Science & Engineering C-Biomimetic and Supramolecular Systems*, **27**, 546 (2007).

75. J. N. Stuecker, J. E. Miller, R. E. Ferrizz, J. E. Mudd and J. Cesarano, *Industrial & Engineering Chemistry Research*, **43**, 51 (2004).

76. G. Amatucci and J. M. Tarascon, *Journal of the Electrochemical Society*, **149**, K31 (2002).

77. N. Chong, J. Lim, J. Sakamoto, B. Dunn, M. Kruger, S. Eitapence, M. Freed, K. Poolla and C. J. Spanos, *Power Sources for the New Millennium, Proceedings*, **2000**, 266 (2001).

78. W. J. Cui, H. J. Liu, C. X. Wang and Y. Y. Xia, *Electrochemistry Communications*, **10**, 1587 (2008).

79. C. Delacourt, P. Poizot, M. Morcrette, J. M. Tarascon and C. Masquelier, *Chemistry of Materials*, **16**, 93 (2004).

80. K. Hawthorne, Apblett, C., Branson, E., Cook, A., Fenton, K., Clem, P., Three Dimensional Writing of MnO_2 Battery Cathodes, in *IMAPS ATW on Printed Devices and Applications*, Orlando, FL (2009).

81. K. Hawthorne, Fenton, K., Branson, E., Cook, A., Apblett, C., Towards a Printed Reserve Cell Zinc-Air Battery, in *IMAPS ATW on Printed Devices and Applications*, Orlando, Fl. (2010).

82. J. B. Bates, N. J. Dudney, B. Neudecker, A. Ueda and C. D. Evans, *Solid State Ionics*, **135**, 33 (2000).

83. R. J. Brodd, W. W. Huang and J. R. Akridge, *Macromolecular Symposia*, **159**, 229 (2000).

84. N. J. Dudney, *Materials Science and Engineering B-Solid State Materials for Advanced Technology*, **116**, 245 (2005).

85. C. Ho, I. D. Raistrick and R. A. Huggins, *Journal of the Electrochemical Society*, **127**, 343 (1980).

86. B. Y. Huang, C. C. Cook, S. Mui, P. P. Soo, D. H. Staelin, A. M. Mayes and D. R. Sadoway, *Journal of Power Sources*, **97-8**, 674 (2001).

87. M. Martin and F. Faverjon, *Thin Solid Films*, **398**, 572 (2001).

88. R. W. Larson and D. E. Day, *Journal of Non-Crystalline Solids*, **88**, 97 (1986).

89. J. B. Bates, N. J. Dudney, G. R. Gruzalski, R. A. Zuhr, A. Choudhury, C. F. Luck and J. D. Robertson, *Journal of Power Sources*, **43**, 103 (1993).

90. S. D. Jones, J. R. Akridge and F. K. Shokoohi, *Solid State Ionics*, **69**, 357 (1994).

91. F. Croce, G. B. Appetecchi, L. Persi and B. Scrosati, *Nature*, **394**, 456 (1998).

92. G. Sandi, K. A. Carrado, H. Joachin, W. Lu and J. Prakash, *Journal of Power Sources*, **119**, 492 (2003).

93. C. S. Wang, X. W. Zhang and A. J. Appleby, *Journal of the Electrochemical Society*, **152**, A205 (2005).

94. E. Zygadlo-Monikowska, Z. Florjanczyk, E. Rogalska-Jonska, A. Werbanowska, A. Tomaszewska, N. Langwald, D. Golodnitsky, E. Peled, R. Kovarsky, S. H. Chung and S. G. Greenbaum, *Journal of Power Sources*, **173**, 734 (2007).

95. A. N. Jansen, K. Amine, A. E. Newman, D. R. Vissers and G. L. Henriksen, *Jom-Journal of the Minerals Metals & Materials Society*, **54**, 29 (2002).

96. R. Hahn, K. Marquardt, M. Blechert, M. Lehmann, M. Topper, M. Wilke, P. Semionyk and H. Reichl, *Dtip 2009: Symposium on Design, Test, Integration and Packaging of Mems/Moems*, 292 (2009).

97. G. A. Ghiurcan, C. C. Liu, A. Webber and F. H. Feddrix, *Journal of the Electrochemical Society*, **150**, A922 (2003).

98. M. Ollinger, H. Kim, T. Sutto and A. Pique, *Applied Surface Science*, **252**, 8212 (2006).

99. R. Wartena, A. E. Curtright, C. B. Arnold, A. Pique and K. E. Swider-Lyons, *Journal of Power Sources*, **126**, 193 (2004).

100. L. B. Hu, J. W. Choi, Y. Yang, S. Jeong, F. La Mantia, L. F. Cui and Y. Cui, *Proceedings of the National Academy of Sciences of the United States of America*, **106**, 21490 (2009).

101. K. Gao, X. G. Hu, C. S. Dai and T. F. Yi, *Materials Science and Engineering B-Solid State Materials for Advanced Technology*, **131**, 100 (2006).

102. A. I. Gopalan, P. Santhosh, K. M. Manesh, J. H. Nho, S. H. Kim, C. G. Hwang and K. P. Lee, *Journal of Membrane Science*, **325**, 683 (2008).

103. J. Wang, *Analytical Electrochemistry*, John Wiley & Sons, Inc., Hoboken, New Jersey (2006).

104. J. Albery, *Electrode Kinetics*, Clarendon Press, Oxford (1975).

105. M. C. Zhao, S. Kariuki, H. D. Dewald, F. R. Lemke, R. J. Staniewicz, E. J. Plichta and R. A. Marsh, *Journal of the Electrochemical Society*, **147**, 2874 (2000).

106. P. E. de Jongh and P. H. L. Notten, *Solid State Ionics*, **148**, 259 (2002).

107. K. Sawai and T. Ohzuku, *Journal of the Electrochemical Society*, **150**, A674 (2003).

108. A. J. Bard and L. R. Faulkner, *Electrochemical Methods - Fundamentals and Applications*, John Wiley & Sons, Inc., New York (2001).

109. K. Dokko, M. Mohamedi, Y. Fujita, T. Itoh, M. Nishizawa, M. Umeda and I. Uchida, *Journal of the Electrochemical Society*, **148**, A422 (2001).

110. Sluyters.M and J. H. Sluyters, *Journal of Electroanalytical Chemistry*, **26**, 237 (1970).

111. J. H. Sluyters, *Recueil Des Travaux Chimiques Des Pays-Bas-Journal of the Royal Netherlands Chemical Society*, **79**, 1092 (1960).

112. C. Gabrielli, *Physical Electrochemistry*, I. Rubinstein Editor, Marcel Dekker, New York (1995).

113. D. D. Macdonald, in *Techniques for Characterization of Electrodes and Electrochemical Processes*, R. Varma, Selman, J.R. Editor, Wiley, New York (1991).

114. F. Mansfeld, Lorenz, W.J., in *Techniques for Characterization of Electrodes and Electrochemical Processes*, R. Varma, Selman, J.R. Editor, Wiley, New York (1991).

115. http://www.arkema-inc.com/kynar/literature/pdf/666.pdf

116. P. N. Garay, *Pump application desk book.*, The Fairmont Press, Inc. (1996).

117. J. F. Berret, R. Gamez-Corrales, S. Lerouge and J. P. Decruppe, *European Physical Journal E*, **2**, 343 (2000).

118. A. Du Pasquier, P. C. Warren, D. Culver, A. S. Gozdz, G. G. Amatucci and J. M. Tarascon, *Solid State Ionics*, **135**, 249 (2000).

119. M. W. Verbrugge, B. J. Koch and E. W. Schneider, *Journal of Applied Electrochemistry*, **30**, 269 (2000).

120. S. J. Zhang, A. Tsuboi, H. Nakata and T. Ishikawa, *Journal of Power Sources*, **97-8**, 584 (2001).

121. M. C. Borghini, M. Mastragostino and A. Zanelli, *Journal of Power Sources*, **68**, 52 (1997).

122. D. W. Dees, V. S. Battaglia, L. Redey, G. L. Henriksen, R. Atanasoski and A. Belanger, *Journal of Power Sources*, **89**, 249 (2000).

123. K. L. Heitner, *Journal of Power Sources*, **89**, 128 (2000).

124. G. Nagasubramanian and D. Doughty, *Journal of Power Sources*, **96**, 29 (2001).

125. S. S. Zhang, *Journal of Power Sources*, **162**, 1379 (2006).

126. R. Koksbang, I. I. Olsen and D. Shackle, *Solid State Ionics*, **69**, 320 (1994).

127. C. Fernandez-Sanchez, C. J. McNeil and K. Rawson, *Trac-Trends in Analytical Chemistry*, **24**, 37 (2005).

128. Y. P. Ma, M. Doyle, T. F. Fuller, M. M. Doeff, L. C. Dejonghe and J. Newman, *Journal of the Electrochemical Society*, **142**, 1859 (1995).

129. S. Obeidi, N. A. Stolwijk and S. J. Pas, *Macromolecules*, **38**, 10750 (2005).

130. A. A. Blumberg, S. S. Pollack and C. A. J. Hoeve, *Journal of Polymer Science Part a-General Papers*, **2**, 2499 (1964).

131. K. Fenton, Apblett, C., Atanassov, P., Towards a Fully Printable Battery: Robocast Deposition of $LiFePO_4$ Structures, in *216th Electrochemical Society Meeting*, Vienna, Austria (2009).

132. P. Kuisma-Kursula, *X-Ray Spectrometry*, **29**, 111 (2000).

133. M. Popall, R. Buestrich, G. Semrau, G. Eichinger, M. Andrei, W. O. Parker, S. Skaarup and K. West, *Electrochimica Acta*, **46**, 1499 (2001).

134. J. K. Whear, *Journal of Power Sources*, **177**, 226 (2008).

135. S. A. H. Ali and A. K. Arof, *Journal of Alloys and Compounds*, **449**, 292 (2008).

136. S. Megahed and B. Scrosati, *Journal of Power Sources*, **51**, 79 (1994).

137. http://www.celgard.com/products/specialty-membranes.asp

138. P. Arora and Z. M. Zhang, *Chemical Reviews*, **104**, 4419 (2004).

139. S. S. Zhang, *Journal of Power Sources*, **164**, 351 (2007).

140. J. Y. Song, Y. Y. Wang and C. C. Wan, *Journal of Power Sources*, **77**, 183 (1999).

141. A. M. Elmer and P. Jannasch, *Polymer*, **46**, 7896 (2005).

142. R. Frech, S. York, H. Allcock and C. Kellam, *Macromolecules*, **37**, 8699 (2004).

143. F. M. Delnick, Process of manufacturing porous separator for electrchemical power supply, U.S. patent number 5,882,721 (1997).

144. F. M. Delnick, Doi, S., Denzumi, S., Process of manufacturing porous separator for electrochemical power supply, U.S. patent number 6,148,503 (1999).

145. L. W. Hrubesh, *Chemistry & Industry*, 824 (1990).

146. D. A. Doshi, P. B. Shah, S. Singh, E. D. Branson, A. P. Malanoski, E. B. Watkins, J. Majewski, F. van Swol and C. J. Brinker, *Langmuir*, **21**, 7805 (2005).

147. S. S. Prakash, C. J. Brinker, A. J. Hurd and S. M. Rao, *Nature*, **374**, 439 (1995).

148. K. Fenton, Apblett, C., Atanassov, P., Towards a Fully Printable Battery: Robocast Deposition of Printable Separators, in *217th Electrochemical Society Meeting*, Vancouver, BC, Canada (2010).

149. S. W. Kim, S. Iwamoto and M. Inoue, *Journal of Porous Materials*, **17**, 377 (2010).

150. W. C. Li, A. H. Lu, W. Schmidt and F. Schuth, *Chemistry-a European Journal*, **11**, 1658 (2005).

151. G. M. Pajonk, *Applied Catalysis*, **72**, 217 (1991).

152. Q. Q. Ke, X. Y. Huang, P. Wei, G. L. Wang and P. K. Jiang, *Journal of Applied Polymer Science*, **104**, 1920 (2007).

153. B. K. Ryu, S. C. Rew, H. C. Park and I. Yasui, *Journal of Materials Science Letters*, **15**, 889 (1996).

154. T. Kawamura, S. Okada and J. Yamaki, *Journal of Power Sources*, **156**, 547 (2006).